Master's thesis

NTNU
Norwegian University of Science and Technology
Faculty of Natural Sciences
Department of Physics

Viktor Mikalsen

Modelling the Galactic NII intensities and the distribution of OB associations

Master's thesis in Physics
Supervisor: Michael Kachelriess
June 2024

NTNU
Norwegian University of
Science and Technology

Viktor Mikalsen

Modelling the Galactic NII intensities and the distribution of OB associations

Master's thesis in Physics
Supervisor: Michael Kachelriess
June 2024

Norwegian University of Science and Technology
Faculty of Natural Sciences
Department of Physics

NTNU
Norwegian University of
Science and Technology

Abstract

The distribution of Galactic supernovae is of great interest as these powerful explosions are the primary source of cosmic rays. These highly energetic particles have been observed for over a century. Recently, more effort has been dedicated to studying the most energetic cosmic rays and their subsequent diffuse emission of photons in the peta-electronvolt energy range. Their sources, called "PeVatrons", are generated by supernovae but are yet to be observationally determined.

As such, the main objective of this thesis is to generate a model for the Galaxy capable of predicting past supernova occurrences, which can be further developed to model the propagation of cosmic rays. We consider two models for the Galaxy: an axisymmetric model and a spiral arm model. These models are compared to the N II intensities observed by the FIRAS instrument, with the spiral arm model most accurately reproducing the data. With the spiral arm model, we use a Monte Carlo simulation to model the locations of OB associations, which are the birthplaces of the stars massive enough to undergo core collapse at the end of their lifetimes. Combining the known OB associations and those we model, we present a comprehensive model for the Galactic distribution of OB associations and past supernova events.

Sammendrag

Hvordan supernovaer er fordelt i Melkeveien er av stor interesse ettersom disse kraftige eksplosjonene er hovedkilden til kosmisk stråling. Disse svært energiske partiklene har blitt observert i over et århundre. I løpet av de senere årene har mer innsats blitt dedikert til å studere de aller mest energirike partiklene og deres diffuse stråling av fotoner med energi opp mot noen peta-elektronvolt. Kildene til denne diffuse strålingen kalles for ”PeVatrons” og er generert av supernovaer, men ingen PeVatrons har enda blitt direkte observert.

Dermed er hovedformålet med denne oppgaven å lage en modell for Melkeveien som kan predikere fordelingen av tidligere supernovaer. Denne modellen kan utvikles videre for å simulere hvordan kosmisk stråling propagerer gjennom Melkeveien. Vi studerer to modeller for galaksen vår: en aksesymmetrisk modell, og en spiral arm modell. Disse modellene blir evaluert opp mot den observerte intensiteten av N II, som har blitt observert av FIRAS instrumentet. Av disse modellene er det spiral arm modellen som klarer å gjenskape disse dataene best. Med spiral arm modellen bruker vi en Monte Carlo simulering til å modellere lokasjonene til OB assosiasjoner, som da er fødestedet til de stjernene som er massive nok til å ende sitt liv i en supernovaeksplosjon. Ved å kombinere data fra de kjente OB assosiasjonene og de vi modellerer, kan vi presentere en omfattende modell for fordelingen av OB assosiasjoner i Melkeveien og tidligere supernovaer.

Acknowledgements

I want to express my gratitude to my supervisor, Professor Michael Kachelriess, for giving me the opportunity to work on this project. His extensive guidance and feedback throughout this year have been invaluable and much appreciated. Thank you for the weekly meetings, which helped me understand the topics better and motivated me with the work. Also, thank you for helping me on short notice when I was stuck through mail and extra meetings.

I also wish to thank Joy Haina Sørbotten and Kasper Voogt Arvesen for proofreading my thesis, whose time and feedback have been much appreciated. I would also like to thank Joy for supporting me through this year and listening to both my problems with the thesis and enthusiastic ramblings when the solutions were found.

Contents

Chapter 1

Introduction

More than a hundred years have now passed since Hess (1912)[1] discovered that the highly energetic radiation, which we now know as cosmic rays (CR), was of extraterrestrial origin. This discovery granted him the Nobel Prize in physics in 1936, and in the years since, extensive research on cosmic rays has been carried out. Recent progress in understanding astrophysical feedback mechanisms significantly indicates that CRs are potentially vital for our understanding of the formation and evolution of galaxies on a cosmological scale and regulating star formation processes (see, e.g., Ruszkowski & Pfrommer 2023, and references therein). From where in the Milky Way CRs originate and how they propagate through it is thus important for our knowledge and understanding of the Galaxy.

It is generally assumed that CRs gain their energy by being accelerated by supernovae remnant (SNR) shock waves (Axford 1981; Blandford & Eichler 1987). The majority of all supernovae, roughly 80% – 90%, occur as core-collapse supernovae (Type II and Ib/c, see, e.g. van den Bergh & McClure 1994), with the remainder being thermonuclear explosions by accreting white dwarfs (Type Ia, see, e.g., Hillebrandt & Niemeyer 2000). A minimum amount of mass is needed for a star to undergo core collapse by the end of its lifetime, and this value is often taken as $8\mathrm{M}_\odot$ (Smartt 2009; Woosley & Weaver 1995). The more massive the stars are, the more quickly they will burn their fuel, and stars with a mass of $8\mathrm{M}_\odot$ have a lifetime of about 38 Myr (Fuchs et al. 2006; Schaller et al. 1992). This is a short timeframe from the astrophysical point of view, and for comparison, our own Sun is roughly 4570 Myr old and has more than half of its original fuel left (Bonanno et al. 2002).

Stars whose mass lies in the range $2.7\,\mathrm{M}_\odot - 18.7\,\mathrm{M}_\odot$ are classified as B stars, and those stars with an even greater mass are classified as O stars (Mamajek 2022; Pecaut & Mamajek 2013). This system for classifying stars was first introduced by Morgan, Keenan et al. (1943), and collectively, we refer to all stars with a mass greater than $2.7\,\mathrm{M}_\odot$ as OB stars. Observationally, stars are classified by observing their apparent magnitude in different wavebands to calculate their colour index (Johnson & Morgan 1953). Thus, we would expect that the spatial origins of cosmic rays coincide with the distribution of these massive ($> 8\mathrm{M}_\odot$) OB stars, which end their lives as supernovae.

---

[1] For an English translation from 2018 by Angelis and Schultz, see Hess (2018).

OB stars are not distributed uniformly throughout the Galaxy but are rather most commonly found in structures called OB associations, something we have known for more than a century (examples of some important early works include Eddington 1914; Kapteyn 1914). The term "association" was first coined by Ambartsumian (1947), who also pointed out that these structures are of very low density ($< 0.1\,\mathrm{M}_\odot\,\mathrm{pc}^{-3}$). Previously, Bok (1934) had shown that stellar groups with such a low density were unstable against Galactic tidal forces, leading Ambartsumian (1949) to suggest that these OB associations were very young. Being so relatively sparse (as compared to other structures, for instance, open clusters), OB associations have been defined as being gravitationally unbound structures of stars (see, e.g., Wright 2020), and more recently, as "groups of young stars with a stellar density lower than that of the Galactic field and that are not strongly associated with interstellar matter" (Wright, Goodwin et al. 2022).

OB associations are often found in star forming regions and have ages typically from a few to a few tens of Myr (see, e.g. Chapter 2 and Wright 2020). This makes OB associations very interesting for studying, for instance, star forming processes, the early evolution of stars, and the distribution of young stars. As more studies have been carried out, and particularly with observations with Gaia, it has become increasingly clear that OB associations are very complex structures with high degrees of spatial, kinematic and temporal clustering and that most OB associations and their substructures are expanding, suggesting they were more compact in the past (see, e.g., Wright, Goodwin et al. 2022).

OB associations are also interesting objects to study with respect to the interstellar medium (ISM). When massive stars die as supernovae, they inject large amounts of energy into the ISM, significantly affecting the pressure and velocity dispersion of the surrounding gas (McKee & Ostriker 1977). Supernovae play a crucial role in the creation of new nuclei, a process called nucleosynthesis, which affects the metallicity of the ISM.

Where can we expect to find these OB associations? Their locations are revealed not only through direct observation but also through their effect on their surroundings. Massive stars inject large amounts of energy into the surrounding gas through ionising photons and stellar winds, which in turn create hot, low-density, ionised cavities within the ISM (see, e.g., Mac Low & McCray 1988). These ionised regions are often referred to as H II regions, owing to them mainly consisting of hydrogen gas (Franco et al. 1990). The relationship between massive, ionising stars and H II regions have been known for over a century; Hubble (1922a,b) showed that H II regions are strongly associated with massive O stars.

Supernovae can further enlarge these cavities, and when enough supernovae have occurred, these cavities can become several hundred parsecs in radii, structures often referred to as superbubbles (Mac Low & McCray 1988; Tenorio-Tagle & Bodenheimer 1988; Tomisaka 1992). Superbubbles are also surrounded by hot, ionised H II regions, which are responsible for absorbing the majority of the ionising radiation emitted by embedded, massive stars which have not yet exploded (McKee & Williams 1997). On the outskirts of these structures, we find dense, thin, neutral and cold shells of gas which have been swept up and blown away by the expanding supernova shock waves (Mac Low & McCray 1988). Moreover, the correlation between H II regions and OB associations has been well established through direct observation (see, e.g., de Zeeuw et al. 1999; Wright 2020, and Chapter 2).

In this thesis, we will be using far-infrared ionised nitrogen at 205 µm (N II) to infer the spatial distribution of the H II regions and, thus, the spatial distribution of OB associations. The rationale for using N II as a tracer for H II regions is that the ionisation potentials of H I and N I are, respectively, 13.6 eV and 14.5 eV, meaning that nitrogen and hydrogen can be ionised by approximately the same radiation since their ionisation potentials are so similar. It is expected that N II is completely ionised within H II regions (Goldsmith et al. 2015; Wright, Cheng et al. 1991), and thus, that H II regions are significant sources of the observed N II intensity (McKee & Williams 1997; Roshi & Anantharamaiah 2001). Moreover, it is worth noting that other works have also used the N II intensity as a tracer for H II regions, like Higdon & Lingenfelter (2013), McKee & Williams (1997) and Steiman-Cameron et al. (2010).

We will be using the N II 205 µm intensities as measured by the far-infrared absolute spectrophotometer (FIRAS) on the Cosmic Background Explorer (COBE), operated from November 18, 1989 to September 21, 1990. Its mission was to conduct an unbiased far-infrared survey of the spectral line emission of our Galaxy to measure the cosmic microwave background (CMB) spectrum and to observe the line and dust emission of the Galaxy. FIRAS performed the first all-sky spectral line survey in the far-infrared region. The data from FIRAS facilitated the calculation of the CMB temperature, and the full-sky coverage and careful calibration allowed for the detection of several spectral lines. This included the very first observation of the 205.3 µm N II line (Wright, Cheng et al. 1991). This line was so strong that Fixsen et al. (1999) could produce a full sky map of N II, shown in their Figure 1.

The primary goal of this thesis is to develop an improved model for OB associations in the Galaxy that integrates known and newly modelled associations to predict historical supernova occurrences. In Chapter 2, we investigate the literature for data on the most prominent OB associations, which are either close enough to Earth or luminous enough so that they have been well studied. In Chapter 3, we investigate two different models for the Galactic distribution of N II. In Chapter 4, we use the resulting model for the Galaxy from Chapter 3 to simulate the distribution of OB associations. Finally, we combine the known and modelled associations to build a comprehensive model for the distribution of OB associations in our Galaxy.

Chapter 2

Observational Data on Known OB Associations

This chapter will investigate the observational data found in the literature on the known OB associations. Together with our modelled associations, this data will be used in Chapter 4.2 to generate a comprehensive model of the distribution of OB associations. For each association investigated, we are primarily interested in the age, distance, position in the sky, and a metric on the stellar content, such as the number of OB stars or stars in a specific mass range.

Most of the data and information in this section is gathered from the paper "OB associations and their origins" by Wright (2020) and the references therein, and from papers released since. For most associations, positions are taken from Wright's Table 1. In general, the closest associations are those which are best studied, and for some, there are estimates in the literature on past supernovae based on observational data. A table with the gathered data for the different associations will be given at the end of this chapter.

For the number of stars in each association, either star catalogues of known massive stars in OB associations are used or specific, more up-to-date studies for the specific association if available. The highly cited paper of Humphreys (1978) is one such catalogue, which was updated in 1984 (Humphreys & McElroy 1984) and yet again in 1989 (Blaha & Humphreys 1989). These catalogues mainly focused on the massive O stars and early B types, compared to, e.g., de Zeeuw et al. (1999), who investigated the entire stellar population. Blaha & Humphreys (1989) consider their catalogue to be fairly complete for stars brighter than $M_{\text{bol}} \sim -7.5$ up to 3 kpc from Earth. Unfortunately, this catalogue and the one from 1984 do not seem to be freely available online, and, e.g., Wright (2020) used the catalogue from 1978 instead. The fairly recent studies of Melnik & Dambis (2017, 2020) use Gaia DR1 and Gaia DR2, respectively, in their work and rely on the catalogue of Blaha & Humphreys (1989) for identifying the OB associations and stars. In Melnik & Dambis (2020), they identified more than 90% of the stars in Blaha & Humphreys with DR2 data. Hence, this catalogue will be preferred, but as the different catalogues contain different associations, all will be used in this chapter, except those from 1984 and 1989.

2.1 Scorpius-Centaurus

The Scorpius-Centaurus association, also known as Sco-Cen or Scorpius OB2, is our closest association, being only 100 pc – 150 pc away from the Sun (de Zeeuw et al. 1999). With a size of about 100 pc, it extends for almost 90° over the sky, covering several constellations. Historically, Blaauw (1964) divided the association into three subgroups by, namely Upper Scorpius (US), Upper Centaurus-Lupus (UCL) and Lower Centaurus-Crux (LCC). More recent studies have revisited these subdivisions and favoured a more continuous distribution (Pecaut & Mamajek 2016; Rizzuto et al. 2011; Wright & Mamajek 2018).

The coordinates and ages for each subgroup are taken from Table 1 of Wright (2020). Wright & Mamajek (2018) list the number of stars per subgroup, totalling 433. Their work was built upon the Bayesian membership analysis of Rizzuto et al. (2011), who identified 436 stars across Sco-Cen. Rizzuto's criterion for selection was stars with a B–V colour index ≤ 0.6, corresponding to a stellar mass greater than 1.06 $M_\odot$ (Mamajek 2022; Pecaut & Mamajek 2013). Furthermore, Wright & Mamajek (2018) estimate the total stellar mass to be about 4000 $M_\odot$, and that the association contains at least 150 B type stars of spectral types B9 and earlier as well as a runaway O9V star associated with it (de Zeeuw et al. 1999; Wright 2020).

For Scorpius-Centaurus, several studies have estimated the number of past supernovae events. The first of such studies was done by de Geus (1992), who listed his estimate for each subgroup in his Table 3. Subsequent work by Preibisch & Mamajek (2008) estimated about 7 past supernovae in UCL, which agreed with de Geus's estimate of 6 ± 3 supernovae. Wright writes that most studies have estimated the total stellar content of LCC to be just above half of that of UCL (de Geus 1992; Mamajek et al. 2002), and thus an estimate of four past supernovae in LCC is appropriate. This, too, fits with de Gaus's estimate of 3 ± 2 past supernovae in LCC. For UC, a recent paper from 2023 by Briceño-Morales & Chanamé (2023) estimated four past supernovae. In total, an estimated 15 supernovae have occurred across Scorpius-Centaurus in the past.

2.2 Orion

The Orion OB Association, commonly known as Orion OB1, spans 200 deg^2 in the sky and is one of the best-studied associations in our Galaxy due to its relative closeness of about 300 pc – 450 pc (Brown et al. 1994; Zari et al. 2018). This association is commonly divided into four subgroups labelled a–d due to Blaauw (1964). Despite being well studied, Wright (2020, p. 16) writes that "There are very few estimates of the total stellar mass of the Orion OB1 association in the literature" and estimates the total mass of the association to be somewhere between 4000 $M_\odot$ – 13500 $M_\odot$. Blaauw (1964) reports that the Orion associations contains at least 53 stars of spectral type B3 and earlier, but reports none in Ori OB1d.

The positions, distances and ages for the four subgroups are taken from Table 1

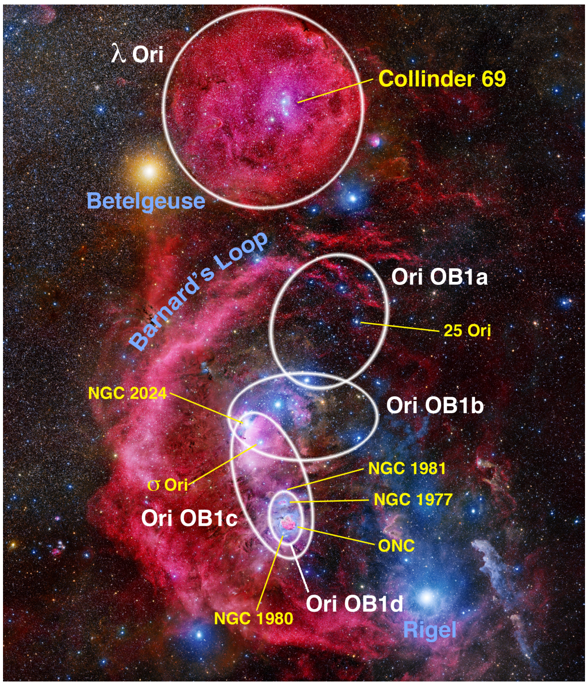

Figure 2.1: Figure 9 in Wright (2020). Illustrating the Orion constellation and its subgroups. Background astrophotograph courtesy of Stanislav Volskiy.

of Wright (2020). Regarding the stellar content, the studies of Humphreys (1978) and Melnik & Dambis (2017, 2020) are of little help, as these give the stellar content for Orion OB1 as a whole, and not per subgroup. Instead, we use the numbers reported by Briceno (2008) who used the works of Brown et al. (1994) and Hillenbrand (1997) to estimate the number of stars per subgroup with a mass greater than $2\,\mathrm{M}_\odot$. We note that the age estimations for these subgroups vary and Wright (2020) reported, for instance, that the age of Ori OB1a could be anywhere from eight to twelve Myr old. Moreover, Briceno (2008) also gave an overview of several earlier age estimations for each group which varied a lot. As such, picking an estimate for the ages of these subgroups is somewhat arbitrary.

2.3 Vela OB2

The Vela association was first reported by Kapteyn (1914) and is located at a distance of about 400 pc away from Earth (Cantat-Gaudin et al. 2019; de Zeeuw et al. 1999). Due to its projection against the Galactic plane, Vela OB2 has historically not received as much attention as other associations, but this has changed in recent years. de Zeeuw et al. (1999) made the first kinematical study of the association, and Cantat-Gaudin et al. (2019) identified seven substructures in the association, two of which belong to the Trumpler region. They also find significant age spread, with ages for Vela OB2 ranging from about 10 Myr – 40 Myr. A more recent paper by Armstrong, Wright, Jeffries, Jackson & Cantat-Gaudin (2022) also find that Vela OB2 is substructured, and estimates of the ages of pre-main-sequence stars (PMS) in each subgroup are given in their Figure 8. However, these ages must be scaled by about 25% – 30% to match previous results, and the underestimation is discussed in the paper. Moreover, the older (about 35 Myr) open cluster NGC 2547, previously considered as a part of Vela, is reported to be an interloper. As such, the age of Vela will here be estimated to 13 Myr, corresponding to a 25% – 30% increase of the estimated age of Vela OB2 of 10.3 Myr by Armstrong, Wright, Jeffries, Jackson & Cantat-Gaudin (2022).

de Zeeuw et al. (1999) identifies 93 high mass members of the association based on Hipparcos data. This result has recently been revised by Armstrong, Wright & Jeffries (2018), which by using Gaia DR2 data decreased this number to 82 massive stars, 72 of which have a mass of at least 2.5 $M_\odot$.

2.4 Trumpler 10

Bordering Vela OB2 lies Trumpler 10. This region was considered an open cluster until de Zeeuw et al. (1999) reclassified it as an association. de Zeeuw reports 22 B type stars in Trumpler 10, the earliest being spectral type B3V. Trumpler 10 is older than Vela OB2, being approximately 45 Myr – 50 Myr old (Cantat-Gaudin et al. 2019).

2.5 The Cygnus region

The Cygnus region is a massive star forming complex in our Galaxy, located 1 kpc – 2 kpc from Earth (Uyanıker et al. 2001). Despite its distance, it has received a considerable amount of attention due to its richness in recent star formation, including the Cygnus X star forming region, hundreds of OB stars, and many H II regions and supernova remnants (e.g., Comerón & Pasquali 2012; Fesen et al. 2021; Quintana & Wright 2022; Wright 2020). Humphreys (1978) divided Cygnus into the nine classical OB associations, out of which Cygnus OB2 is by far the most massive, richest and best-studied association. Cygnus OB2 contains 169 primary OB stars, out of which 52 are of type O (Wright, Drew et al. 2015), making it one of the largest groups of O stars in our Galaxy (Wright 2020). Cyg OB2 is also home to one of our Galaxy's most massive and luminous red hypergiants, namely NML Cyg (Zhang et al. 2012). Regarding past supernovae, there have been at least two supernovae in the Cygnus X region, one in the centre of Cyg OB2 and one or two in the Cygnus Loop (Reipurth & Schneider 2008).

Recent work has revealed that many of the classical associations of Humphreys do not form coherent kinematic groups. Quintana & Wright (2021) used Gaia EDR3 to investigate the parts of the Cygnus region covering the best-studied classical associations: Cyg OB1, OB2, OB3, OB8 and OB9. They found six new associations, of which only two resembled the classical ones: Cyg OB2 and OB3. For this thesis, the data found in their Table 1 for the position, age and number of OB stars will be used, and the associations will be named Cyg A – F as they do. Due to their data-filtering process, their sample of member stars is slightly incomplete, which they correct for using a Monte Carlo simulation. They report 681 OB stars in these groups, where 87 are of type O.

For the remainder of the Cygnus Associations, Cyg OB4, OB5, OB6 and OB7, reliable data is challenging to come by. de Zeeuw et al. (1999) investigated OB4 and OB7 and could not find evidence based on Hipparcos data that they were even real groups. They write on page 36 that ”Some of the previous claims for OB associations based on large numbers of supergiants and/or early-type stars in this direction, e.g., Cyg OB4 and Cyg OB7, may therefore be the result of chance projections”. However, Melnik & Dambis (2017) list Cyg OB4 and OB7 in their table of OB associations, but only reports an estimate for the steller content for OB7. Of these, only Cyg OB7 made it to their newer catalogue from 2020 (Melnik & Dambis 2020), where it is listed as having seven stars with mass greater than $20\,\mathrm{M}_\odot$ and a total stellar mass of $2.9 \times 10^3\,\mathrm{M}_\odot$. OB5 and OB6 are not listed in their papers. Wright (2020) lists in his Table 1 the positions and approximate distances of CYG OB4, OB5 and OB6, but no age estimates for these associations are available. He writes that OB4 has an age of 8.3 Myr, but this age is taken from Uyanıker et al. (2001) who gave this age estimate for OB3. Uyanıker et al. list no age estimate for OB4, OB5 or OB6. No estimates on stellar content or mass for OB4, OB5, or OB6 have been found in the literature.

Based on this discussion, CYG OB4, OB5, and OB6 will be left out of the model. The region covering Cyg OB1, OB2, OB3, OB8 and OB9 will be simulated by the recent census of Quintana & Wright (2021). For CYG OB7, position and distance are taken from Table 1 of Wright (2020) and the stellar content from Melnik & Dambis (2020). Regarding its age, it is known that Cyg OB7 is home to active star formation and could contain stars as young as 0.1 Myr old (Wolk et al. 2013), while OB7 could be as old as 13 Myr (Uyanıker et al. 2001).

2.6 Auriga

Quintana, Wright & Jeffries (2023) recently revisited the Auriga constellation. Classically, this region has been identified with two OB associations, Aur OB1 and Aur OB2, first reported by Roberts (1972) and Humphreys (1978). Their distances from Earth are respectively 1.06 kpc and 2.42 kpc (Melnik & Dambis 2017). In their study, Quintana, Wright & Jeffries (2023) employ Gaia data to discover that these classical groupings are too extended in proper motions and distance to be considered actual associations. Instead, they identify five associations in this region, which they number 1 – 5. Three of these replace the old associations, whereas the remaining two are completely new. Of these five associations, association 1 is by far the richest association with a total stellar mass of about $6000\,\mathrm{M}_\odot$ at about 1 kpc away. Coordinates, ages, total stellar mass and number of OB stars are collected from Table 4 from Quintana, Wright & Jeffries (2023). As with the Cygnus data, they have to correct for observational incompleteness, and this is taken into account for the listed masses. For their second association, they give no number for the age but an upper limit of hundreds of millions of years, and its total stellar mass is about 1/6 of the mass of association 1. Association 5 is by far the most distant association at 2.76 kpc and contains even less mass than association 2. Therefore, only the data for associations 1, 3, and 4 will be used here.

2.7 Ara OB1

Ara OB1 was first reported by Whiteoak (1963) and is a compact association covering approximately one square degree (Arnal et al. 1987) located in the Carina Sagittarius Arm. Some sources list Ara OB1 as consisting of two associations, Ara OB1A and OB1B (e.g., Humphreys 1978; Melnik & Dambis 2017), whereas others such as Wright (2020) list Ara OB1 as only one association. From the available findings, there are no age estimations for Ara OB1B, and given its distance of approximately 2.8 kpc, we will solely focus on Ara OB1A, which will be referred to as Ara OB1.

Ara OB1 hosts active star formation and contains the RCW 108 cloud, which is in its early stages of evolution (Comerón, Schneider et al. 2005). The distance to the association has been estimated to 1.32 kpc (Herbst & Havlen 1977), but in the more recent work of Melnik & Dambis (2020) it is given a distance of 1.1 kpc. Humphreys (1978) lists that Ara OB1 contains at least seven O stars and seven B stars, and Melnik & Dambis (2020) list Ara OB1 as having eleven stars with a mass greater than $20\,\mathrm{M}_\odot$ and a total stellar mass of $4.3 \times 10^{10}\,\mathrm{M}_\odot$. Regarding the age, Whiteoak estimated it to be 5 Myr, whereas Arnal estimated a somewhat younger age of 2 Myr. Given that Arnal's work was done 24 years after Whiteoak's, 2 Myr will be used for the association's age. Position is taken from Melnik & Dambis (2020).

2.8 Perseus OB2

First reported by Blaauw (1944), Perseus OB2 (Per OB2) is an association within the Perseus molecular cloud. Per OB2 is one of the closest associations to Earth at only 318 pc, and has thus become one of the more well-studied associations (de Zeeuw et al. 1999). The age of Per OB2 has previously been estimated to be as high as 15 Myr (e.g., Bally et al. 2008; Gimenez & Clausen 1994), but in a more recent study which focused on Young Stellar Objects (YSO) towards the Per OB2 and the Perseus star forming complex, the highest reported age was about 10 Myr (Azimlu et al. 2015). Using Hipparcos data, de Zeeuw et al. (1999) identify 41 massive members towards the association, with the majority being of type B and A. Out of the 17 classical B type members of the association, only eight of them are confirmed as members by de Zeeuw et al. (1999). However, the total stellar content could be as high as 20000 stars (Bally et al. 2008). There is also a runaway, massive O star associated with Per OB2, ξ Per, which may have been expelled from the association due to a past supernova explosion (Bally et al. 2008; de Zeeuw et al. 1999).

2.9 Carina OB1

The Carina OB1 (Car OB1) is a fairly distant association, located at a distance of approximately 2.35 kpc (Shull et al. 2021), an estimate based on Gaia EDR3 which is in good agreement with the previously established distance of 2.3 kpc (Smith 2006). Car OB1 is an association rich in OB stars, star clusters and H II regions. It mainly comprises the large Carina Nebula and its constituents, but also some surrounding clusters (Wright 2020). Car OB1 has been subject to numerous studies, including kinematic studies by Melnik & Dambis (2017, 2020). Star formation has been ongoing for the last 10 Myr in Car OB1, whereas the first high-mass stars were formed around 5 Myr – 6 Myr ago (DeGioia-Eastwood et al. 2001). Regarding the stellar content, the census of Berlanas et al. (2023) will be used, which is likely the best and most complete census of OB stars for Car OB1. In their work, they use, among others, the Gaia-ESO survey to compile a catalogue of OB stars across Car OB1 and obtain 74 O type stars, 214 non-supergiant B type stars, and six WR stars or non-O-supergiants for a total of 294 massive stars.

2.10 Canis Major OB1

Ambartsumian (1949) was the first to propose Canis Major OB1 (CMa OB1) as an association, located in the constellation of Canis Major at a distance of about 1.2 kpc (Zucker et al. 2019, 2020). It has long been suspected that CMa OB1 has been home to at least one supernova event (see, e.g., de Zeeuw et al. (1999) and references therein), and in a recent study by Fernandes et al. (2019), they find it likely that there have occurred at least three supernovae in the past in CMa OB1, at about 6, 2 and 1 Myr ago.

In recent years, efforts have been made to map the young stellar population of CMa OB1 (e.g., Fischer et al. 2016; Gregorio-Hetem et al. 2021). Santos-Silva, Gregorio-Hetem et al. (2018) used X-ray data to investigate the YSOs in CMa OB1 and reported that there have been several episodes of star formation in the association, with the first happening around 10 Myr ago and the second 5 Myr ago, and that the association is now in the final stages of star formation. Shevchenko et al. (1999) also report a few stars older than 10 Myr, but the vast majority are younger. Given this and the suggested past supernovae, an age of 10 Myr will be used.

Finding modern censuses on the content of OB stars has been difficult. Most recent papers are concerned with YSOs, and where they mention the massive stars, they quote the results of Gregorio-Hetem (2008), stating that CMa OB1 contains at least 200 B type stars and a few O type stars (e.g., Fernandes et al. 2019; Santos-Silva, Perottoni et al. 2021; Wright 2020). The Gregorio-Hetems catalogue of massive stars in CMa OB1 is primarily based on the works of Claria (Claria 1974; Clariá 1974, papers I and II) and Shevchenko et al. (1999). Out of Clarias 247 massive stars observed in the direction of CMa OB1, 44 were considered probable members of the association. Shevchenko identified 88 stars out of a sample of 165 as probable members. Upon examination of the Gregorio-Hetems table, it was determined that the compilation includes two O stars and 91 B stars, in addition to stars of various other spectral types and some without specified spectral classifications.

2.11 Monoceros

Recently, the associations Monoceros (Mon) OB1 and R1 have been the subject of a kinematical study by Lim et al. (2022). Using Gaia EDR3 and radial velocity data found in the literature, they identified 728 members of these associations and the surrounding halo, where 24 are of type O and B. From their analysis, they determine a distance to OB1 and R1 to be, respectively, approximately 700 pc and 660 pc. They also find that the stars' spatial distribution and kinematic properties show that each association contains three substructures, which agrees with earlier studies on OB1 (e.g., Sung et al. 2008). Monoceros OB1 is also home to the star forming region NGC 2264 (Kuhn et al. 2014), and from Lim's work, they find that OB1 and R1 are home to stars up to 5 Myr old. Note that older work from Sagar et al. (1986) found that the majority of stars within NGC 2264 were between 1 Myr and 10 Myr old. For simplicity, this analysis will assume the presence of only one cluster, selecting it based on the distance measurements for OB1, as it is the most massive. The coordinates from Wright (2020) will be used.

Projected close to Mon OB1 lies Mon OB2 at a further distance of about 1.5 kpc, which is home to both the Rosetta Nebula and its central cluster NGC 2244 (Wright 2020). Although Melnik & Dambis (2020) report a slightly shorter distance of 1.2 kpc, this measurement revises earlier estimates from Blaha & Humphreys (1989). This revision is elaborated in Melnik & Dambis (2017, 2020) and references therein. Despite this, the distance listed in Mahy et al. (2009) will be used as it builds upon more recent work than that of Blaha & Humphreys. Others, including Knies et al. (2024), have also opted for a distance of 1.5 kpc, who derived the same distance from the calculations by Leahy et al. (1986) on the distance to the SNR Monoceros Loop (SNR G205.5+0.5).

Mon OB2 contains at least ten O type stars (e.g., Humphreys 1978; Martins et al. 2012), and in Table 3 of Melnik & Dambis (2020) they list Mon OB2 as having 13 known members with a mass greater than 20 $M_\odot$. The position is taken from Melnik & Dambis (2020), and the simulation will adopt an age of 5 Myr, based on the works of Chen, de Grijs et al. (2007), who identified stellar ages up to 4 Myr, and Martins et al. (2012), who reported that all observed O stars were younger than 5 Myr.

2.12 Scorpius OB1

Scorpius OB1 (Sco OB1) is a massive association in the Sagittarius spiral arm. It is home to, among others, the young cluster NGC 6231, the open cluster Trumpler 24, and some of the brightest stars in our Galaxy (Humphreys 1978; Wright 2020). With around 4000 M-type stars and a total mass of 8500 $M_\odot$, Sco OB1 is among the most massive associations in our Galaxy (Damiani 2018).

In the catalogue of Humphreys (1978), 18 O stars and ten B stars are listed as members of Sco OB1, and in the review by Reipurth (2008), they write that Sco OB1 is home to more than 100 massive stars, among them 15 O stars. In a more recent paper, Melnik & Dambis (2020) list Sco OB1 as having 28 stars with mass more than $20\,M_\odot$.

Recently, portions of Sco OB1 have been subject to a study by Yalyalieva et al. (2020) using Gaia DR2 data. They focused on the northern and central parts of the association, regions rich in pre-main-sequence (PMS) stars. They identified nine subgroups, of which three were discarded as association members. The remaining six have an average distance from Earth of 1560 pc, in excellent agreement of the distance of 1580 pc reported by Damiani (2018). The association is home to recent star forming activities, and the six-member groups have an average age of 5.6 Myr. This age estimate aligns with previous research findings, but there are also indications of stars in Sco OB1 being as old as 10 Myr (see, e.g. Damiani 2018; Reipurth 2008, and references therein).

2.13 Lacerta OB1

Lacerta OB1 (Lac OB1) is among the closest associations to Earth at a distance of about 358 kpc (de Zeeuw et al. 1999). Despite being relatively close, Lacerta has not received much attention because it is relatively sparse and was, for instance, not included in the survey of the solar neighbourhood of Bouy & Alves (2015). The most up-to-date data comes from de Zeeuw et al. (1999) based on Hipparcos, and other more recent studies also use his results (e.g. Balega et al. 2017; Chen & Lee 2008). Humphreys (1978) only lists a single O star as a member of Lac OB1, whereas de Zeeuw et al. (1999) find 36 OB stars towards Lacerta OB1 from the Hipparcos data. Of these, 14 O–B5 stars are confirmed as members of Lacerta OB1.

de Zeeuw also discusses the classical division of Lac OB1 into OB1a and OB1b, a division made by Blaauw (1958), but disputes that OB1a is a real association. As such, OB1a will not be considered here. The age of Lac OB1 is not well determined, and Wright (2020) writes that it could be anywhere from a few Myr to 25 Myr based on Chen & Lee (2008). de Zeeuw cites Blaauw (1964, 1991) and writes the age of OB1b could be between 12 Myr and 16 Myr. Wright and Chenn & Lee also point out that the O stars main sequence lifetime is about 3.6 Myr (Schaerer & de Koter 1997). Thus, setting the age for the model is somewhat arbitrary, and an age of 10 Myr will thus be used.

2.14 Scutum OB2

Scutum OB2 (Sct OB2) was first referenced by Ambartsumian (1949) and has recently received relatively little attention in the literature. The most recent study focusing on the Sct OB2 is that of Reichen et al. (1990). Here, they list Sct OB2 as having a total of 17 OB stars and also suggest that Sct OB2 consist of two different groups, one located at a distance of 510 pc and the other at 1170 pc with 14 of the OB stars located in the latter grouping. The earlier work by Humphreys (1978) listed eleven OB stars with an average distance of about 1 kpc. Thus, the distance of Reichen et al. and their division of Sct OB2 into two groups will be used, and the closest one will be discarded. Values for the position will be taken from Melnik & Dambis (2017). The most recent age estimate which was found in the literature is 6 Myr (Schild & Maeder 1985), a value referenced by recent work of both Wright (2020) and Tetzlaff et al. (2010).

2.15 Serpens associations

Serpens OB2 (Ser OB2) is also an often neglected association, and the latest paper dedicated to this association is that of Forbes (2000). He significantly increased the number of known OB stars, from the 15 stars reported by Humphreys (1978) to 107. He also found that these stars have an average distance of 1.9 kpc from Earth and a common age of 5 Myr. He reports the location at Galactic coordinates $l = 18.5°$, $b = 2.0°$, which agrees with the position listed by Melnik & Dambis (2017) that will be used here.

There is little information regarding Ser OB1 in the literature. Humphreys (1978) lists the association as having nine O and B stars. Melnik & Dambis (2020) list Ser OB1 as having 20 stars with a mass greater than $20\,\mathrm{M}_\odot$. There are, however, many papers in the literature concerning Ser OB1s central cluster NGC 6611 (e.g., Hillenbrand et al. 1993). A recent paper by Stoop et al. (2023) used Gaia EDR3 to investigate this cluster and reported a distance of 1706 pc. They also find that the cluster has formed at least 19 O stars (including runaway stars). The cluster contains two populations of stars, one being approximately 1.3 Myr old and the other at 7.5 Myr. They also write that most OB stars belong to the younger group and that several previous studies have estimated the cluster's age to be between 1 Myr and 3 Myr. Considering the spread in estimated ages, a value of 5 Myr will be used here. Position is taken from Melnik & Dambis (2020).

2.16 Summary of the known associations

Here, the data which has been discussed and collected are summarised in Table 2.1. The data found in this table will be used for the model. Figure 19 found in Wright (2020) showing the distribution of those associations he summarised in his paper is shown in Figure 2.2.

Table 2.1: Observational data on known associations. The data listed are as discussed in the text, with the masses found in Mamajek (2022) and Pecaut & Mamajek (2013). The sixth column describes how many stars will be used for the Monte Carlo simulations, and the seventh column describes the minimum mass these stars must have.

Name	l (deg)	b (deg)	d (pc)	Age(Myr)	N_s	Min mass ($M_\odot$)
Sco-Cen: US	351.50	20.00	143	10	107	1.06
Sco-Cen: UCL	331.00	12.50	136	16	179	1.06
Sco-Cen: LCC	298.50	5.50	115	15	147	1.06
Ori OB1a	201.0	-17.3	360	12	234	2.0
Ori OB1b	205.0	-18.0	400	6	123	2.0
Ori OB1c	211.3	-19.5	385	4	246	2.0
Ori OB1d	209.0	-19.5	380	1	62	2.0
Vela OB2	262.80	-7.70	400	13	72	2.5
Trumpler 10	262.80	0.70	372	45	22	2.68
Cyg A	72.61	2.06	1895	14	125	2.68
Cyg B	78.58	3.31	1726	9	93	2.68
Cyg C	76.11	0.54	1713	8	88	2.68
Cyg D	75.44	1.19	2000	20	86	2.68
Cyg E	80.19	0.85	1674	8	133	2.68
Cyg F	74.04	1.44	1985	11	156	2.68
Cyg OB7	89.00	0.00	630	13	7	20
Aur 1	170.72	-0.16	1056	21	206	2.68
Aur 3	170.70	0.11	1514	12	111	2.68
Aur 4	173.09	-0.03	1923	2	128	2.68
Ara OB1	337.68	-0.92	1100	2	11	20
Per OB2	159.20	-17.10	318	10	9	2.68
Car OB1	286.50	-0.50	2350	6	294	2.68
CMa OB1	224.00	-1.30	1200	10	93	2.68
Mon OB1	202.10	1.00	700	5	24	2.68
Mon OB2	207.35	-1.60	1500	5	13	20
Sco OB1	343.30	1.20	1580	6	28	20
Lac OB1	96.70	-17.60	358	10	14	4.7
Sct OB2	23.18	-0.54	1170	6	14	2.68
Ser OB2	18.21	1.63	1900	5	107	2.68
Ser OB1	16.72	0.07	1706	5	20	20

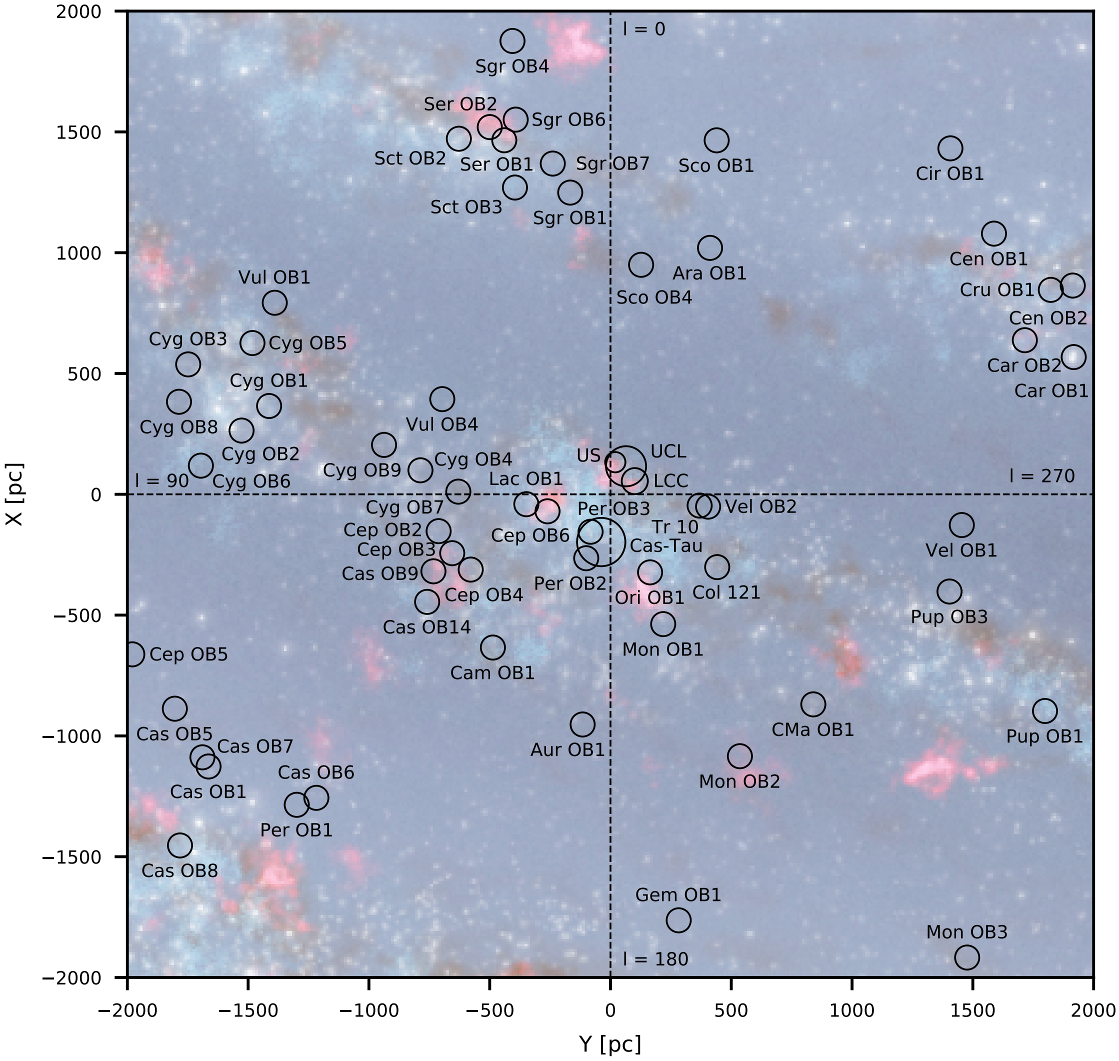

Figure 2.2: Figure 19 in Wright (2020). It illustrates the distribution of the closest OB associations in the Galactic X-Y plane, with the Sun at the centre. Wright updated and expanded the figures of Blaauw (1991) and de Zeeuw et al. (1999) based on Ruprecht (1966) list of OB associations. The distances in Wright (2020) are primarily from Gaia DR2 studies. The background is an artist's illustration of the Milky Way Galaxy, which notably precedes Gaia DR2 (Credit: NASA/JPL-Caltech/R. Hurt).

Chapter 3

Modelling the Galactic Distribution of N II Intensities

Following the approach of Higdon & Lingenfelter (2013), two different models for the Galactic N II emissivity are considered. Firstly, an axisymmetric three-dimensional model is investigated, whose integrated intensity spectra poorly reproduce the measured FIRAS 205 µm intensity. Hence, a more complicated model is studied, taking into account the spiral arm structure of the Galaxy. One finds that this model can more accurately reproduce the measured FIRAS 205 µm intensity.

3.1 Axisymmetric model

The simplest approach to modelling Galactic N II emissivity is to adopt an axisymmetric distribution. Following McKee & Williams (1997), an exponential distribution will be employed. Entering the equation is the distribution's scale length, $H_\rho^{\mathrm{N\,II}}$, which must be determined. The equation

$$S(\rho) \propto \mathrm{e}^{-\rho/H_\rho^{\mathrm{N\,II}}} \tag{3.1}$$

is used by McKee & Williams (1997) not to model the Galactic N II emissivity but rather to make a simple model for the surface density of OB associations. They utilised data from Galactic radio H II regions, compiled by Smith et al. (1978), and further studies on H II regions in optical, far-infrared, and thermal radio emissions. McKee & Williams fitted the H II regions in Smith et al. (1978) to this exponential distribution and found the scale length for the fit to be $H_\rho^{\mathrm{lyc}} = 3.34^{+0.71}_{-1.25}$ kpc. Throughout the rest of their paper, they decided to adopt the rounded value of $H_\rho^{\mathrm{lyc}} = 3.5$ kpc for their simplified model, taking into account previous work by others. However, considering the observed large-scale gradient in the nitrogen-to-hydrogen abundance ratio across the Galaxy, as, e.g., documented by Daflon & Cunha (2004) and Shaver et al. (1983), this same scale length cannot be used for the N II emissivity distribution. Therefore, as in Higdon & Lingenfelter (2013), a shorter scale length for the axisymmetric N II emissivity model will be used here.

Daflon & Cunha (2004) analysed 69 OB stars located at Galactocentric distances between 4.7 kpc and 13.2 kpc. They find that the metallicity gradients are, in general, quite similar for the elements considered and give an average slope for the gradients of $-0.042(7)\,\mathrm{dex\,kpc^{-1}}$ which is the value used in Higdon & Lingenfelter (2013). Note that they do list the slope for nitrogen itself in their Table 3 as $-0.046\,\mathrm{dex\,kpc^{-1}}$, but this is so close to the average that it does not change the derived scale length for the N II emissivity.

Esteban & García-Rojas (2018) recently revisited the radial abundance gradients of nitrogen and oxygen. They selected 13 H II regions located at Galactocentric distances between 5.7 kpc and 16.1 kpc. Because of them selecting H II regions with a low degree of ionisation, they report that their number for the nitrogen radial abundance gradient is the first which is independent of the ionisation correction factor. Their reported value is $-0.059(9)\,\mathrm{dex\,kpc^{-1}}$. As this value is much more recent than that of Daflon & Cunha (2004) and the uncertainties in the two values are fairly similar, the result of Esteban & García-Rojas (2018) will be used in this work.

Following Higdon & Lingenfelter (2013), the value for the scale length $H_\rho^{\mathrm{N/H}}$ is determined as follows:

$$\frac{1}{H_\rho^{\mathrm{N\,II}}} \simeq \frac{1}{H_\rho^{\mathrm{N/H}}} + \frac{1}{H_\rho^{\mathrm{lyc}}}. \tag{3.2}$$

To use this equation, a relation between $H_\rho^{\mathrm{N/H}}$ and the nitrogen radial abundance gradient of $-0.059(9)\,\mathrm{dex\,kpc^{-1}}$ must be established. A change of $0.059\,\mathrm{dex\,kpc^{-1}}$ corresponds to a change by a factor of $10^{0.059} \simeq 1.15$ per kpc, and since $H_\rho^{\mathrm{N/H}}$ is the distance by which the quantity is reduced by a factor of e we get the following:

$$1.15^{H_\rho^{\mathrm{N/H}}} = \mathrm{e} \Rightarrow \frac{1}{H_\rho^{\mathrm{N/H}}} = \ln(1.15)\mathrm{kpc}^{-1}. \tag{3.3}$$

Inserting this number into Equation (3.2) together with $H_\rho^{\mathrm{lyc}} = 3.5\,\mathrm{kpc}$ from McKee & Williams (1997), we get that $H_\rho^{\mathrm{N\,II}} = 2.4\,\mathrm{kpc}$.

McKee & Williams (1997) also noted that Smith et al. (1978) listed no H II regions within $\rho \leq \rho_{\mathrm{min}} = 0.39\,R_{\mathrm{S}}$ or beyond $\rho_{\mathrm{max}} = 1.3\,R_{\mathrm{S}}$, where R_{S} is the distance between the Galactic centre and the Sun. McKee & Williams used a value of $R_{\mathrm{S}} = 8.5\,\mathrm{kpc}$, for which ρ_{min} evaluates to 3.315 kpc and $\rho_{\mathrm{max}} = 11.05\,\mathrm{kpc}$. ρ_{min} and ρ_{max} will thus mark the boundaries for which this axisymmetric model is valid, and the rounded values $\rho_{\mathrm{min}} = 3\,\mathrm{kpc}$ and $\rho_{\mathrm{max}} = 11\,\mathrm{kpc}$ will be used in the model. Note that these rounded values are also those used by McKee & Williams (1997). Higdon & Lingenfelter (2013) used a different value for R_{S} than McKee& Williams which they did not correct for in their axisymmetric model, causing the ρ_{max} used in this thesis to be about 1 kpc larger than that of Higdon & Lingenfelter.

The axisymmetric N II emissivity distribution will be modelled using a Galactocentric Cartesian coordinate system, following Higdon & Lingenfelter (2013). The origin is at the Galactic centre, with the y-axis defined to pass through the Sun and the Galactic centre and the x-axis being orthogonal to the y-axis. The Sun is placed on the positive y-axis. A Galactocentric cylindrical coordinate system (ρ, θ, z) is parameterised as $\rho = \sqrt{x^2 + y^2}$, $\theta = \arctan(y/x)$ and z is measured orthogonal to the Galactic plane, following the usual right-hand rule.

The intensity of N II 205 µm will be calculated by a line of sight integral from its emissivity and compared with the observed FIRAS 205 µm intensity. This calculation requires Earth-centred coordinates (r, l, b), where r represents the radial distance from Earth, l the longitude and b the latitude. The longitude l measures the angular distance from the Sun-Galactic Centre line, and the latitude b is the angular distance north of the Galactic plane as observed from Earth. To convert from Earth-centred coordinates to Galactocentric coordinates, the following formulas are used:

$$\begin{aligned}
\rho &= \sqrt{r^2 \cos^2 b + R_\mathrm{S}^2 - 2R_\mathrm{S} r \cos b \cos l}, \\
\theta &= \arctan\left(\frac{R_\mathrm{S} - r\cos b \cos l}{r \cos b \sin l}\right), \\
z &= r \sin b.
\end{aligned} \tag{3.4}$$

Higdon & Lingenfelter (2013) use $R_\mathrm{S} = 7.6\,\mathrm{kpc}$, but since their work in 2013, this distance has been revised by more recent studies. The GRAVITY Collaboration et al. (2019) estimated this distance to be $8.178 \pm 0.035\,\mathrm{kpc}$, and more recently, the VERA Collaboration et al. (2020) estimated a value of $7.92 \pm 0.46\,\mathrm{kpc}$. Here, the result from the GRAVITY Collaboration will be used since it has the smallest combined statistical and systematic uncertainties, as detailed in the respective papers.

The N II 205 µm line emissivity is calculated using $S(\rho)$ in Equation (3.1) as follows,

$$\epsilon_\mathrm{D}(\rho) = LS(\rho)P_z(z)/A_\mathrm{D}. \tag{3.5}$$

Here, L is the total Galactic N II 205 µm luminosity, $P_z(z)$ represents the dependence of H II superbubbles on the distance z from the Galactic plane, and A_D is the effective Galactic disk area. $\epsilon_\mathrm{D}(\rho)$ is in units of $\mathrm{erg\,s^{-1}\,cm^{-3}}$, L in units of $\mathrm{erg\,s^{-1}}$, A_D in units of $\mathrm{cm^2}$, and finally, $P_z(z)$ in units of $\mathrm{cm^{-1}}$. $S(\rho)$ is dimensionless.

To calculate A_D, Equation (37) in McKee & Williams (1997) is used:

$$\begin{aligned}
A_\mathrm{D} &= \int_{\rho_\mathrm{min}}^{\rho_\mathrm{max}} S(\rho) 2\pi\rho \,\mathrm{d}\rho \\
&= 2\pi \left(H_\rho^\mathrm{N\,II}\right)^2 [(1 + \rho_\mathrm{min}/H_\rho)S(\rho_\mathrm{min}) - (1 + \rho_\mathrm{max}/H_\rho)S(\rho_\mathrm{max}))],
\end{aligned} \tag{3.6}$$

which with the adopted values for ρ_min, $H_\rho^\mathrm{N\,II}$ and ρ_max evaluates to $A_\mathrm{D} = 21.265\,\mathrm{kpc}$.

Finally, we must address how the function $P_z(z)$ is represented. Following Higdon & Lingenfelter (2013), a Gaussian height distribution will be used:

$$P_z(z) = \frac{e^{-0.5z^2/\sigma_z^2}}{\sqrt{2\pi}\sigma_z}. \tag{3.7}$$

The parameter σ_z determines the distribution of N II regions above and below the Galactic plane. The FIRAS data cannot be used to determine this z-dependence of the emissivity due to the beam size of the FIRAS instrument being too large to resolve the Galactic plane. Hence, other results must be used to determine the value of σ_z. Specifically, we will be using hydrogen radio recombination lines (RRL) as a tracer for the latitudinal distribution of H II regions, which is known to stem from their outer envelopes (see, e.g. Anantharamaiah 1986; Roshi & Anantharamaiah 2001).

Roshi & Anantharamaiah (2001) found that the low-frequency RRL had a full-width half maximum of about 1.8° in latitude. They also found that 75% of the identified H II regions in high-frequency RRL surveys were located in the Galactic plane, with $|b| < 1.5°$. Moreover, a more recent study by Quireza et al. (2006) presents a comprehensive study of RRLs in 106 Galactic H II regions using the National Radio Astronomy Observatory's (NRAO) 140-foot telescope. This study aims to enhance the understanding of the composition, structure, kinematics, and physical properties of photodissociation regions (PDRs) on the edges of H II regions. They measured spectra from 119 different regions, with some H II regions, such as M16 and M17, being measured several times. They tabulated results from these measurements in their Table 1, of which a histogram was made for this work and shown in Figure 3.1. Only four measurements had a Galactic latitude greater than 4°, and 88 were within $|b| < 1°$, equating to about 74 % of the sample size. It should be noted that most of the H II regions in Quireza et al. (2006) were located in the first and fourth quadrants and that many of their sources are located at several kiloparsecs away due to their criteria for the study. For instance, they write that for the $^3\mathrm{He}^+$ survey, distant sources are best, and the nearby, classical associations are excluded. This study substantiates the argument that H II regions are strongly concentrated around the Galactic disk.

Higdon & Lingenfelter (2013) found that to reproduce the full width at half maximum (FWHM) reported by Roshi & Anantharamaiah (2001), their model required a standard deviation for the height distribution of $\sigma_z = 0.15\,\mathrm{kpc}$. Even though this value is much greater than the exponential scale height of OB stars of 0.045 kpc (Reed 2000) and the scale height of molecular clouds of 0.035 kpc (Stark & Lee 2005), it is comparable to a result of McKee & Williams (1997). They reported a value for the vertical scale height σ_z for H II regions as $\sigma_z = 0.15\,\mathrm{kpc}$. As such, a value for $\sigma_z = 0.15\,\mathrm{kpc}$ will too be adopted in this thesis.

We will be using the longitude profile of the N II 205 µm intensity as reported by Fixsen et al. (1999), illustrated in their figure 5(e), to compare our model with. This longitude profile was made using data from the Far Infrared Absolute Spectrophotometer (FIRAS) instrument onboard the Cosmic Background Explorer (COBE). As the FIRAS beam essentially was a top hat 7° across, it was not able to resolve the Galactic plane. As such, Fixsen et al. (1999) had to carefully process the data to produce this longitude profile. Their approach is described in detail in their paper, but in short, to produce this line profile, they used the FIRAS data before they were binned into pixels and instead used bins centred on the Galactic plane 1° wide in latitude and 5° wide in longitude. They then fitted this data to the beam shape, assuming that the Galactic plane completely dominates the sky at low latitudes. The resulting intensity in each bin in Figure 5(e) of Fixsen et al. (1999) is the average over 5° in longitude and ± 0.5° in latitude. The resulting line profiles of Fixsen et al. (1999) are available publicly at NASA's Goddard Space Flight Center,

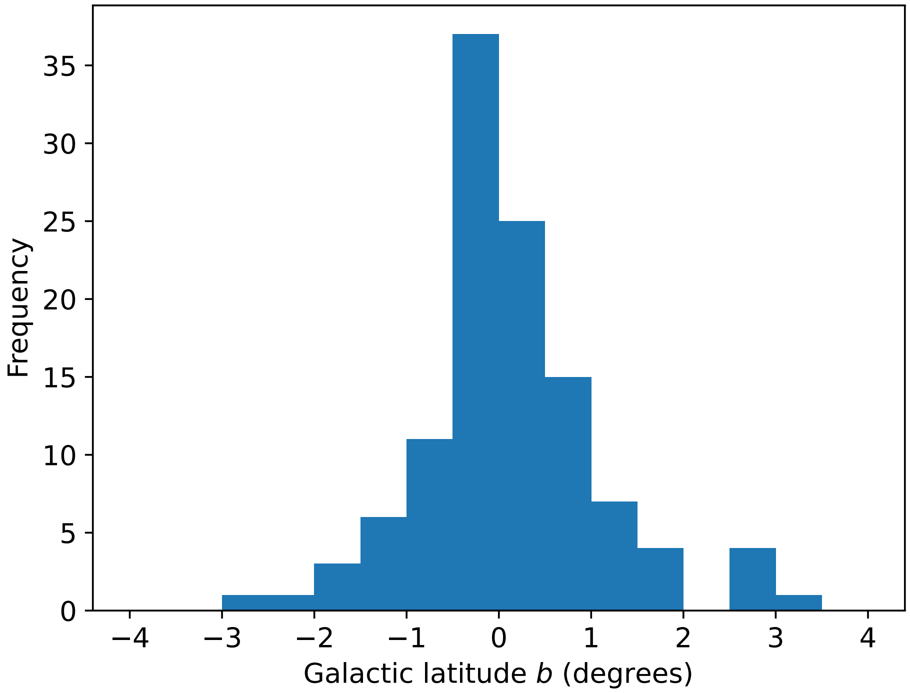

Figure 3.1: Histogram over 115 H II regions found in Table 1 of Quireza et al. (2006).

`https://lambda.gsfc.nasa.gov/product/cobe/firas_prod_table.html`.

Dale J. Fixsen was available to offer insight into the observational data and even shared the pixel data for the N II line. The data for the entire sky was binned into 6144 pixels, with each pixel covering $4\pi/6144\,\mathrm{sr}$, corresponding to the side of each pixel being approximately 2.9° wide. None of these pixels were centred on the Galactic plane. Fixsen suggested that binning the pixel data with bins 5° wide in longitude and 10° wide in latitude, centred on the Galactic plane, could produce an approximation of the data in Fig 5(e) in Fixsen et al. (1999). The 10° wide band in latitude is to take into account the wide FIRAS beam of 7° and the fact that no pixels were centred on the plane. This would create an average for a 10° band in latitude, and assuming the radiation is all from a 1° band, one would need to multiply this by 10. This is not the same as weighting by the beam shape and will thus not be used here, but his suggestion highlighted an important assumption used both in Fixsen et al. (1999) and Higdon & Lingenfelter (2013), namely that all the radiation comes from a 1° wide plane.

Now, the modelled line intensities for N II 205 µm can be calculated. From the emissivity, as given in Equation (3.5), the intensity is defined as

$$I(l,b) = \int \frac{\epsilon_D(\rho(r,l,b))}{4\pi r^2}\, r^2 \,\mathrm{d}r. \tag{3.8}$$

The intensities from Fixsen et al. (1999) is averaged over $\Delta l = 5°$ and $\Delta b = 1°$, and thus we need to average our modelled intensities in Equation (3.8) to compare it with their data. Following the suggestion from Fixsen, we integrate over $\pm 5^\circ$ in latitude and divide by $\Delta b = 1^\circ$, assuming that all radiation comes from the Galactic plane. We also average over $\Delta l = 5^\circ$, and the average intensities are then given as follows,

$$\langle I(l,b)\rangle = \frac{1}{\Delta l\,\Delta b}\int_{b=-5^\circ}^{b=+5^\circ}\int_{l=-2.5^\circ}^{l=+2.5^\circ}\int_{0}^{r_{\max}}\frac{\epsilon_D(\rho(r,l,b))}{4\pi r^2}\,r^2\cos b\,\mathrm{d}r\,\mathrm{d}l\,\mathrm{d}b. \tag{3.9}$$

The averaged line intensities have units of $\mathrm{erg\,cm^{-2}\,s^{-1}\,sr^{-1}}$, and $r_{\max} = 11\,\mathrm{kpc}$, as discussed earlier in the text. Following Higdon & Lingenfelter (2013), this axisymmetric model is then normalised to the observed FIRAS N II 205 µm intensity at longitude $l = 30^\circ$. This normalisation required a total Galactic N II luminosity of $1.92 \times 10^{40}\,\mathrm{erg\,s^{-1}}$, which is in close agreement with the value of Higdon & Lingenfelter of $1.85 \times 10^{40}\,\mathrm{erg\,s^{-1}}$. Some of this difference could be explained by the more up-to-date values used in this thesis, but the exact implementations of the models could also have had some impact.

The resulting figure for the axisymmetric model is shown in Figure 3.2 together with the observed intensities from Fixsen et al. (1999) as a histogram. The result of Higdon & Lingenfelter is also shown in Figure 3.3 for comparison. From our figure, it is clear that this model poorly reproduces the observed intensities for longitudes $l > 30^\circ$ and $l < 330^\circ$ as it falls off too slowly and fails to capture much of the details in the data. Hence, a more complicated and accurate model is needed and will be considered next.

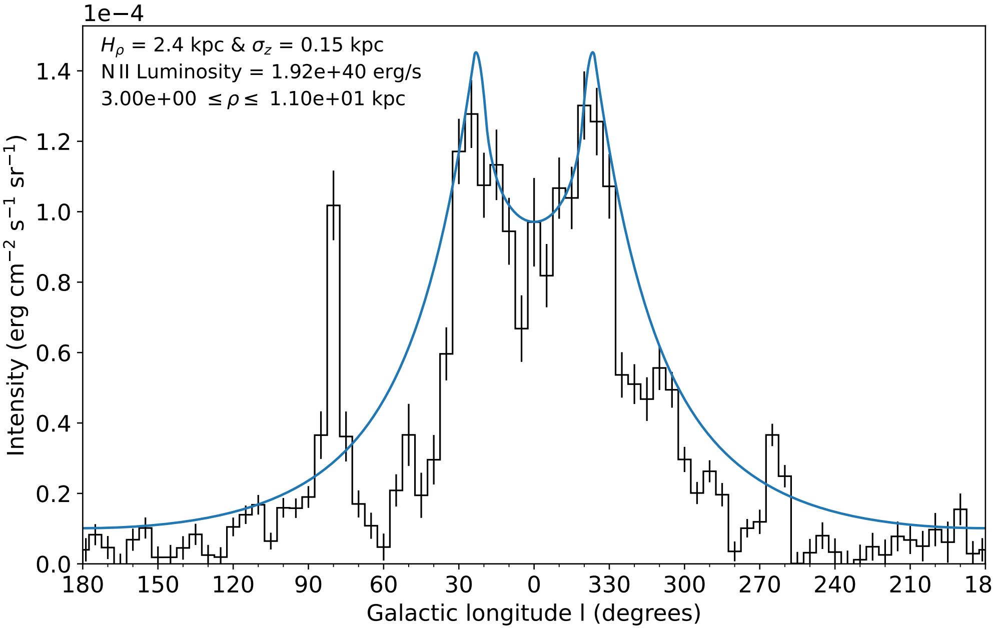

Figure 3.2: N II 205 µm line intensity plot (blue line), resulting from the axisymmetric model. The measured N II line from FIRAS in Figure 5(e) of Fixsen et al. (1999) is shown as a histogram.

3.2 Spiral arm model

Morgan, Sharpless et al. (1952) were the first to identify spiral arms in the Milky Way, and the Galaxy's structure has since been thoroughly studied. Studying H II regions and their massive ionising stars, Georgelin & Georgelin (1976) proposed that the Galaxy consists of four spiral arms known as Norma-Cygnus (NC), Perseus (P), Sagittarius-Carina (SA), and Scutum-Crux (SC). This four-arm spiral model is shown in Figure 3.4 together with the Local Arm, which will be discussed later. The most common spiral arm tracers are H II regions, but also giant molecular clouds, H I regions, infrared radiation, and masers have been used to determine spiral arm properties (see, e.g., Benjamin et al. 2005; Georgelin & Georgelin 1976; Hou, Han & Shi 2009).

There is still much uncertainty about the exact structure of the Galaxy, and significant work has been done in the past few decades to improve our understanding of it. Some of the most well-known recent works on the subject are those of Jacques P. Vallée (see, e.g., Vallée 2008, 2013) and Hou & Han (2014). The spiral arm model proposed by Higdon & Lingenfelter (2013) is built on the work of Vallée (2008), which has also served as a starting point for this work.

Both Vallée (2008) and Hou & Han (2014) use a logarithmic model for the positions of the spiral arm medians in the Galactocentric cylindrical coordinate system, which can be described by the following equations found in Higdon & Lingenfelter (2013):

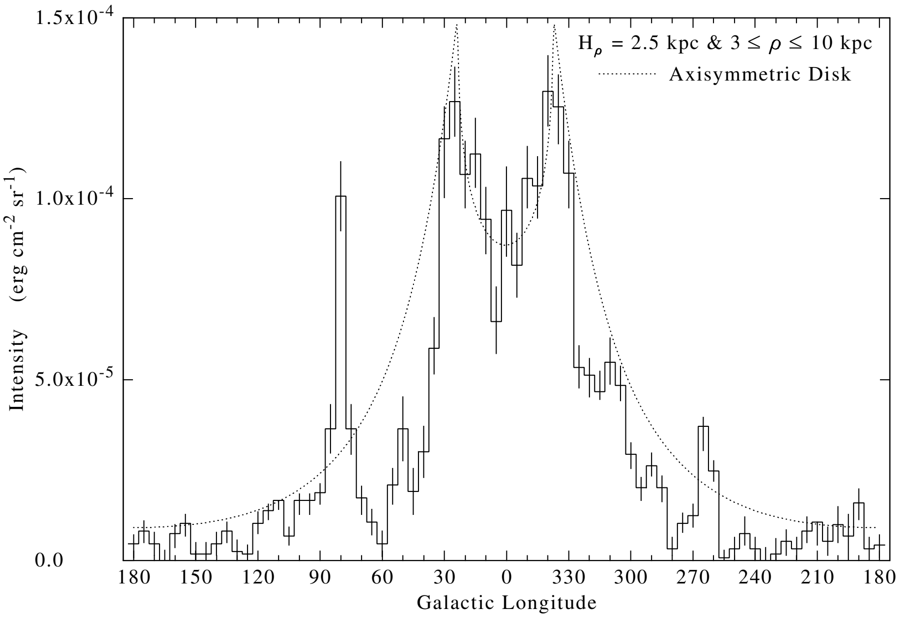

Figure 3.3: N II 205 µm line intensity plot, resulting from the axisymmetric model of Higdon & Lingenfelter (2013) as illustrated in their Figure 1. They used a value for $R_\mathrm{S} = 7.6\,\mathrm{kpc}$, and their model required a total N II luminosity of $1.85 \times 10^{40}\,\mathrm{erg\,s^{-1}}$. The measured N II line from FIRAS in Figure 5(e) of Fixsen et al. (1999) is shown as a histogram.

$$\begin{aligned} \rho(\theta) &= \rho_\mathrm{min} e^{k(\theta-\theta_0)}, \\ \rho_\mathrm{min} &\leq \rho \leq \rho_\mathrm{max}, \\ k &= \tan(p), \end{aligned} \tag{3.10}$$

where p is the pitch angle for the given spiral arm, ρ_min and ρ_max are respectively the inner and outer limits for the spiral arm, and θ_0 is the starting angle for the spiral arm as measured counterclockwise from the x-axis. Vallée does not give an explicit value for ρ_min, and as such Higdon & Lingenfelter (2013) used Figure 1 in Vallée (2008) to estimate a value for $\rho_\mathrm{min} = 2.9\,\mathrm{kpc}$. The same value for ρ_min was used by Steiman-Cameron et al. (2010), who also built a model for the Galaxy using FIRAS data. As such, we will also use $\rho_\mathrm{min} = 2.9\,\mathrm{kpc}$. Following Higdon & Lingenfelter (2013) and Vallée (2008), a value for $\rho_\mathrm{max} = 35\,\mathrm{kpc}$ will here be used for the outer limit.

Vallée (2008) assumes a Galactocentric distance $R_\mathrm{S} = 7.6\,\mathrm{kpc}$ from the Sun in his model, which is the same value employed by Higdon & Lingenfelter (2013). As previously mentioned, the more up-to-date value of $R_\mathrm{S} = 8.178\,\mathrm{kpc}$ is used in this thesis, and as such, the starting angles and pitch angles will differ here from Higdon

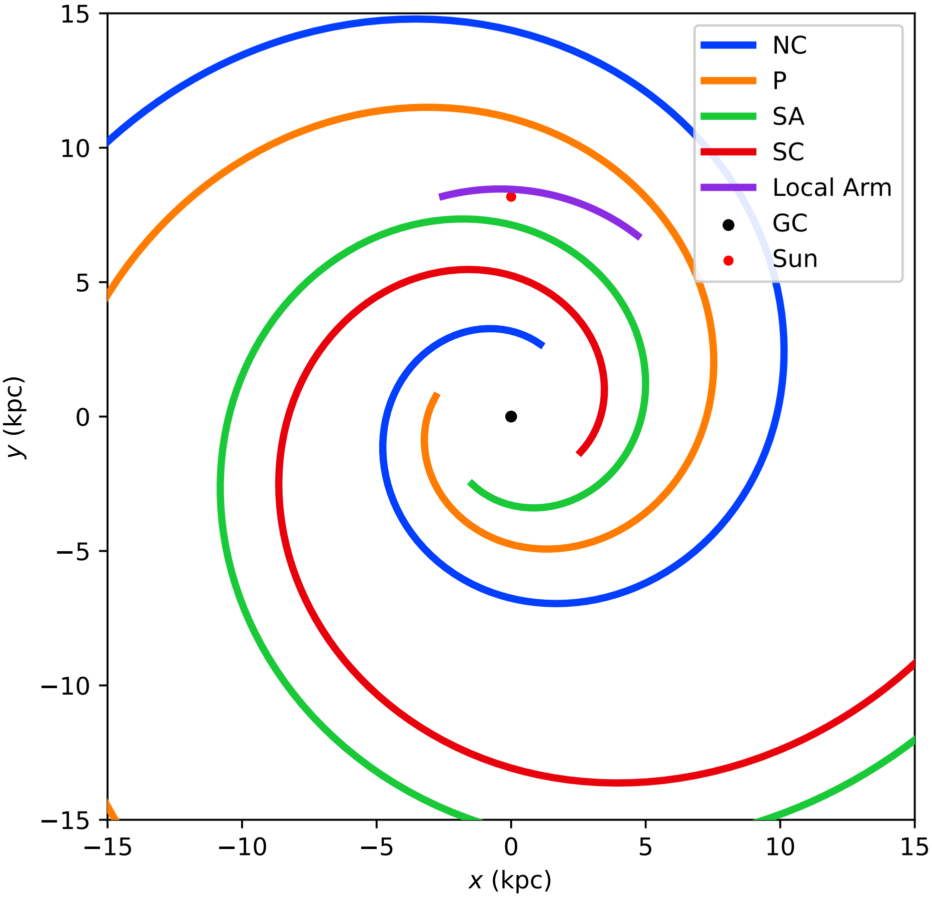

Figure 3.4: Schematic of the Milky Way, showing the four major spiral arms Norma-Cygnus (NC), Perseus (P), Sagittarius-Carina (SA), and Scutum-Crux (SC), as well as the Local Arm. The Galactic Centre (GC) and the Sun are also highlighted. The parameters for this spiral arm model are discussed later in the text.

& Lingenfelter (2013). These eight angles were first tweaked manually until the model became reasonable compared to the observational data from FIRAS. Then, a script designed to vary these angles and calculate the corresponding reduced χ^2 value was created and employed to determine the best fit for the spiral arm angles and pitch angles. These values are listed in table 3.1 in units of degrees. The fitting procedure is explained in Chapter 3.2.5.

With the spiral arm medians defined by Equation (3.10), we can begin to create the transverse components of the arms. Following Cordes & Lazio (2002) and Taylor & Cordes (1993), the width of the arms are modelled with an exponential distribution,

$$P_{\Delta}(\Delta) = e^{-0.5\,\Delta^2/\sigma_{\mathrm{A}}^2}, \tag{3.11}$$

Table 3.1

Name	$\theta_{0,\text{ NC}}$	$\theta_{0,\text{ P}}$	$\theta_{0,\text{ SA}}$	$\theta_{0,\text{ SC}}$	$p_{\text{ NC}}$	$p_{\text{ P}}$	$p_{\text{ SA}}$	p_{SC}
Higdon & Lingenfelter	70	160	250	340	13.5	13.5	13.5	15.5
χ^2 fitted	68	165	240	333	13.5	15.1	13.8	16.2

where σ_A controls how fast the density falls of with distance Δ from the arm median. As in Higdon & Lingenfelter (2013), the distances Δ are sampled non-uniformly in the range 0.01 kpc − 5 kpc. Notice that the transverse densities given by Equation (3.11) are not normalised. This is intentional, as the transverse densities shall be relative to the arm median density, which is given by

$$P_\rho(\rho) = \mathrm{e}^{-\rho/H_\rho}. \tag{3.12}$$

In addition, Equation (3.11) is also used to determine the fall-off in density at the endpoints of the spiral arms. These densities are calculated using Equation (3.11) with respect to the density of the respective endpoint. Then, the calculated densities are projected in a circular arc of 180° around the endpoint. This ensures a smooth transition at the endpoint to the surrounding medium.

As in the axisymmetric model of Chapter 3.1, the height distribution is given by Equation (3.7) with $\sigma_z = 0.15\,\text{kpc}$. The relative planar density of each spiral arm is given by the Cartesian product $P_\rho(\rho) \times P_\Delta(\Delta)$, and in the calculations, the densities in each spiral arm are calculated for about 10^5 different points.

These relative arm densities cannot be treated equally, however. As will be shown in Chapter 3.2.5, giving the four spiral arms an equal weight is inadequate to reproduce the measured N II intensities. As such, each arm is given a relative weight, f_i, to replicate the observational data more accurately. This is in line with, for instance, Drimmel & Spergel (2001) who made a three-dimensional model fitted to the far-infrared (FIR) and near-infrared (NIR) data measured by COBE/DIRBE and found that the spiral arms Scutum-Crux and Perseus dominated the NIR emission. To improve their model, they found that the Sagittarius-Carina's arm had to be reduced relative to the other arms. Other authors such as Benjamin (2008), Benjamin et al. (2005) and Hou & Han (2015) also support that the Sagittarius-Carina Arm is weaker than the other arms. Steiman-Cameron et al. (2010) also finds that the Scutum-Crux and Perseus arms have significantly stronger emissions than the Sagittarius-Carina and Norma-Cygnus arms.

Thus, each spiral arm will be multiplied with a fractional contribution f_i. As for the spiral arm angles and pitch angles, the values given by Higdon & Lingenfelter (2013) have to be tweaked to fit with the new parameters for the Galaxy, and the obtained values can be found in Table 3.2. Notice that the sum of all fractional contributions only adds to 0.99. This is because we anticipate the inclusion of the Local Arm, which will be described in Chapter 3.2.3.

These spiral arms are, again, calculated in the Galactocentric coordinate system but have to be integrated over latitude b and distance r to achieve an intensity plot

Table 3.2

Name	f_{NC}	f_{P}	f_{SA}	f_{SC}
Higdon & Lingenfelter	0.18	0.36	0.18	0.28
χ^2 fitted	0.19	0.35	0.16	0.29

as a function of longitude l. To facilitate this integration, we interpolate each spiral arm over the entire Galactic plane. The coordinates for each position in the plane are generated in (r, l, b) coordinates, and to achieve a good enough resolution, we have around $5 \cdot 10^7$ points in the Galaxy for which each arm is interpolated over.

Consequently, the size of the generated data is vast. To be as efficient as possible with the available computer resources while ensuring that the model remains accurate, the points above and below the plane are created with a non-uniform angular distance db. As seen from Figure 3.5, the effective thickness of the Galactic disk is very small. Thus, lines of sight with large latitude b will mostly sample empty space, as seen from Figure 3.6. Thus, the lines of sight lying close to the Galactic plane with $|b| \leq 1°$ are sampled from an exponential distribution, and the lines of sight above $|b| = 1°$ are created with a spacing $\mathrm{d}b = 0.2°$. This ensures that the emphasis is kept on the Galactic plane where the majority of the mass lies while also sampling the entire range $|b| \leq 5°$. The spacing between the points along r and l are respectively $\mathrm{d}r = 0.2\,\mathrm{kpc}$ and $\mathrm{d}l = 0.2°$. Along the radial direction r, the maximum distance is $r_{\max} = R_{\mathrm{S}} + 35\,\mathrm{kpc} + 5\,\mathrm{kpc} = 48.178\,\mathrm{kpc}$. This distance is along the line of sight from Earth towards the Galactic centre and ensures that everything of the spiral arms on the other side is considered. The $+\,35\,\mathrm{kpc}$ is the maximum distance from the Galactic centre to the end of the spiral arm medians, and the $+\,5\,\mathrm{kpc}$ is to take into account the transverse part of the Galactic arms.

The procedure for calculating the coordinates (r, l, b) first results in a three-dimensional matrix, with the r coordinates along the first axis, l along the second and b along the third. For the integration, this coordinate matrix is then flattened into a one-dimensional array and transformed into (x, y, z) coordinates with the formulas in Equation (3.4) and the usual equations $x = \rho\cos(\theta)$ and $y = \rho\sin(\theta)$.

As for the axisymmetric model of Chapter 3.1, the source-weighted spiral arm areas have to be calculated,

$$A_i = \int_0^{2\pi} \int_0^{r_{\max}} P_\rho(\rho_j(\rho, \theta)) \times P_\Delta(\Delta)\rho\,\mathrm{d}\rho\,\mathrm{d}\theta, \tag{3.13}$$

where i runs through the spiral arms Norma-Cygnus (NC), Perseus (P), Sagittarius-Carina (SA) and Scutum-Crux (SC). ρ_j is a given point along this spiral arm median as a function of ρ and θ as defined by Equation (3.10). P_Δ remains the same for each spiral arm and every ρ_j, as the transverse density always is relative to the arm median density.

In the code, the coordinates for the spiral arms and the corresponding densities are first calculated in the Galactocentric coordinate system. Then, the arm coordinates

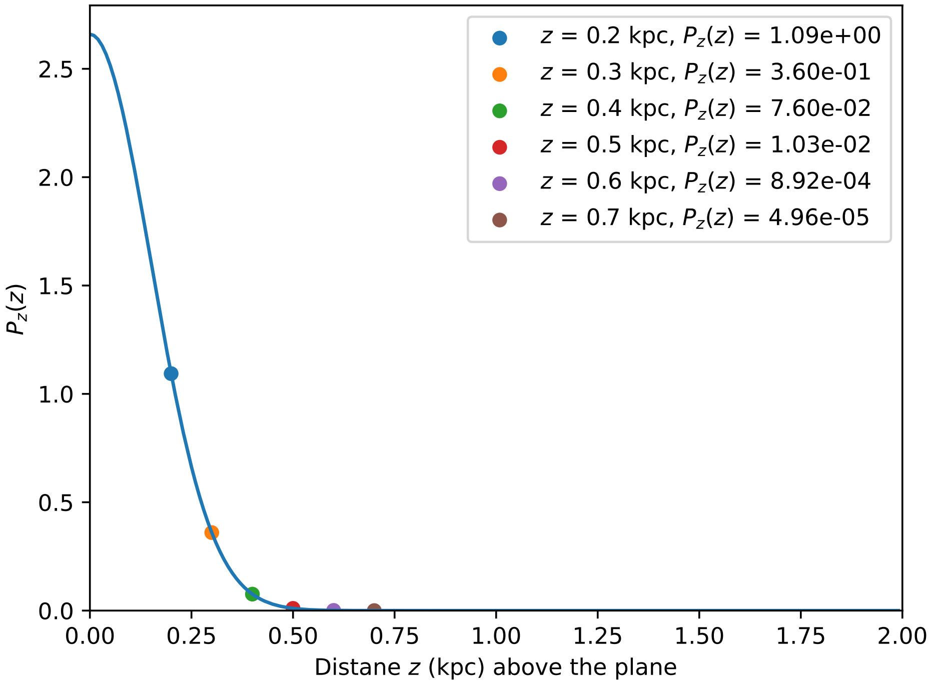

Figure 3.5: The relative density as function of height z in kpc as described by Equation (3.7). Relative densities for selected values for z are shown. At height $z = 0.5\,\text{kpc}$, the density becomes essentially equal to zero.

are converted into (x, y, z) coordinates before the arm densities are interpolated over the entire Galactic plane, which is generated as described above and then integrated up to give A_i.

With the source-weighted spiral arm areas calculated, the interpolated spiral arms can be defined as follows:

$$S_i(\rho, \theta) = f_i P_\rho(\rho_j(\rho, \theta)) \times P_\Delta(\Delta)\rho\,\mathrm{d}\rho\,\mathrm{d}\theta / A_i. \tag{3.14}$$

Each S_i gives the density for each spiral arm at every point in the Galactic plane. Naturally, the arm density is practically zero at large distances from the given arm. As for each A_i, the coordinates and densities are first calculated in the Galactocentric coordinate system before being converted to (x, y, z) coordinates for the interpolation.

Now, the emissivity of each arm can be easily calculated,

$$\epsilon_i(x, y, z) = L S_i(x(\rho, \theta), y(\rho, \theta)) P_z(z), \tag{3.15}$$

where $P_z(z)$ is as defined in Equation (3.7) with the same $\sigma_z = 0.15\,\text{kpc}$. In the same manner as for the axisymmetric model in Chapter 3.1, the modelled line intensities for N II 205 µm are defined as

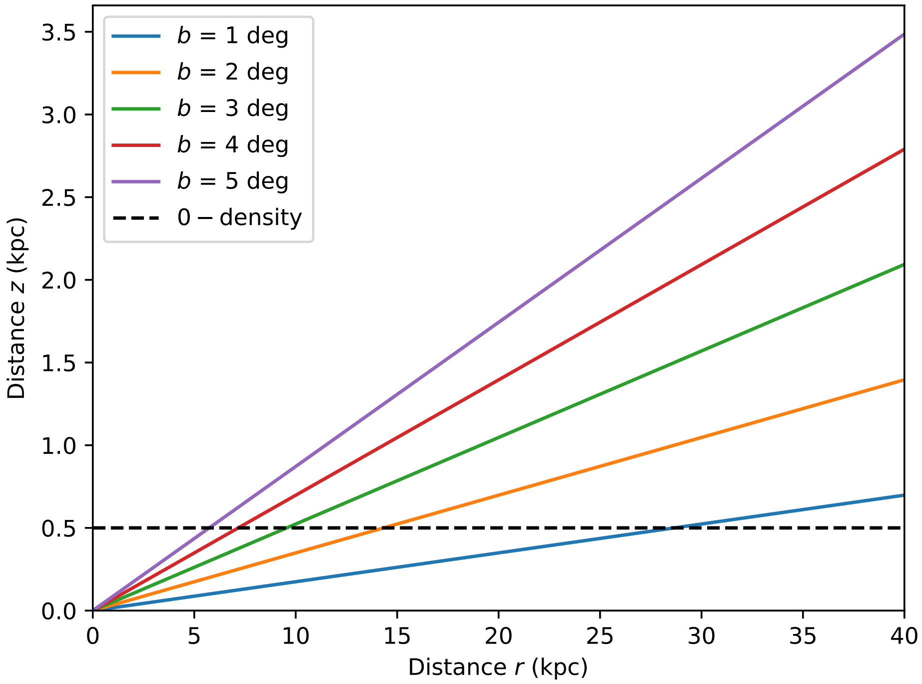

Figure 3.6: Lines of sight for different values for latitude b with the demarcation line for zero-density as found in Figure 3.5 shown. For higher latitudes, the lines of sight sample, for the most part, empty space, while lines of sight with lower values for latitude b sample more of the interior of the Galaxy.

$$I_i(l,b) = \int \frac{\epsilon_i(r,l,b)}{4\pi r^2} r^2 \,\mathrm{d}r. \tag{3.16}$$

As the intensities from Fixsen et al. (1999) are averaged over $\Delta l = 5^\circ$ and $\Delta b = 1^\circ$, we calculate the average intensities as follows,

$$\langle I_i(l,b)\rangle = \frac{1}{\Delta l\,\Delta b}\int_{b=-5^\circ}^{b=+5^\circ}\int_{l=-2.5^\circ}^{l=+2.5^\circ}\int_0^{r_{\max}} \frac{\epsilon_i(r,l,b)}{4\pi r^2}\, r^2 \cos b \,\mathrm{d}r\,\mathrm{d}l\,\mathrm{d}b. \tag{3.17}$$

The average line intensities have units of $\mathrm{erg\,cm^{-2}\,s^{-1}\,sr^{-1}}$, and $r_{\max} = 48.178\,\mathrm{kpc}$, as discussed earlier in the text. The integration limit over b is to take into account the width of the FIRAS beam, as discussed in Chapter 3.1. The division by $\Delta b = 1^\circ$ is due to the assumption that all radiation stems from the 1° wide Galactic plane.

Notice that ϵ_i is changed from $\epsilon_i(x,y,z)$ to $\epsilon_i(r,l,b)$. The emissivity was calculated in terms of (x,y,z) coordinates but has to be transformed into (r,l,b) coordinates to calculate the intensity as seen from Earth. To achieve this coordinate transformation and integration, we first reshape the emissivity array into a three-dimensional matrix of the same size as the original (r,l,b) coordinate matrix. This reshaping of the emissivity array is essentially the coordinate transformation, with radial distance r along axis 0, longitude l along axis 1 and latitude b along axis 2. Then, to perform the integration, one has to sum up this array along axis 0 and 2, and of course, multiply by the step size db and dr to perform the Riemann sum.

The resulting figure for the modelled intensities can be seen in Figure 3.7. In Figure 3.8, the result of Higdon & Lingenfelter (2013) is shown for comparison. As for the axisymmetric model, the spiral arm model in this thesis required a slightly larger value for the total N II 205 µm luminosity than that of Higdon & Lingenfelter (2013). Our model required a total N II luminosity of $1.6 \times 10^{40}\,\mathrm{erg\,s^{-1}}$, whereas the model of Higdon & Lingenfelter required an N II luminosity of $1.4 \times 10^{40}\,\mathrm{erg\,s^{-1}}$. The small difference shows that the two implementations share a general agreement.

As can be seen from the figures, the resulting model from this work more accurately reproduces the observed FIRAS N II intensities by comparing, for instance, the regions towards the Galactic centre. Again, since the work of Higdon & Lingenfelter (2013), a more precise value for the distance between the Earth and the Galactic centre has been calculated, which is used here. Moreover, a more thorough fitting of parameters was carried out in this work, allowing for a more accurate model. There are, however, still regions with significant discrepancies between the observed N II intensities and the modelled one. Some of these regions will be discussed next in the following sections and considered in the model.

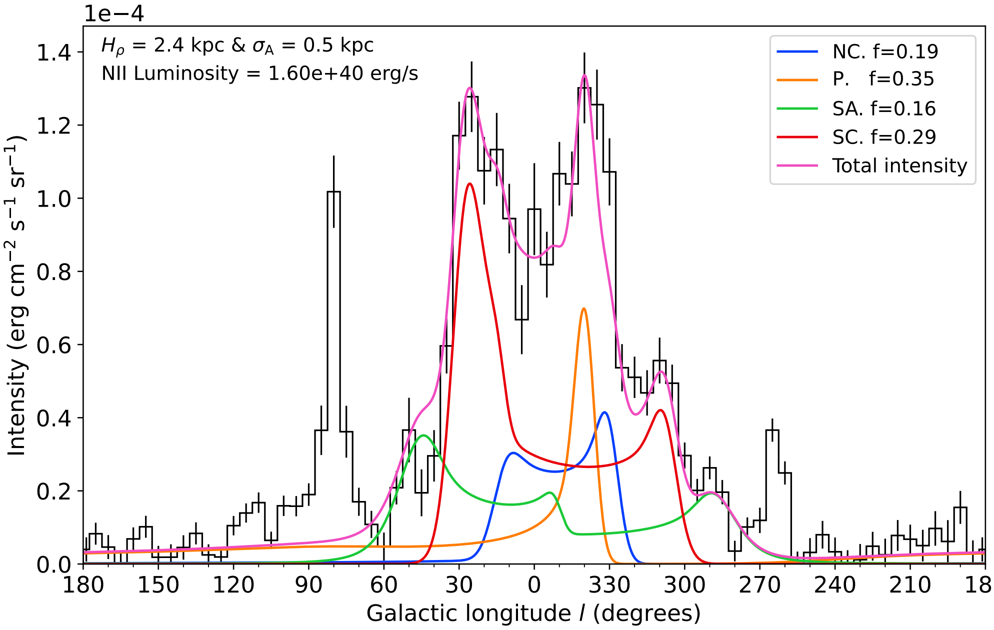

Figure 3.7: N II 205 µm line intensity plot, resulting from the four spiral arm model with a total Galactic N II luminosity $L = 1.6 \times 10^{40}\,\mathrm{erg\,s^{-1}}$. The measured N II line from FIRAS in Figure 5(e) of Fixsen et al. (1999) is shown as a histogram. Notice the fractional contributions sum up to 0.99 in anticipation of the contribution of the Local Arm.

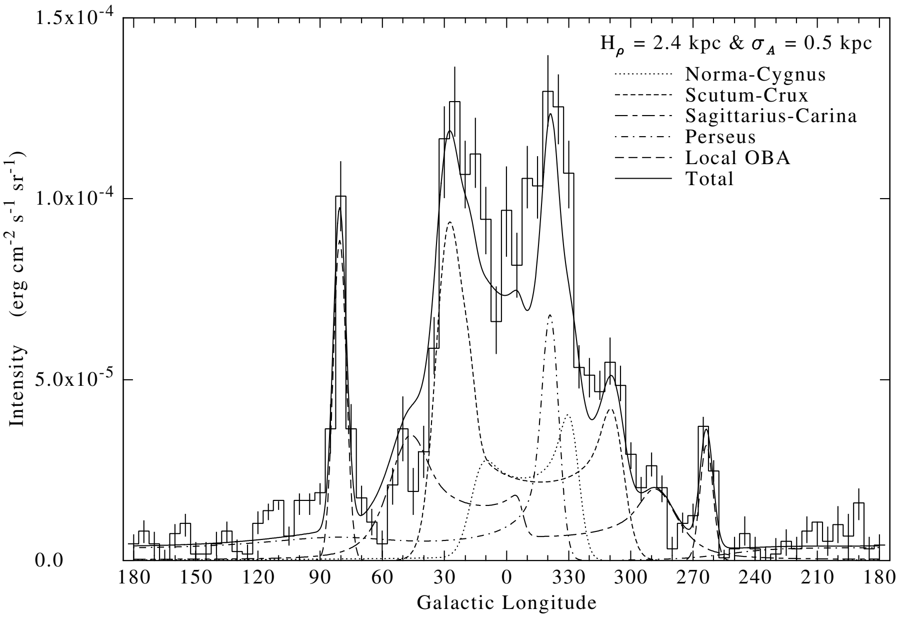

Figure 3.8: N II 205 µm line intensity plot, resulting from the spiral arm model of Higdon & Lingenfelter (2013) as shown in their Figure 6 with a total Galactic N II luminosity $L = 1.4 \times 10^{40}\,\mathrm{erg\,s^{-1}}$. Contributions from the Cygnus X region and Gum Nebula are also included. The measured N II line from FIRAS in Figure 5(e) of Fixsen et al. (1999) is shown as a histogram.

3.2.1 Cygnus region

As discussed in Chapter 2, the Cygnus region is a massive star forming region of our Galaxy, containing several OB associations and hundreds of OB stars (Quintana & Wright 2021; Wright 2020). The most massive of these associations is the well-known Cyg OB2 association, which contains at least 50 O stars. Cyg OB2 is embedded in the large star forming region called Cygnus X located at $l \simeq 80°$, $b \simeq 0.8°$ (Rygl et al. 2012; Wright 2020; Wright, Drew et al. 2015). Hanson (2003) calculated the distance to Cyg OB2 as 1.45 kpc, which is in excellent agreement with the estimate on the distance to Cygnus X of 1.40 ± 0.08 kpc by Rygl et al. (2012). Cygnus X is $\sim 10°$ large (Reipurth & Schneider 2008), or ~ 200 pc across. In Figure 1 of Wright, Drew et al. (2015), a 4×3 deg^2 portion of Cygnus X is shown together with Cyg OB2.

Being so rich in massive stars, Cygnus X is a feature clearly visible in the sky and has been known for a long time. For instance, Reipurth & Schneider (2008) write that Cygnus X is so bright that it is clearly visible in the radio skymaps of Reber (1944). Piddington & Minnett (1952) named this source after detecting a large region with thermal spectrum in their radio data to distinguish it from the radio source Cyg A.

The bright feature in the FIRAS data at $l \approx 80°$ will thus be interpreted as the star forming region Cygnus X. Following Higdon & Lingenfelter (2013), this feature is then modelled as a uniform sphere located at $l = 80°$, $b = 0°$ with a radius of $R = 75\,\mathrm{pc}$, corresponding to an angular width of $\sim 12°$. It is assumed that this source is resolved against the Galactic plane. To mimic the effect of the 7° FIRAS beam, the modelled intensities from Cygnus X was weighted over a normal distribution with a full width at half maximum of 7°. In the same manner as for the spiral arm intensities, the contribution from the Cygnus X region was averaged over $\Delta l = 5°$ and $\Delta b \simeq 5.9°$, with Δb being the angular extent of the source instead of $\Delta b = 1°$.

The effect of including Cygnus X to the N II intensities profile can be seen in Figure 3.10. The implementation of the Cygnus X region in this work required an N II luminosity for Cygnus X to be $2.4 \times 10^{37}\,\mathrm{erg\,s^{-1}}$, which is identical to the value obtained by Higdon & Lingenfelter (2013). They also calculated that the total ionising luminosity, Q_0, required to produce the diffuse thermal radio emission from Cygnus X was $0.45 \times 10^{51}\,\mathrm{s^{-1}}$, of which 45% was required to power the N II line emission estimated for Cygnus X.

3.2.2 Gum Nebula

The bright feature in the FIRAS data at $l \approx 260°$ is interpreted as the H II region known as the Gum Nebula, first discovered by Gum (1952). This H II region is primarily excited by the massive runaway O4I star ζ Puppis and the binary γ^2 Velorum in the Vela OB2 association, the latter being composed of a massive O star and a Wolf-Rayet star (Reynolds 1976).

γ^2 Velorum is located at $l = 262.8°$, $b = -7.7°$ (Maíz-Apellániz et al. 2004) and is by far its most massive and brightest member of Vela OB2. γ^2 Velorum is located at a distance of $368^{+38}_{-13}\,\mathrm{pc}$ from Earth (Millour et al. 2007). The approximately one square degree region around γ^2 Velorum is well known for its rich population in low-mass PMS stars (see, e.g., Armstrong, Wright, Jeffries & Jackson 2020; Jeffries et al. 2014). In Figure 3 of Armstrong, Wright & Jeffries (2018), a density map of the PMS stars in Vela OB2 together with known OB stars highlights the high density around γ^2 Velorum, which is found as the most dense region. Their figure is also given here in Figure 3.9.

ζ Puppis is located at $l = 256°$, $b = -4.7°$ (Maíz-Apellániz et al. 2004) at a distance of $332 \pm 11\,\mathrm{pc}$ (Howarth & van Leeuwen 2019). This star is the closest O star to the Sun and one of the brightest stars in the night sky, making it one of the best-studied massive stars across all wavebands (Gunderson et al. 2024; Schilbach & Röser 2008). ζ Puppis is a runaway star which most likely originated from the Trumpler 10 region some 2.5 Myr ago (Hoogerwerf et al. 2001; Schilbach & Röser 2008).

Following Higdon & Lingenfelter (2013), the feature in the FIRAS data at $l \approx 260°$ will here be modelled as a single spherical source located $l = 262°$, $b = 0°$ at a distance of 330 pc. As for Cygnus X, the Gum Nebula will be weighted over a normal distribution with a full width at half maximum of 7° to simulate the effect of the FIRAS beam. It will also be averaged over $\Delta l = 5°$ and $\Delta b \sim 10.4°$, with Δb being

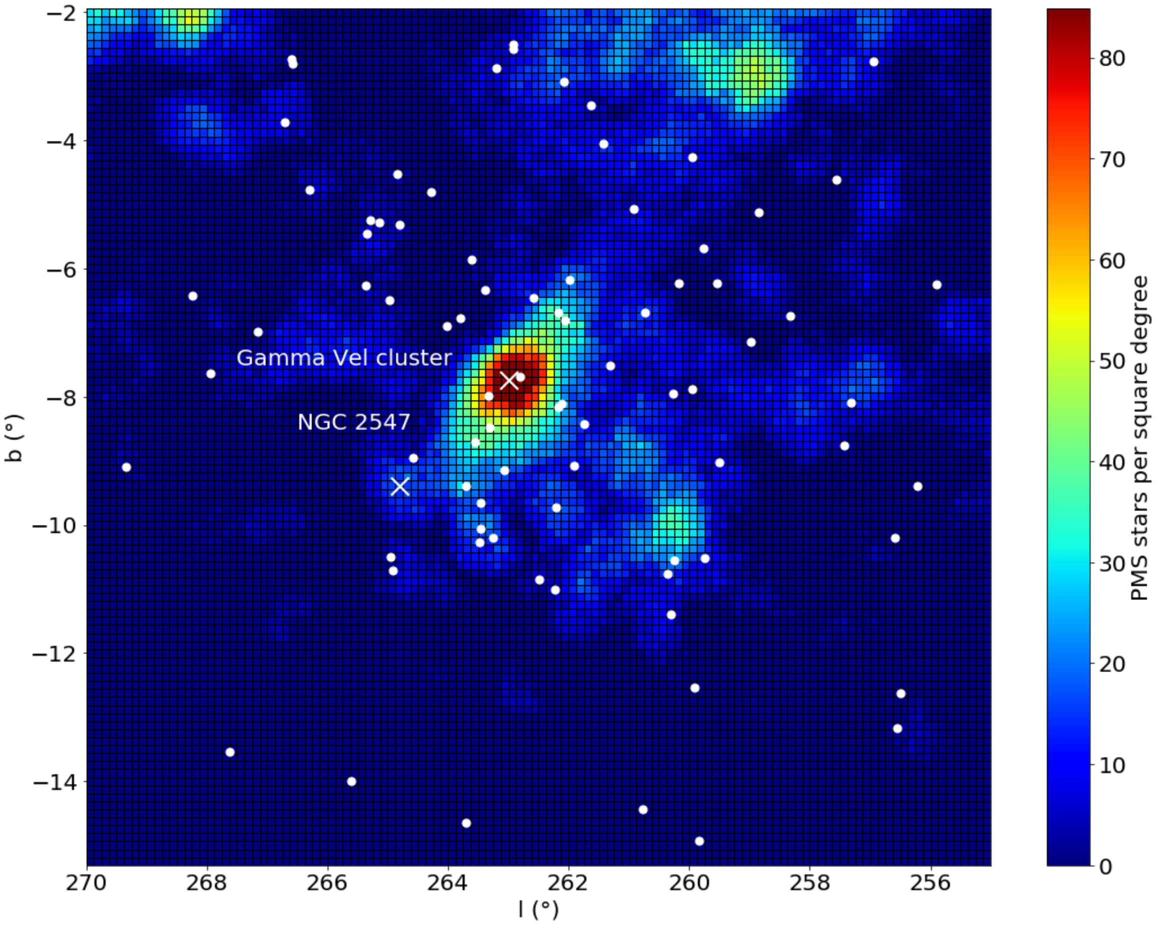

Figure 3.9: PMS density map of the Vela OB2 association. γ^2 Velorum is seen in the middle of the map, and 82 OB associations from de Zeeuw et al. (1999) are shown as white dots. The figure is taken from Armstrong, Wright & Jeffries (2018).

the angular extent of the source instead of $\Delta b = 1°$.

The inclusion of the Gum Nebula to the N II intensity profile can be seen in Figure 3.10. The implementation of the Gum Nebula in this work required an N II luminosity for the Gum Nebula to be $1.2 \times 10^{36}\,\mathrm{erg\,s^{-1}}$, which is slightly higher than the value of $1 \times 10^{36}\,\mathrm{erg\,s^{-1}}$ obtained by Higdon & Lingenfelter (2013). Of the total ionising luminosity of ζ Puppis and the binary γ^2 Velorum, Higdon & Lingenfelter (2013) found that ζ Puppis contributed $\sim 80\%$ of it, and that only 10% of the ionising luminosity from the three stars mentioned here was required to power the N II luminosity observed by FIRAS towards the Gum nebula.

3.2.3 Local Arm

The four major arms which have been the main focus thus far have been known to exist for a long time, and countless models for them exist in the literature. Moreover, between the Perseus and Sagittarius-Carina arms, star forming regions have been known for a long time to exist, a region which has been called the 'Orion spur', 'Orion

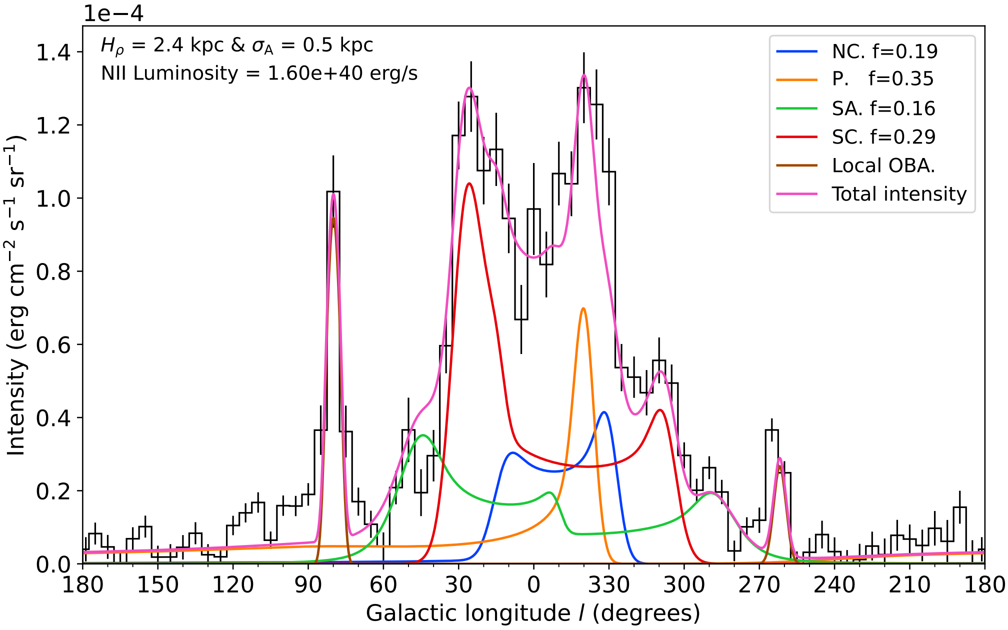

Figure 3.10: N II 205 µm line intensity plot, resulting from the four spiral arm model with a total Galactic N II luminosity $L = 1.6 \times 10^{40}\,\mathrm{erg\,s^{-1}}$. The Cygnus X region and Gum Nebula have been added with an N II luminosity of $2.4 \times 10^{37}\,\mathrm{erg\,s^{-1}}$ and $1.2 \times 10^{36}\,\mathrm{erg\,s^{-1}}$, respectively. The measured N II line from FIRAS in Figure 5(e) of Fixsen et al. (1999) is shown as a histogram. Notice the fractional contributions sum up to 0.99 in anticipation of the contribution of the Local Arm.

arm' and 'Local Arm' (e.g., Georgelin & Georgelin 1976; Vallée 2002). Xu et al. (2013) find that the Local Arm is indeed an arm, possibly originating from the Perseus Arm.

Hou & Han (2014) recently investigated the spiral structure of the Milky Way, employing data from more than 2500 known H II regions, 1300 giant molecular clouds (GMCs), and 900 6.7 GHz methanol masers. They found that a model with four major spiral arms and a Local Arm best fitted the data. They recommended the model fitted to only the H II data, as the distances to GMCs in the second and third quadrants were unreliable. Their model parameters can be found in their Table 1, which was calculated for both $R_\mathrm{S} = 8.5\,\mathrm{kpc}$ and $R_\mathrm{S} = 8.3\,\mathrm{kpc}$. The Local Arm begins near the Perseus Arm and extends past the Sun towards the Sagittarius-Carina Arm. The parameters from Hou & Han (2014) for the Local Arm together with a value for the fractional contribution and the result from the reduced χ^2 fitting are given in Table 3.3. It should be noted that $\theta_{0,\mathrm{LA}}$ and p_LA were not subject to the fitting procedure as these model parameters are so recent, and that the contribution of the Local Arm is small compared to the major spiral arms and a fitting procedure of all parameters could lead to overfitting. The value for $\theta_{\max,\mathrm{LA}}$ is not found in Table 1 in Hou & Han (2014), but rather as a crude estimate in the text, and was thus subject to the fitting procedure.

The result of adding the Local Arm to the model can be seen in Figure 3.11.

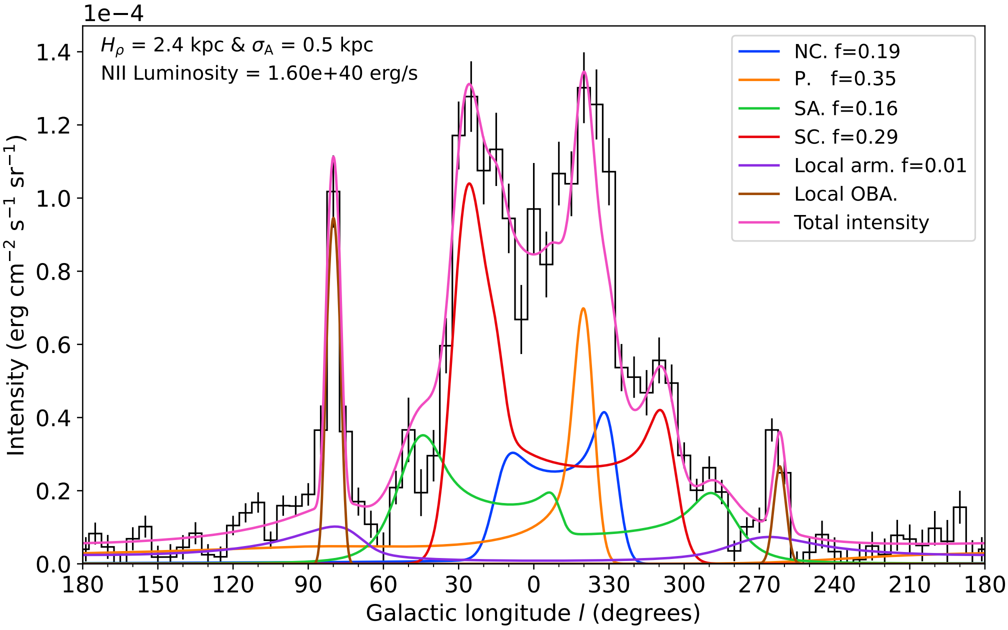

Figure 3.11: N II 205 μm line intensity plot, resulting from the four spiral arm model with a total Galactic N II luminosity $L = 1.6 \times 10^{40}$ erg s^{-1}. The Cygnus X region and Gum Nebula have been added with an N II luminosity of 2.4×10^{37} erg s^{-1} and 1.2×10^{36} erg s^{-1}, respectively. The Local Arm has also been added. The measured N II line from FIRAS in Figure 5(e) of Fixsen et al. (1999) is shown as a histogram.

Table 3.3

Name	$\theta_{0,\mathrm{LA}}$	$\theta_{\mathrm{max,LA}}$	p_{LA}	f_{LA}
Hou & Han	55.1	110	2.77	
χ^2 fitted	55.1	107	2.77	0.01

Its most notable contribution to the resulting N II line intensity plot is the region $l \approx 70°$ and $l \approx 110°$. The inclusion of the Local Arm also contributes towards the Gum Nebula, increasing the total modelled N II intensities to match the observed data. The inclusion of the Local Arm lowered the reduced χ^2 from 16.72 to 12.47, the calculation of which is detailed in Chapter 3.2.5. Contrary to the conclusion of Higdon & Lingenfelter (2013), we thus note that including the Local Arm improves the model considerably. Also, note that the Local Arm has been included in other models in the literature, such as Xie et al. (2024), who modelled the radial distribution of pulsars in the Milky Way.

3.2.4 Regarding the devoid region of Sagittarius

Investigating the figures of the modelled N II intensities from the spiral arm model, it is clear that the model is overestimating the intensities in the range $l = 20°$ to $l = 65°$. This portion of the Sagittarius arm has been known for a long time to be devoid of optical tracers and to suffer from heavy extinction. When looking at old spiral arm models for the Galaxy (e.g., Georgelin & Georgelin 1976), the Sagittarius-Carina Arm abruptly ceases in this region. Georgelin & Georgelin (1976) writes that the Sagittarius-Carina Arm cannot be followed with optical data beyond $l = 36°$ due to absorption. Instead, they have to use radio data, whose intensity reaches a maximum at $l = 50°$.

Forbes (1983, 1984, 1985) investigated the region between $l = 30°$ and $l = 70°$, and attributed this lack of optical tracers to heavy extinction as well as a lack of spiral arm tracers. He discussed that high degrees of extinction combined with historical neglect of this region have contributed to biases in maps of arm tracers and that there are intrinsic gaps in the spiral arm structure. Crampton & Georgelin (1975) also attributed the lack of optically studied H II tracers between $l = 32°$ and $l = 50°$ due to very high absorption. Forbes finds that the majority of the extinction appears between $r = 0.5\,\text{kpc}$ and $r = 1\,\text{kpc}$, with the most heavily obscured region appearing between $l = 32°$ and $l = 44°$. The most transparent regions had an extinction in the visual band of $A_V \approx 2.4$ mag at 4 kpc between $l = 28° - 32°$ and $l = 62° - 70°$.

A specific portion of the arm in this direction was selected to model this devoid region, and the corresponding σ_d was reduced. σ_d determines how fast the density decreases transverse the arm median in the devoid region in the same manner as σ_A does in Equation (3.11). This effectively made the density transverse the arm median of this portion of the arm fall off more quickly. Since the current model accurately represents the observed arm tangent, reducing the surrounding density while keeping the arm tangent intact would be a better approach than simply decreasing the modelled densities of the entire arm segment.

As shown in Figure 3.12, the resulting Sagittarius-Carina Arm matches the observed intensities in this region to a greater extent. The devoid region is defined by the parameters ρ_min, ρ_max and σ_d, with ρ_min determining the closest distance from the Galactic centre to the devoid region, and ρ_max determining the other edge furthest away from the Galactic centre. Table 3.4 lists the fitted parameters for the devoid region. As for the inclusion of the Local Arm, incorporating the devoid region improved the overall fit for the model, lowering the reduced χ^2 from 12.47 to 11.25.

Table 3.4

Name	ρ_min	ρ_max	σ_d
χ^2 fitted	5.1	7.0	0.25

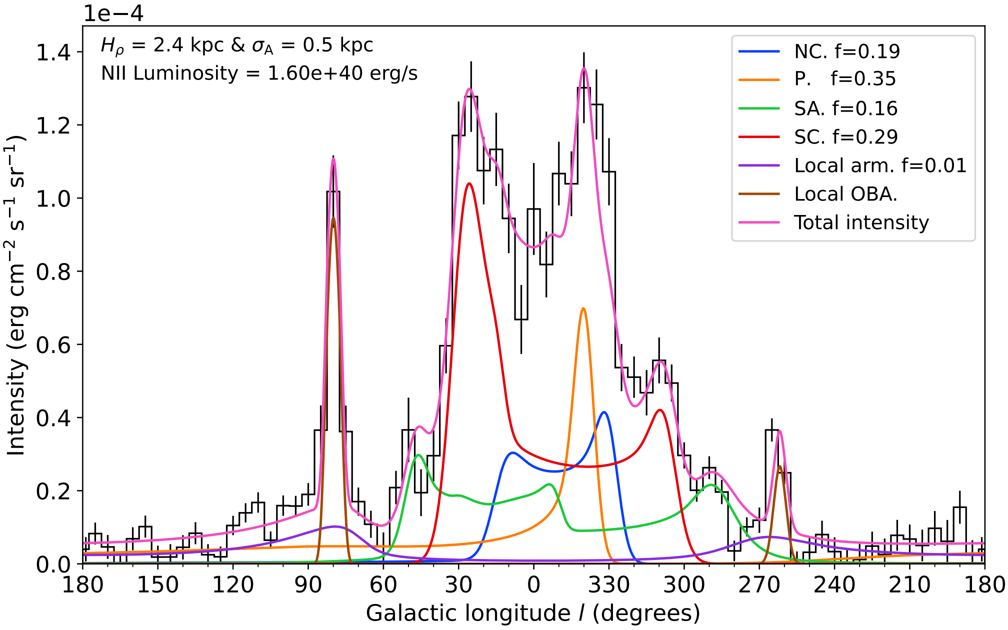

Figure 3.12: N II 205 µm line intensity plot, resulting from the four spiral arm model with a total Galactic N II luminosity $L = 1.6 \times 10^{40}$ erg s^{-1}. The Cygnus X region and Gum Nebula have been added with an N II luminosity of 2.4×10^{37} erg s^{-1} and 1.2×10^{36} erg s^{-1}, respectively. The Local Arm has also been added together with the devoid region of Sagittarius. The measured N II line from FIRAS in Figure 5(e) of Fixsen et al. (1999) is shown as a histogram.

3.2.5 Fitting parameters

As mentioned in this chapter, the parameters for the model had to be fitted to reproduce the observed N II luminosity more accurately. As a goodness of fit the reduced χ^2 was used:

$$\chi^2 = \frac{1}{N-m} \sum_i^N \frac{(O_i - C_i)^2}{\sigma_i^2}, \tag{3.18}$$

where O_i are the observed intensities, C_i the calculated intensities from the model and σ_i^2 the variance. N is the number of data points and m is the number of fitted parameters. In the final version of the model, $N = 1800$ and $m = 40$. With so many parameters, testing out all different combinations is an unfeasible exercise. Instead, the parameters used in Higdon & Lingenfelter (2013) were taken as a starting point and adjusted by eye until the model became reasonable compared to the observed FIRAS data. The assumption is then that this eyeballed model would be fairly close to the actual minima; thus, the range of values for the parameters to be tested would be small.

For instance, in the code, the four major spiral arm angles would be varied by ±1°, and all $4^3 = 64$ resulting models would be calculated. The set of arm angles which resulted in the smallest reduced χ^2 value would be kept and passed on to the following function varying, for instance, the pitch angles. In a similar manner, the fractional contributions, parameters for the devoid region of the Sagittarius-Carina Arm, maximum angle θ for the Local Arm, H_ρ and σ_A would be varied around the existing parameter values and the best set of parameters passed on to the following function, constantly varying the parameter values around the previously calculated best set of parameters. This algorithm would loop until the model converged to a minimum in the reduced χ^2.

As is evident from the figures, the observed FIRAS N II intensities varies quite a lot as a function of longitude. Some of these spikes correspond to spiral arm tangents, for instance, at longitudes $l = 50°$, $l = 25°$ and $l = 340°$, and as already discussed, some regions have enhanced densities and some are devoid of gas. Even though the model has 40 parameters, it remains relatively simple, and there are several regions where the model overestimates and underestimates the N II intensities. Perhaps the most notable examples of such regions are the bins at $l = 2.5°$ and $l = 280°$. As the deviations from the model with the observed data are so prominent at specific bins, the algorithm for optimising the parameters would favour parameters which would minimise these large deviations at the expense of other features of the spiral arms. The most notable examples of this behaviour were the skewing of the Sagittarius-Carina Arm to minimise the gap $l = 280°$ at the expense of its spiral arm tangents, and favouring a significant fractional contribution for Norma-Cygnus at the expense of Perseus to minimise the gap at $l = 330°$ and $l = 350°$. As already discussed from observations, we know that Perseus and Scutum-Crux are the most luminous arms, rendering the latter solution incompatible with observations.

As such, several bins had to be removed from the calculation of the reduced χ^2 to optimise parameters to keep the model reasonable compared to observations. These were the bins at $l = 5°$, $l = 45°$, $l = 275°$, $l = 280°$, $l = 330°$, $l = 335°$ and $l = 350°$. However, the listed reduced χ^2 values in the following figures are calculated from all of the data — the listed bins were only left out for the fitting process. These bins are highlighted in Figure 3.13.

In the following, the N II intensities will be calculated for many different values of the parameters to showcase that the adopted values are optimal, and to get a feel for how the intensity plot changes with the parameters. The contributions of the local OB associations, the Local Arm, and the devoid region of Sagittarius-Carina are included in the following figures. The achieved best-fit values, as shown in the previous tables, are used for the parameters not being varied in the given Figure.

In Figure 3.14, the starting angles for the four major spiral arms are varied, and five different sets of spiral arm angles are showcased. For all but the fourth set, the adopted values illustrated with the blue line achieve the lowest value for the reduced χ^2. The fourth solution, even though it has a lower value for the reduced χ^2, has to be discarded due to the arm tangents at $l = 50°$ and $l = 290°$ not being visible.

Figure 3.15 shows the N II intensities for five different sets of pitch angles for the four major spiral arms. The adopted values shown with the blue line achieve the lowest reduced χ^2. This figure also illustrates that the Sagittarius-Carina Arm is sensitive to

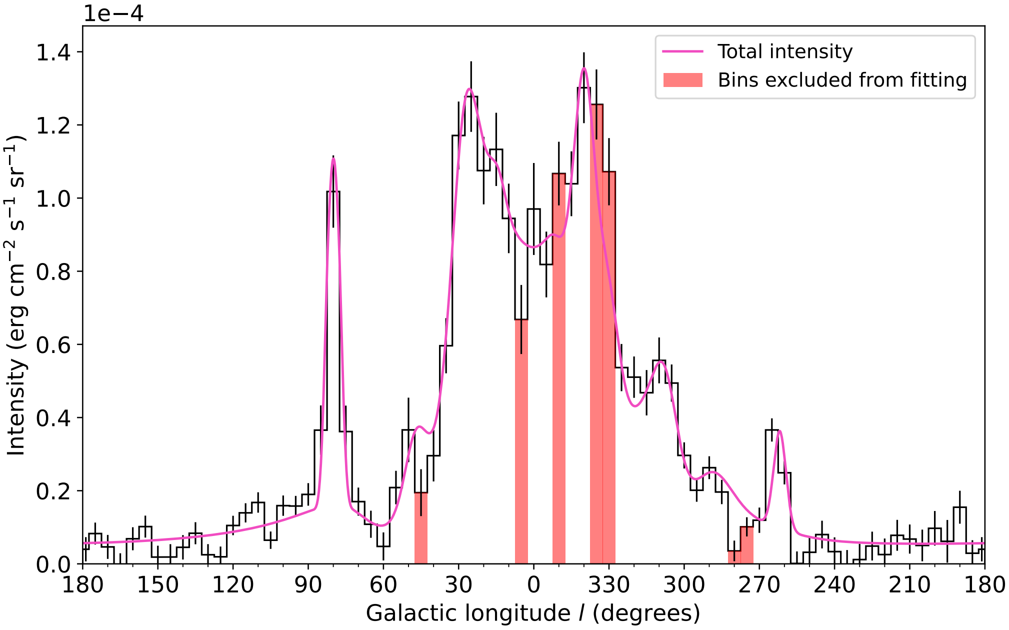

Figure 3.13: N II 205 µm line intensity plot, together with the bins removed from the fitting procedure highlighted. This plot has been prepared in the same manner as Figure 3.12

an increased pitch angle.

In Figure 3.16, the fractional contributions for the four major spiral arms are varied, and the N II intensities are shown for four different sets of these values. The adopted values in blue give the lowest reduced χ^2, and this plot also illustrates how an equal-weighted spiral arm model would be unable to reproduce the observed N II intensities. Also, note that the sum of the fractional contributions for each set sums to 0.99 as the Local Arm is included and is being weighted by 0.01.

In Figure 3.17, the resulting N II intensities for five different values for the N II density scale length H_ρ is shown. Figure 3.18 shows the resulting N II line intensities for five different values of σ_A. These figures illustrate that the values $H_\rho = 2.4\,\mathrm{kpc}$ and $\sigma_\mathrm{A} = 0.5\,\mathrm{kpc}$ creates the best fit to the observed FIRAS N II intensities. These are also the same values that Higdon & Lingenfelter (2013) achieved for their implementation.

In Figure 3.19, the N II intensities are calculated for three different sets of the parameters ρ_min, ρ_max and σ_d for the devoid region of the Sagittarius-Carina Arm. As this is a relatively small region, the changes in the intensity plot are quite subtle. Nevertheless, the values $\rho_\mathrm{min} = 5.1\,\mathrm{kpc}$, $\rho_\mathrm{max} = 7.0\,\mathrm{kpc}$ and $\sigma_\mathrm{d} = 0.25\,\mathrm{kpc}$ results in the best fit. In Figure 3.20, the N II intensities are calculated for three different values for the maximum angle for the Local Arm. Here, the changes to the plot are even more subtle, but for the three values considered, $\theta = 107°$ fits best. It is worth commenting that in other tests, even smaller values for this angle made for slightly better fits, but considering that Hou & Han (2014) wrote the Local Arm extended to approximately $\theta = 110°$, it seems implausible that the angle should be much smaller than $\theta = 107°$.

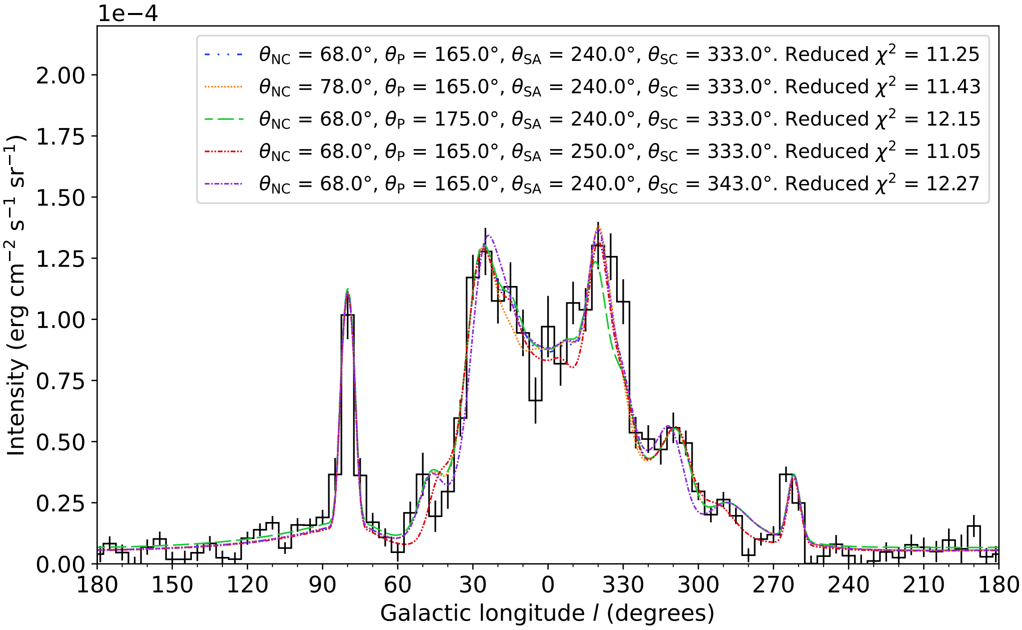

Figure 3.14: The N II line intensities are shown for five different sets of arm angles for the four major spiral arms. Otherwise, the plot is prepared in the same manner as in Figure 3.12.

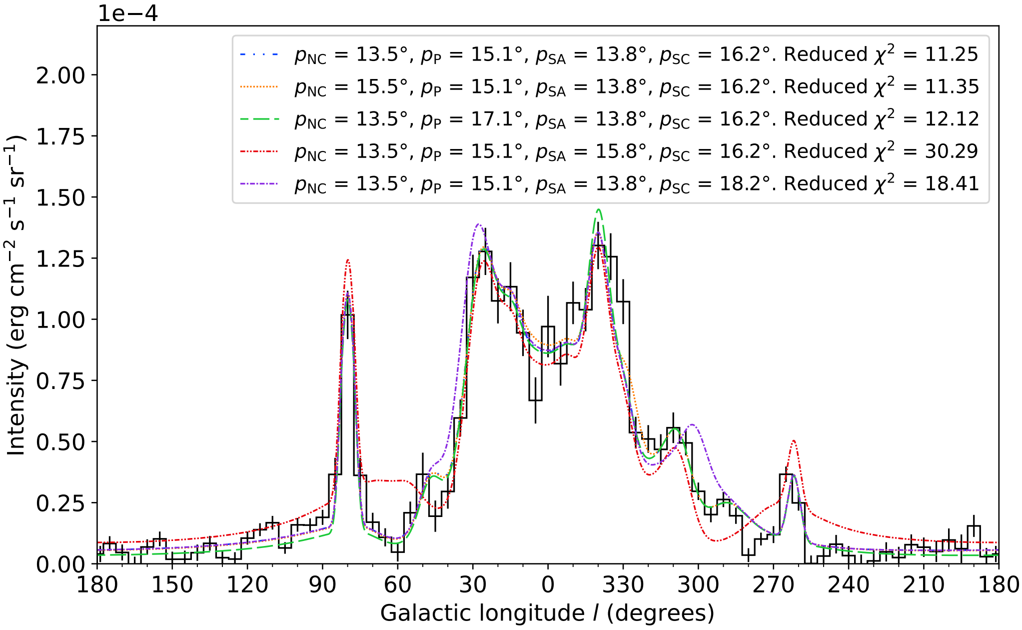

Figure 3.15: The N II line intensities are shown for five different sets of pitch angles for the four major spiral arms. Otherwise, the plot is prepared in the same manner as in Figure 3.12.

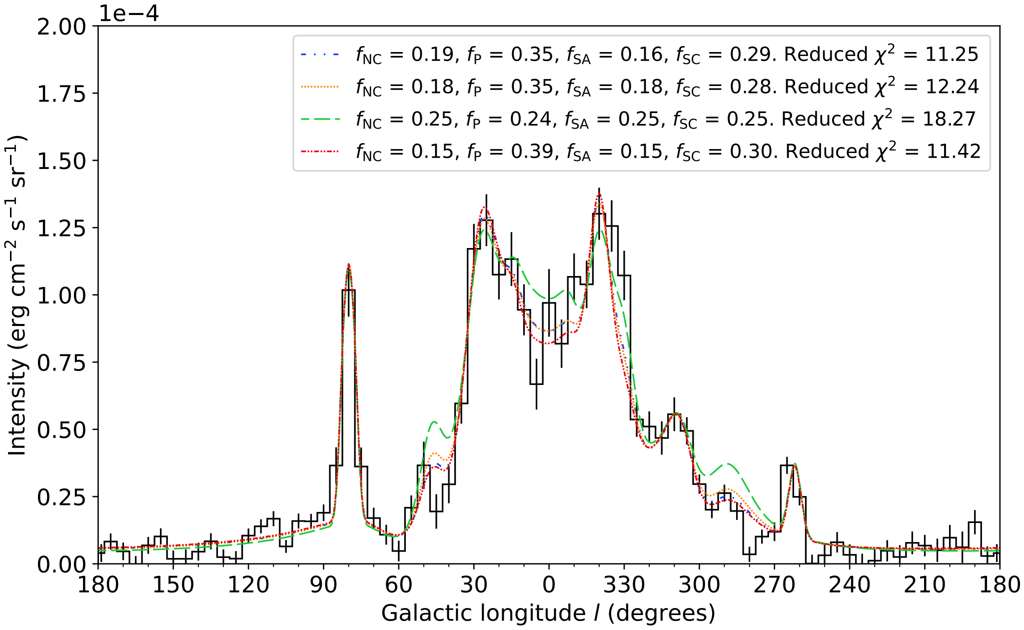

Figure 3.16: The N II line intensities are shown for four different sets of fractional contributions for the four major spiral arms. Otherwise, the plot is prepared in the same manner as in Figure 3.12.

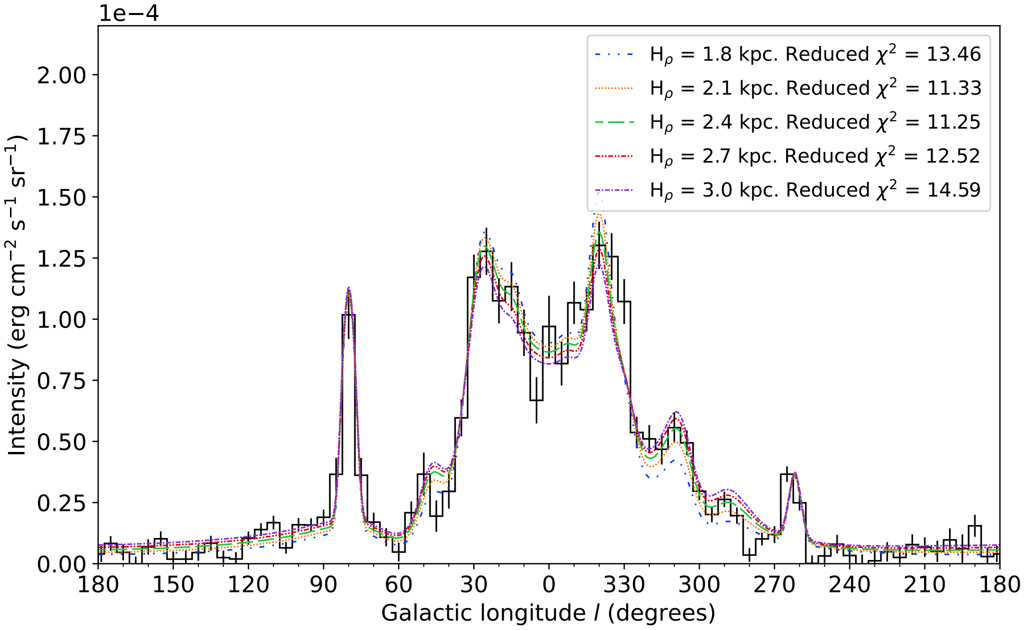

Figure 3.17: The N II line intensities are shown for five different values for H_ρ. Otherwise, the plot is prepared in the same manner as in Figure 3.12.

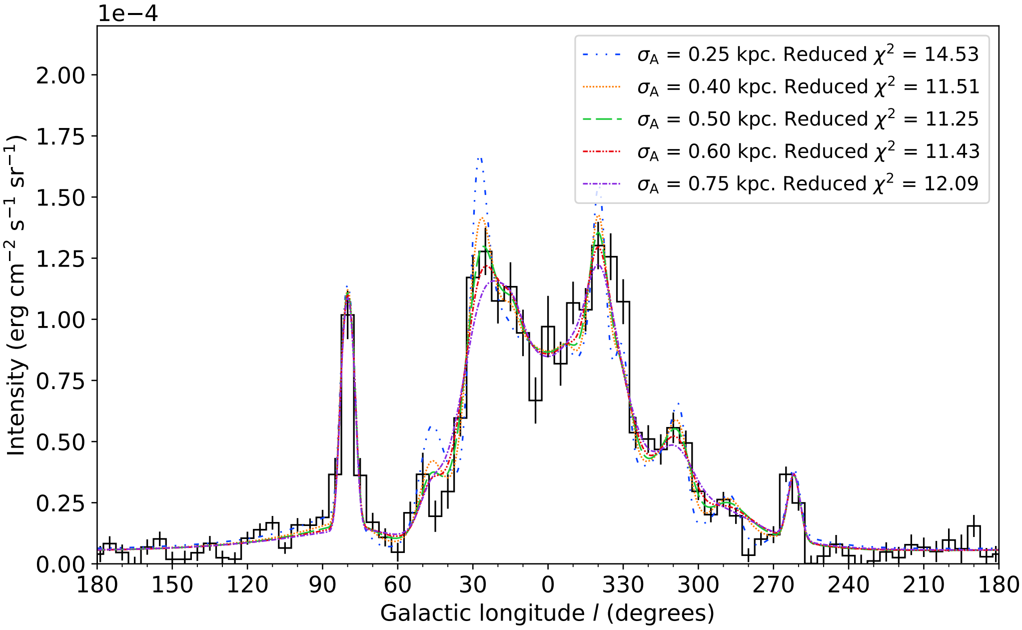

Figure 3.18: The N II line intensities are shown for five different values for σ_A. Otherwise, the plot is prepared in the same manner as in Figure 3.12.

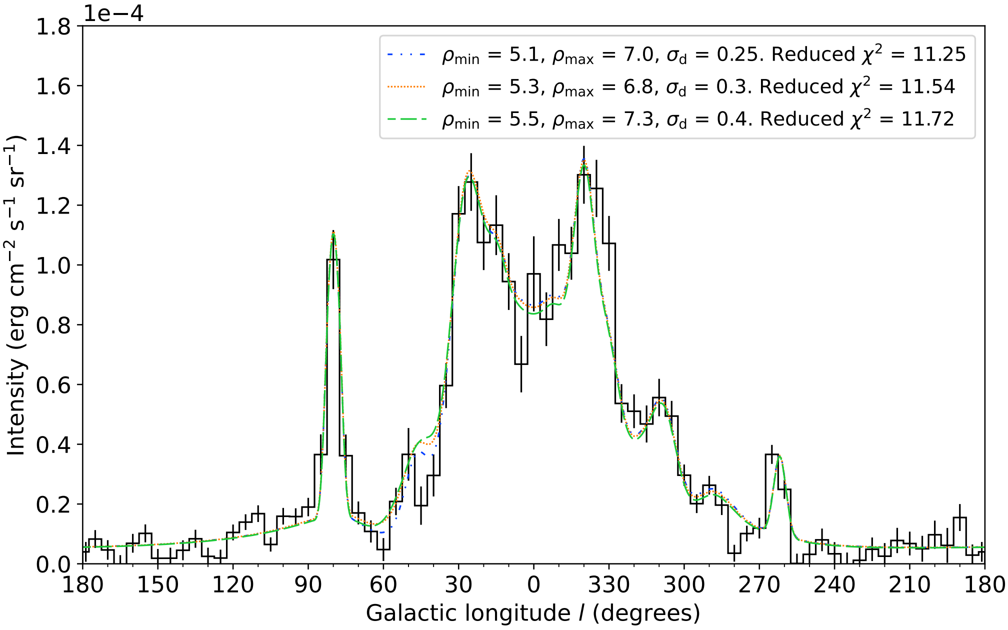

Figure 3.19: The N II line intensities are shown for three different sets of parameters for the devoid region of Sagittarius-Carina. Otherwise, the plot is prepared in the same manner as in Figure 3.12.

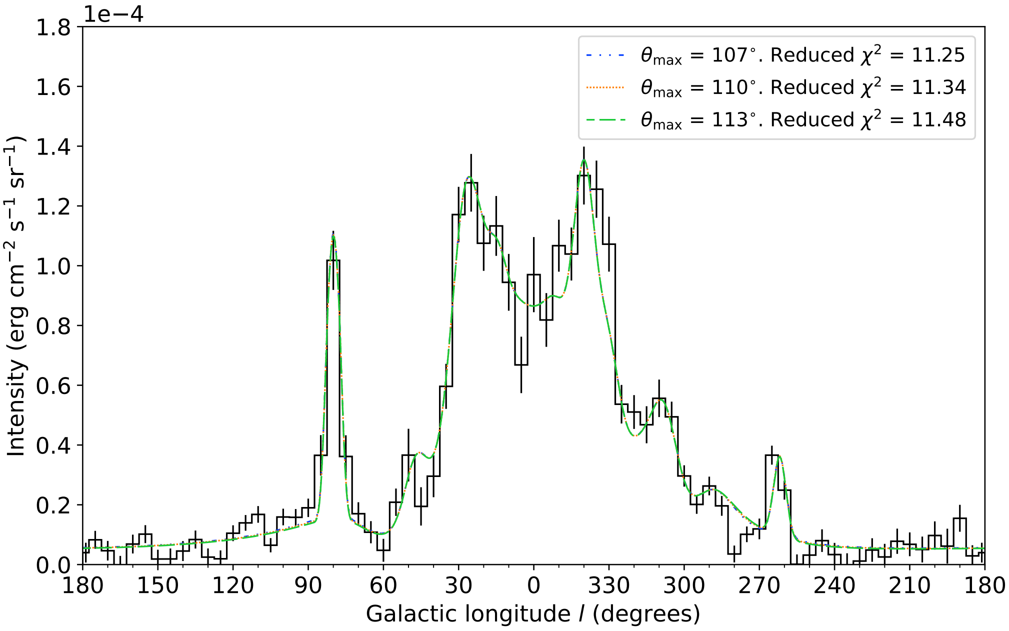

Figure 3.20: The N II line intensities are shown for three different values for the maximum angle for the Local Arm. Otherwise, the plot is prepared in the same manner as in Figure 3.12.

Chapter 4

Simulation of OB Associations

As is evident from Chapter 2, most of the observed OB associations are located relatively close to Earth, and those which are the best studied are either very close to Earth or very rich in stars. OB associations are likely not an unique, local feature of our Galaxy but rather distributed throughout the Milky Way, waiting to be discovered. The main reason we have only sampled the closest OB associations is by their nature; by definition, OB associations are groups of OB stars which are gravitationally unbound, meaning there are great distances between each star as opposed to globular clusters, for instance. This makes it challenging to observe the association the further away it is located and to distinguish member stars from field stars.

Since the primary goal of this work is to model past Galactic supernovae, we cannot solely rely on observational data due to observational bias. Thus, in Chapter 4.1, we will employ our model of the Milky Way as a probability distribution for the location of Galactic OB associations, which we will populate with OB stars and then simulate their eventual demise. Then, in Chapter 4.2, we will combine this model with the known associations from Chapter 2, constructing a comprehensive model of the Galactic OB associations.

4.1 Modelled associations

In Chapter 3.2, the model for the Milky Way was generated with a value for the density scale length $H_\rho^{\mathrm{N\,II}} = 2.4\,\mathrm{kpc}$, which gave the best fit to the observational data. However, as discussed in Chapter 3.1, the hydrogen to nitrogen ratio gradient causes the N II emission to not scale with the Lyc emission, as described by Equation (3.2). Thus, when simulating the location of OB associations, the scale length for the Lyc emission, $H_\rho^{\mathrm{lyc}} = 3.5\,\mathrm{kpc}$, will instead be used. This is the same value McKee & Williams (1997) used, and the value which gave $H_\rho^{\mathrm{N\,II}} = 2.4\,\mathrm{kpc}$.

Figure 4.1 shows a density map of the modelled spiral arm Lyc emissivity. The spiral arms are generated as described in Chapter 3.2 with $H_\rho^{\mathrm{lyc}} = 3.5\,\mathrm{kpc}$. The Local Arm, devoid region of Sagittarius-Carina and the location of the Sun and Galactic centre are also shown. In this density map, the values have been scaled so that the brightest region has a value of one. In the code, there are settings for whether or not

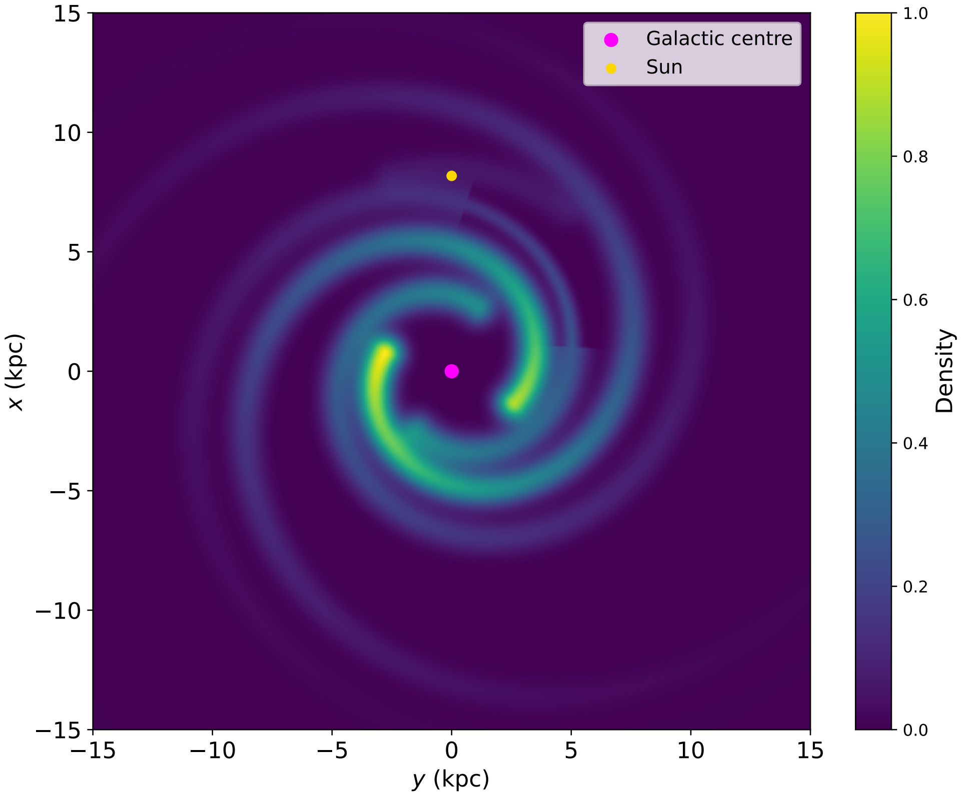

Figure 4.1: Density map of the Milky Way for the spiral arm Lyc distribution, which is expected to represent OB associations' location and superbubbles. The spiral arms were generated as described in Chapter 3.2, with $H_\rho^{\mathrm{lyc}} = 3.5\,\mathrm{kpc}$ and $\sigma_\mathrm{A} = 0.5\,\mathrm{kpc}$. Also, the Local Arm and the modelled devoid region of Sagittarius-Carina are shown. The location of the Sun and Galactic centre is also highlighted, and the density map is normalised such that the brightest area has a value of one.

to add the Local Arm to the devoid region so that the user can easily switch them on or off. Also, note that the Gum Nebula and Cygnus X are not visible in this plot. This is on purpose, as these bright regions will be taken care of in Chapter 4.2.

When the code is run, the user can input the number of Myrs for which they wish to simulate past OB associations and supernovae. For instance, if the input is 10 Myr, the simulation will begin 10 Myr in the past and draw new OB associations every Myr up until the present. This is so that the model generates associations that could have produced cosmic rays that are observable today. The associations are generated in batches every Myr to simulate the temporal distribution of OB associations and supernovae.

As the birthrate of Galactic supernovae is about three per century (see, e.g., Tammann et al. 1994; van den Bergh & McClure 1994), out of which about 80 % – 90 % are core-collapse Type II and Ib/c, the number of born associations and their stellar content should reflect the expected supernovae birthrate. So, how many supernovae progenitors (SNP) are expected to be born in each association, and how many associations are born per Myr?

Since only a modest number of supernovae are needed to generate superbubbles ($>$ five, see, e.g. Mac Low & McCray 1988; Tenorio-Tagle 1996), how the massive OB stars cluster significantly affects the role of superbubbles as a source of cosmic rays. Higdon & Lingenfelter (2005) investigated the temporal and spatial clustering of OB stars, and their model predicted 80% – 90% of supernovae of Type II and Ib/c occur in superbubbles and that the superbubbles, thus, are a primary source of cosmic rays. Their approach to how the OB stars cluster will inspire how SNPs will be born in our modelled associations.

The spatial clustering of OB stars is thoroughly discussed in Higdon & Lingenfelter (2005), but in short, it relates to how the mass of the giant molecular clouds affects the star formation rate. In their work, Higdon & Lingenfelter (2013) assume that the star formation rate per unit molecular cloud mass is constant. The temporal clustering relates to the observational data of OB associations, which show that they are highly substructured and have experienced several episodes of star formation. This is evident in several associations considered in Chapter 2. Elmegreen (2000, 2002) explains how several star forming episodes can happen in the same molecular cloud. Firstly, GMCs are typically part of a hierarchical structure within the interstellar medium (ISM). This structure can facilitate multiple episodes of star formation as smaller clouds within the GMC can individually undergo collapse and star formation at different times. Secondly, radiation and winds from newly formed, massive stars in one part of the cloud can influence other parts, triggering more star formation.

The implementation of spatial clustering is more involved than temporal clustering, and Higdon & Lingenfelter (2005) only briefly explains the implementation in the abstract of their paper. As such, only temporal clustering will be considered here.

Before explaining temporal clustering, we first need to mention the Interstellar Mass Function (IMF), which plays a crucial role in modelling stars. The IMF describes the distribution of stellar masses that form in a star forming event in a given volume of space and covers stars from low-mass brown dwarfs to the very massive O stars (Kroupa 2001, 2002). As discussed by Kroupa, the IMF shows an extraordinary universality, describing present-day star formation in molecular clouds varying in size from the smallest to the very rich and massive, through to ancient and metal-poor populations. The first works on the IMF came from Salpeter (1955), and today perhaps the most used model is the broken power-law by Kroupa (2001, 2002). We note that more recent formulations of the IMF exist, such as the one of Maschberger (2013), but as the authors note, this formulation is essentially indistinguishable from the standard IMF of Kroupa. As in Higdon & Lingenfelter (2005), we will here be using the modified Kroupa IMF, where the index α_3 has been increased from 2.35 to 2.7 to take into account unresolved binaries. This is discussed in Kroupa (2002). The modified Kroupa IMF is given by the following broken power law:

$$\xi(m) = k \begin{cases} (m/m_1)^{-\alpha_0} & , \ m_0 = 0.01 < m/M_\odot \le m_1 = 0.08, \\ (m/m_1)^{-\alpha_1} & , \ m_1 = 0.08 < m/M_\odot \le m_2 = 0.5, \\ (m_2/m_1)^{-\alpha_1} (m/m_2)^{-\alpha_2} & , \ m_2 = 0.5 < m/M_\odot \le m_3 = 1.0, \\ (m_3/m_2)^{-\alpha_2} (m_2/m_1)^{-\alpha_1} (m/m_3)^{-\alpha_3} & , \ m_3 = 1.0 < m/M_\odot \le m_4 = 120, \end{cases} \tag{4.1}$$

$$\begin{aligned} \alpha_0 &= 0.3, \ m_0 = 0.01 < m/M_\odot \le m_1 = 0.08, \\ \alpha_1 &= 1.3, \ m_1 = 0.08 < m/M_\odot \le m_2 = 0.5, \\ \alpha_2 &= 2.3, \ m_2 = 0.5 < m/M_\odot \le m_3 = 1.0, \\ \alpha_3 &= 2.7, \ m_3 = 1.0 < m/M_\odot \le m_4 = 120, \end{aligned}$$

Higdon & Lingenfelter (2005) combine a size-frequency distribution of young stellar clusters, the modified Kroupa IMF and the study of ionising luminosities by McKee & Williams (1997) to derive an equation for the number of clusters born per Myr with a number of stars N_* between N_* and $N_*+\mathrm{d}N_*$. For this derivation, the reader is referred to Higdon & Lingenfelter (2005) and references therein, but the final distribution is given as follows:

$$\frac{\mathrm{d}n_{\mathrm{sc}}(N_*)}{\mathrm{d}N_*\,\mathrm{d}t} = 1.65 \left(\frac{1.7 \times 10^6}{N_*^{1+\alpha}} \right) \mathrm{Myr}^{-1}, \ \text{for } 190 \le N_* \le 1.7 \times 10^6. \tag{4.2}$$

Here, $\mathrm{d}n_{\mathrm{sc}}(N*)$ is the number of clusters with N_* stars, and N_* denotes stars of all masses, not solely the massive OB stars. The parameter α determines the slope of the power law and is determined by observations of H II regions. Kennicutt et al. (1989) investigated 30 nearby Galaxies, and found a best fit value of $\alpha = 1 \pm 0.5$, and McKee & Williams (1997) who focused on the Milky Way, found $\alpha = 0.99 \pm 0.25$. McKee & Williams (1997) excluded the smallest H II regions due to incompleteness in the dataset on the lower end. That α should be around 1 is reasonable: a value for $\alpha \gtrsim 2$ would cause most of the massive stars to be located in the smallest associations, and with $\alpha \lesssim 0$ almost all of the most massive stars would be in the largest associations (McKee & Williams 1997). Higdon & Lingenfelter (2005) uses $\alpha = 1$ in their calculations, but here we have taken $\alpha = 0.8$. Our α is within the reported uncertainties, and as shown in Chapter 4.2, this value seems to create a better fit with the observational data on OB associations than $\alpha = 1$.

On average, the number of SNPs born is related to the total number of stars formed. The parameter f_{SN} denotes the fraction of the formed stars with initial mass above $8\,\mathrm{M}_\odot$, which is the commonly cited minimum mass needed for core-collapse supernovae (see, e.g. Smartt 2009; Woosley & Weaver 1995). For the modified Kroupa IMF, Higdon & Lingenfelter (2005) calculate that $f_{\mathrm{SN}} = 1.1 \times 10^{-3}$. Thus, to use Equation (4.2) on SNPs, the lower and upper limits on the number of stars change to $N^{\mathrm{SN}}_{\mathrm{min}} = 0.21$ and $N^{\mathrm{SN}}_{\mathrm{max}} = 1870$. The fact that $N^{\mathrm{SN}}_{\mathrm{min}} < 1$ reflects that not every star cluster contains OB stars. The probability of an association containing an SNP is less than one for $N_* < 909$.

From Equation (4.2), we can then calculate the expected number of associations born per Myr containing more than one OB star as follows,

$$3.085 \times 10^3 \sum_{N_*^{\mathrm{SN}}=2}^{1870} \left(N_*^{\mathrm{SN}}\right)^{-2} = 1988\,\mathrm{Myr}^{-1}. \tag{4.3}$$

Notice the sum starts at $N_*^{\mathrm{SN}} = 2$ as we are not interested in the singleton end of the distribution. Higdon & Lingenfelter (2005) find that the $N_*^{\mathrm{SN}} = 1$ end of the distribution agrees with the OB field stars.

We can calculate the expected number of SNPs to be born within an OB association from the cluster distribution in Equation (4.2). We multiply the distribution by $f_{\mathrm{SN}} N_*$ and integrate over the desired range. The birthrate of SNPs born in associations with no more than one SNP is then given by

$$3.085 \times 10^3 \int_{190}^{909} \frac{\mathrm{d}N_*}{N_*} = 4.83 \times 10^3\,\mathrm{Myr}^{-1}, \tag{4.4}$$

and the birthrate of supernovae in associations containing more than one SNP is

$$3.085 \times 10^3 \int_{1}^{1870} \frac{\mathrm{d}N_*^{\mathrm{SN}}}{N_*^{\mathrm{SN}}} = 2.32 \times 10^4\,\mathrm{Myr}^{-1}. \tag{4.5}$$

In total, these equations of Higdon & Lingenfelter (2005) predict the birthrate of supernovae will be roughly $2.81 \times 10^4\,\mathrm{Myr}^{-1}$, or about one every 36 years. This estimate is consistent with the expected number of Galactic supernovae (Mac Low & McCray 1988). To illustrate how the SNPs are distributed among the OB associations, the cumulative probability distribution $P(> N_*^{\mathrm{SN}})$ can be calculated as follows:

$$\begin{aligned} P(> N_*^{\mathrm{SN}}) &= 1 - \left(\frac{4.83 \times 10^3}{2.81 \times 10^4} + \frac{3.085 \times 10^3}{2.81 \times 10^4} \ln N_*^{\mathrm{SN}} \right) \\ &= 0.828 - 0.11 \ln N_*^{\mathrm{SN}}, \\ 1 < N_*^{\mathrm{SN}} &\leq 1870. \end{aligned} \tag{4.6}$$

Considering several episodes of star formation in an association is relatively straightforward. Let g denote the number of star forming events in an association. Then, in Equation (4.4), the upper limit for the integral would be decreased by a factor of g as fewer stars would need to be born in each star forming episode to achieve at most one SNP in the association. This is easiest seen from the equation $gN_* f_{\mathrm{SN}} \leq 1$. Hence, Equation (4.6) is modified to

$$P(> N_*^{\mathrm{SN}}) = C(g) - 0.11 \ln N_*^{\mathrm{SN}}, \quad 1 < N_*^{\mathrm{SN}} \leq 1870g, \tag{4.7}$$

where $C(g) = 0.828, 0, 95$ and 1.0 for $g = 1, 3$ and 5, respectively. These values are given in Table 4.1 together with the expected number of SNPs to be born in OB associations (OBAs). The cumulative probability distributions for these three values for g are shown in Figure 4.2 and illustrate how we get more clustering of OB stars

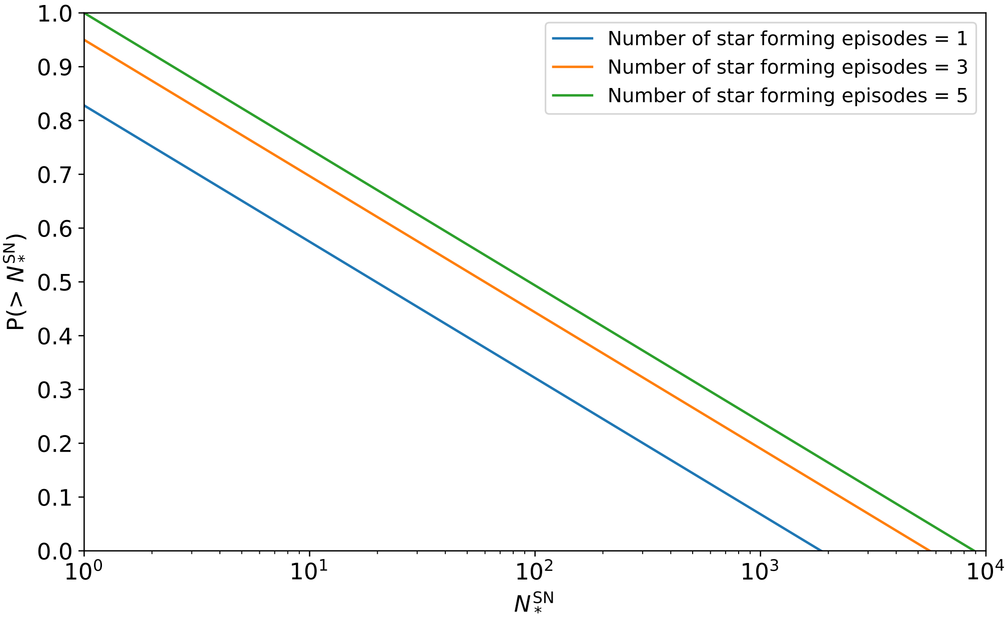

Figure 4.2: Temporal clustering of supernovae progenitors. $P(> N_*^{\mathrm{SN}})$ shown for 1, 3 and five star forming episodes.

with several star forming episodes. With five such episodes, this model predicts that all of the OB stars in our Galaxy would be born in OB associations.

For $g = 1, 3$ and 5, the upper limit for the number of massive stars in OB association becomes, respectively, $1870, 5610$ and 9350. How does this fit with observations and models made by other authors? McKee & Williams (1997) investigated supernovae progenitors with a minimum mass of $8\,\mathrm{M}_\odot$ and found for their model that the largest associations with five star forming episodes contained about 7200 OB stars. This is less than what the distribution of Higdon & Lingenfelter (2005) predicts, but McKee & Williams (1997) did use a different IMF. McKee & Williams (1997) compares their result with that of Heiles (1990) and Ferriere (1995), and writes that their numbers correspond to, respectively, a maximum number of SNPs in Galactic associations of about 9000 and 7230. Thus, the upper limit for our model of 9350 SNPs in an association is perhaps a bit on the higher end, but not unreasonable.

Table 4.1

g	$C(g)$	SNPs born Myr^{-1} in OBAs
1	0.828	23270
3	0.95	26600
5	1	28100

When the number of SNPs to be born in OB associations per Myr is specified, a

Monte Carlo simulation is used to draw associations from the distribution in Equation (4.2) with limits given by $N_{\mathrm{min}}^{\mathrm{SN}} = 2$ and $N_{\mathrm{max}}^{\mathrm{SN}} = 1870$. Associations are drawn until we have reached at least 99% of the expected number of SNPs to be born each Myr; this limit prevents a constant overshooting of how many SNPs we generate each Myr and allows for some random fluctuations. From testing the code, this limit made the average number of SNPs generated per Myr very close to the calculated numbers found in Table 4.1. Each association is populated g times from Equation (4.2), and each star forming episode in an association is separated by 4 Myr (see, e.g., Chapter 2 and Higdon & Lingenfelter 2013; McKee & Williams 1997). McKee & Williams (1997) results suggest that each star forming episode in an association would be of an equal number of stars, which agrees with the earlier work of Elmegreen & Lada (1977). As such, we will take the generations of stars to contain an equal number of stars in our model. Once the associations and their stellar content are drawn, they are placed in the modelled Galaxy using a Monte Carlo simulation.

If we, for instance, run the simulation for 100 Myrs, the resulting map of OB associations' placement will look similar to that of Figure 4.3. Note that the associations whose member stars have all exploded are not being plotted. The spiral arm structure, the Local Arm and the devoid region are clearly visible and align with the density map of the modelled Galaxy in Figure 4.1.

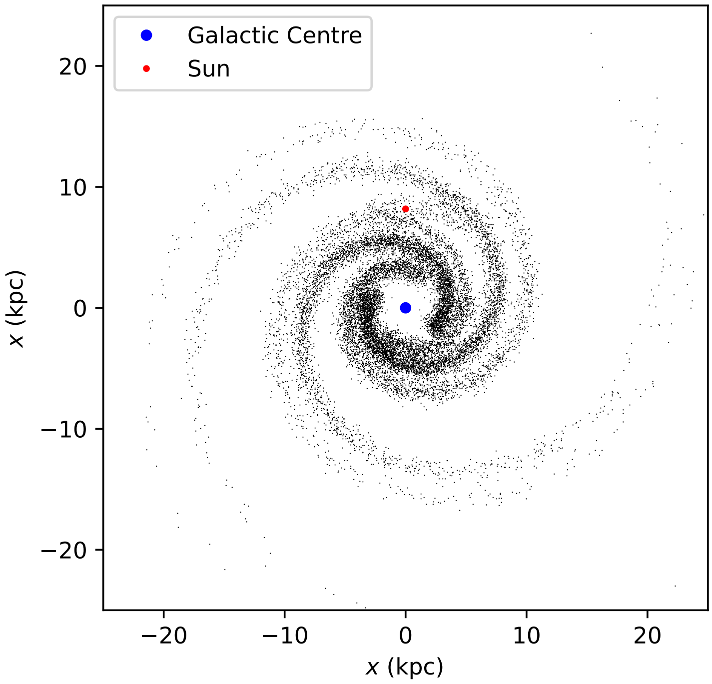

Figure 4.3: Modelled Galaxy after 100 Myrs. Each black dot represents an OB association, containing at least 2 OB stars. The Galactic centre and the Sun are highlighted. The Local Arm and the devoid region of Sagittarius-Carina are also visible.

The masses for the OB stars are drawn randomly from the modified Kroupa IMF, as given in Equation (4.1). The mass is then used to determine the lifetime of the star. Schaller et al. (1992) investigated stellar evolutionary models and also gave data for the lifetimes of stars as a function of mass. This data was then used by Fuchs et al. (2006) to make a fit for the main-sequence lifetime in the mass-range $2 \leq m/\mathrm{M}_\odot \leq 67$. To make the function better fit the expected lifetimes for stars with even higher masses as compared to the data of Schaller et al. (1992), we have scaled the function of Fuchs et al. (2006) by a factor of 1.65:

$$\tau = 1.65\tau_0 m^{-\alpha}, \ \tau_0 = 1.6 \times 10^8\,\mathrm{yr}, \ \alpha = 0.932. \tag{4.8}$$

Here, m is the stellar mass in units of solar masses $\mathrm{M}_\odot$. This function is illustrated in Figure 4.4 where the modelled ages for specific stellar masses are also shown.

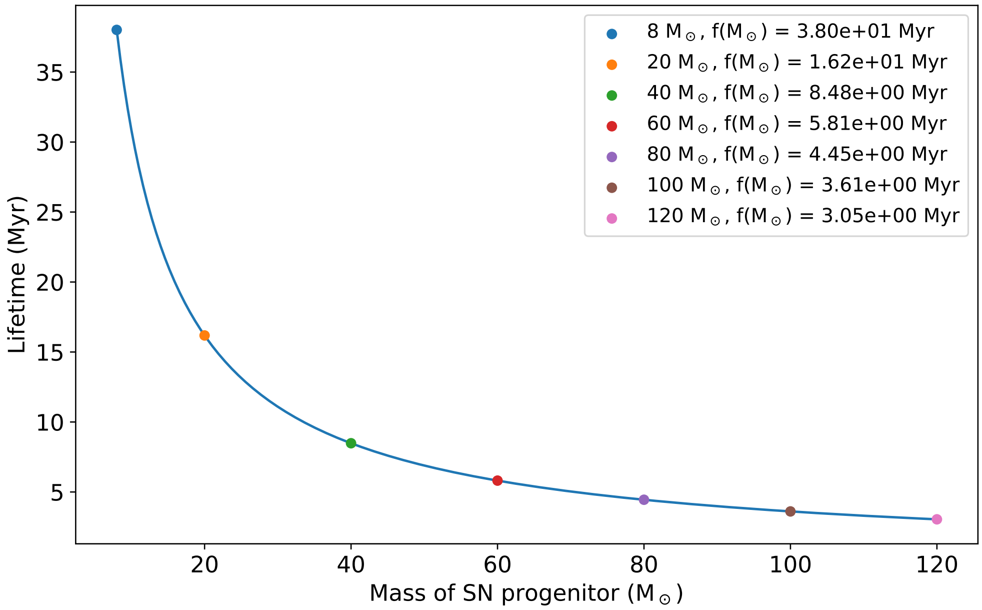

Figure 4.4: Stellar age as a function of stellar mass. The distribution is described by Equation (4.8). The stellar ages for specific stellar masses are also shown.

The massive OB stars have now been assigned a mass, lifetime and birthplace in the Galaxy, with the birthplace being the association's centre. These stars are not taken as stationary but will move about as time passes. Typically, the velocity dispersion within an OB association is of the order of a few $\mathrm{km\,s^{-1}}$ and anisotropic (see, e.g., Wright 2020). Following Higdon & Lingenfelter (2005), we will, for simplicity, assume a Gaussian one-dimensional isotropic velocity dispersion of $\sigma = 2\,\mathrm{km\,s^{-1}}$. Higdon & Lingenfelter (2005) write that this is built upon the kinematic study of nearby OB associations by de Zeeuw et al. (1999), and that $\sigma = 2\,\mathrm{km\,s^{-1}}$ also takes into account the effect of deceleration with escape from the association. The directions for the SNPs are drawn randomly from an isotropic distribution. An example of how the OB stars move around within a modelled OB association is given in Figure 4.5.

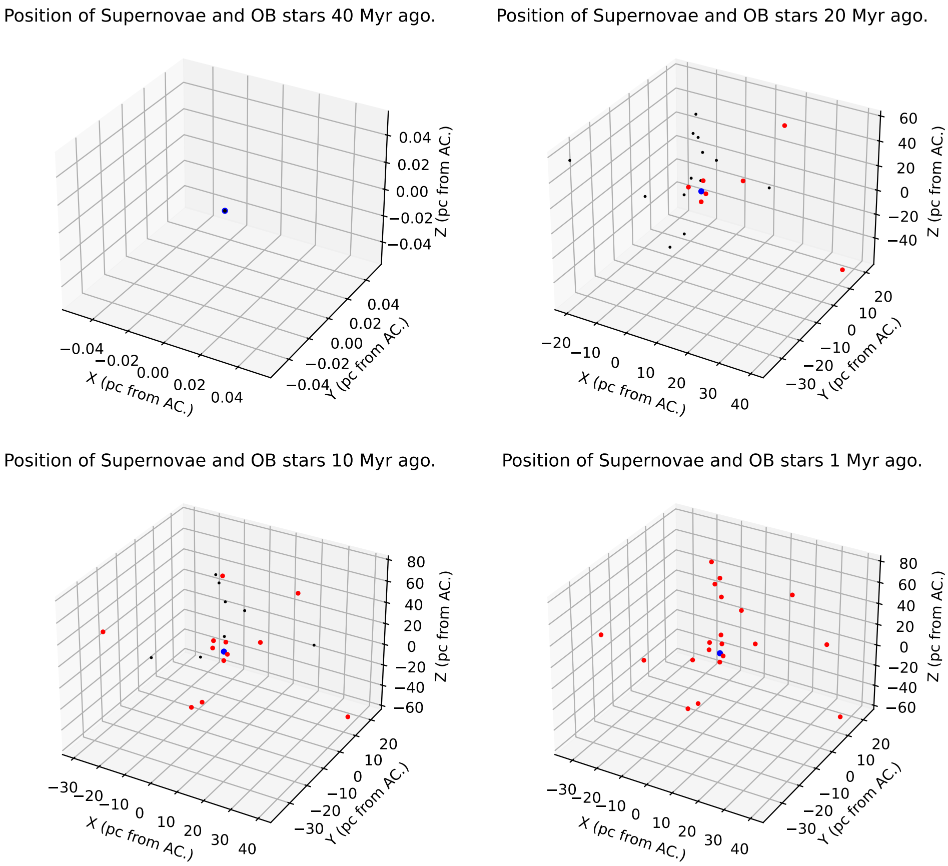
Position of Supernovae and OB stars 40 Myr ago.

Position of Supernovae and OB stars 20 Myr ago.

Position of Supernovae and OB stars 10 Myr ago.

Position of Supernovae and OB stars 1 Myr ago.

Figure 4.5: A modelled OB association located at $x = 0\,\mathrm{kpc}$, $y = 8\,\mathrm{kpc}$, $z = 0\,\mathrm{kpc}$, illustrating how the OB stars move with time. The blue dot is the association centre, the black dots are OB stars, and the red dots are the positions where the OB stars were when they exploded. Coordinates along the axis are relative to the association centre (AC).

With this model for the Galactic OB associations, we would like to see how the resulting longitude profile of the distribution of supernovae becomes and if it resembles the N II distribution in Figure 3.12. To even out fluctuations, we let the simulation run for 100 Myr with five episodes of star formation for each OB association. The resulting distribution is found in Figure 4.6. Excluding the Cygnus X region and the Gum Nebula, we see that the resulting distribution is very close to the modelled N II intensities, with the arm tangents located at $30^\circ, 340^\circ$ and 310° visible, for instance. We note that the resulting longitudinal profile is different for each code run and changes dynamically with the evolution of the modelled Galaxy. Sometimes, this profile closely resembles the intensity profile of N II, while other times, it may be more estranged. This is expected from the inherent randomness in the model, with the number of stars, their masses and the location of OB associations being calculated by Monte Carlo simulations.

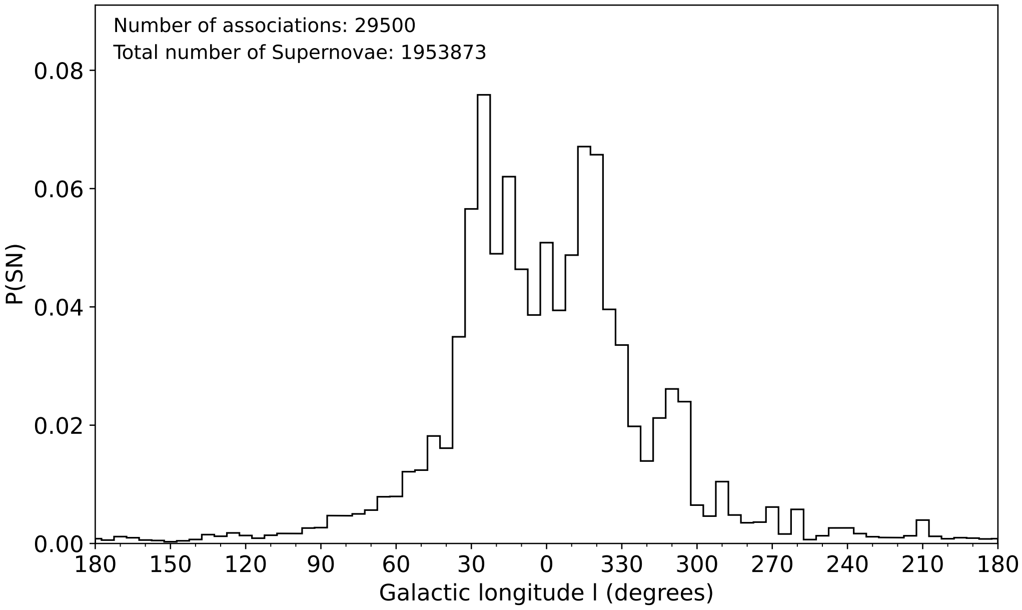

Figure 4.6: Resulting longitude profile of the distribution of supernovae after 100 Myr with five star formation episodes.

4.2 Comparison with observational data

We now combine the modelled and observed associations into one model to tie everything together, and produce a comprehensive model that considers both the historical associations we know and those we cannot observe. A resulting plot of the Galaxy can be seen in Figure 4.7. Here, the spiral arms are shown in the background with labels and the same colours as given in Figure 3.11. The modelled associations are shown with green circles and the known ones in blue. The Sun and Galactic centre have also been highlighted. The procedure for combining the modelled and known associations will next be described.

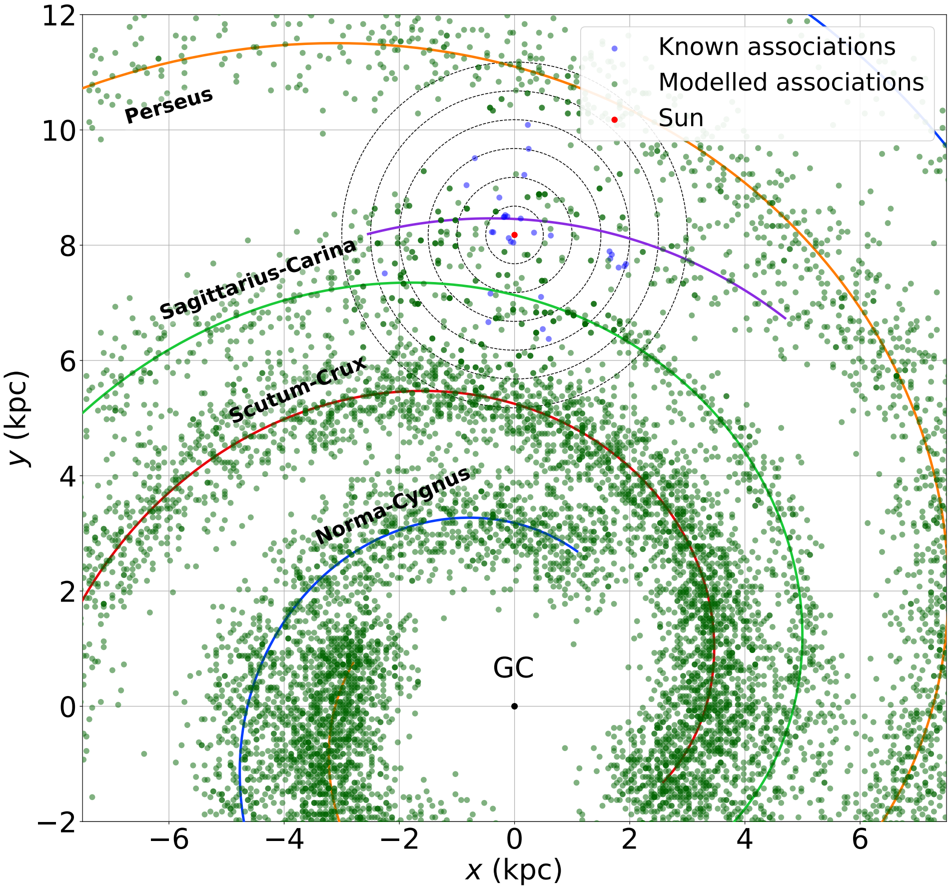

Figure 4.7: Resulting distribution of OB associations after 100 Myr with five star formation episodes. Blue and green dots represent the known and modelled associations, respectively. The four major spiral arms and the Local Arm passing close to the Sun are highlighted. The arms' colours are the same as in the intensity profiles (e.g. Figure 3.12).

First, we generated a modelled Galaxy starting 100 Myr ago with five star forming episodes for each association and retrieved data on the known associations in Table 2.1. To populate the Galaxy with associations, we first added the known associations. Then concentric circles with a spacing of 0.5 kpc centred on the Sun were generated, which is also shown in Figure 4.7. For each circular region, as defined by the concentric circles, we compared the number of known associations to the number of modelled associations. If the number of known associations was equal to or greater than the number of modelled associations, do nothing and move on to the next circular region. If the number of known associations was less than the number of modelled associations, we randomly drew from the modelled associations located in this circular region until the sum of associations in this circular region equalled the total number of modelled associations. Beyond 2.5 kpc we have only modelled associations.

As seen from Figure 4.7, this combined model follows the spirals arms, and the devoid region of Sagittarius-Carina is also seen. This figure explains why we chose $\alpha = 0.8$ in Equation (4.2) instead of $\alpha = 1$ as in Higdon & Lingenfelter (2005): from observations and the data in Table 2.1 it is clear that we know about fewer associations at greater distances from Earth, which is reasonable considering the low density of OB associations and difficulties observing them. Hence, one would expect that, if not all, we should have observed the majority of the closest associations to Earth. Thus, there should be at most only a few modelled associations in the first circle in Figure 4.7, which we achieved with $\alpha = 0.8$. As discussed previously, a higher value for α makes the distribution in Equation (4.2) steeper, meaning we would have many more associations with fewer stars, and these models created an overabundance of modelled associations close to Earth. Setting $\alpha = 0.7$ would make for an even better fit, but since there are still many associations from Wright (2020) which have yet not been considered in Table 2.1, we choose a slightly higher value for α to try to take this into account.

How accurate is our model for the modelled associations? Can it predict the true nature of OB associations, such as their age spread and mass distribution? To be able to answer this, we first need to estimate the past stellar content of the known OB associations, as we are only able to observe those stars who have survived up to the present. To do this, we draw stars from the IMF until we have drawn as many stars as the observed number of stars in the given mass range, which could have survived up to the present day. We only keep the stars whose mass is greater than $8\,\mathrm{M}_\odot$. This is a somewhat simplified approach, as each association in Table 2.1 is taken as having a singular star forming event when estimating the past stellar content, but considering many of them are relatively young and/or have had their substructures studied (such as Sco-Cen), we consider this approach to be satisfactory.

In Table 4.2, we give the average number for the total number of stars with masses above $8\,\mathrm{M}_\odot$ after 10,000 iterations of this procedure. We have also given the number of past supernovae that this procedure predicts and how many SNPs are left. Note that Trumpler 10 is estimated as having no stars left massive enough to produce a supernova due to its old age.

Table 4.2: Estimated past stellar content of the associations in Table 2.1. The calculations for each association were run 10,000 times to average out random fluctuations. Column 1 gives the name for the association in the same order as in Table 2.1. Columns 2 and 3 give the mean SNPs born in the association and the corresponding standard deviation (SD). Columns 4 and 5 list the SNPs who have ended their lives in supernovae and the corresponding SD, and columns 6 and 7 list the SNs that occurred in the last Myr. Columns 8 and 9 give the SNPs which are estimated to be still alive and the corresponding SD.

Name	SNPs	SD	SN	SD	SN 1 Myr	SD	SNPs left	SD
Sco-Cen: US	3.0	2.0	0.0	1.0	0.0	0.0	3.0	2.0
Sco-Cen: UCL	6.0	2.0	1.0	1.0	0.0	0.0	5.0	2.0
Sco-Cen: LCC	5.0	2.0	1.0	1.0	0.0	0.0	4.0	2.0
Ori OB1a	22.0	5.0	2.0	2.0	0.0	1.0	20.0	4.0
Ori OB1b	12.0	3.0	0.0	1.0	0.0	0.0	12.0	3.0
Ori OB1c	23.0	5.0	0.0	0.0	0.0	0.0	23.0	5.0
Ori OB1d	6.0	2.0	0.0	0.0	0.0	0.0	6.0	2.0
Vela OB2	10.0	3.0	1.0	1.0	0.0	0.0	9.0	3.0
Trumpler 10	4.0	2.0	4.0	2.0	0.0	0.0	0.0	0.0
Cyg A	20.0	4.0	3.0	2.0	0.0	1.0	17.0	4.0
Cyg B	15.0	4.0	1.0	1.0	0.0	0.0	14.0	3.0
Cyg C	14.0	3.0	1.0	1.0	0.0	0.0	13.0	3.0
Cyg D	14.0	4.0	4.0	2.0	0.0	1.0	10.0	3.0
Cyg E	21.0	4.0	1.0	1.0	0.0	1.0	20.0	4.0
Cyg F	24.0	5.0	2.0	2.0	0.0	1.0	22.0	4.0
Cyg OB7	100.0	36.0	13.0	6.0	2.0	2.0	87.0	31.0
Aur 1	33.0	6.0	11.0	3.0	1.0	1.0	22.0	4.0
Aur 3	17.0	4.0	2.0	1.0	0.0	1.0	15.0	4.0
Aur 4	20.0	4.0	0.0	0.0	0.0	0.0	20.0	4.0
Ara OB1	54.0	15.0	0.0	0.0	0.0	0.0	54.0	15.0
Per OB2	1.0	1.0	0.0	0.0	0.0	0.0	1.0	1.0
Car OB1	45.0	6.0	1.0	1.0	0.0	1.0	44.0	6.0
CMa OB1	15.0	4.0	1.0	1.0	0.0	0.0	14.0	3.0
Mon OB1	4.0	2.0	0.0	0.0	0.0	0.0	4.0	2.0
Mon OB2	69.0	17.0	1.0	1.0	1.0	1.0	68.0	17.0
Sco OB1	157.0	27.0	4.0	2.0	2.0	1.0	153.0	26.0
Lac OB1	6.0	2.0	0.0	1.0	0.0	0.0	6.0	2.0
Sct OB2	2.0	1.0	0.0	0.0	0.0	0.0	2.0	1.0
Ser OB2	17.0	4.0	0.0	0.0	0.0	0.0	17.0	4.0
Ser OB1	106.0	21.0	2.0	1.0	1.0	1.0	104.0	21.0

Now, we can compare the modelled associations to the known ones. The same instant of the modelled Galaxy has been used for the following figures as in Figure 4.7. Firstly, we take a look at the age distribution for the associations located within a distance of $r \leq 2.5$ kpc from the Sun. As shown in Figure 4.8, the modelled associations vary greatly in age spread. This feature is in agreement with the observed associations. This plot is only one realisation of the model, and the bar plot varies for each run.

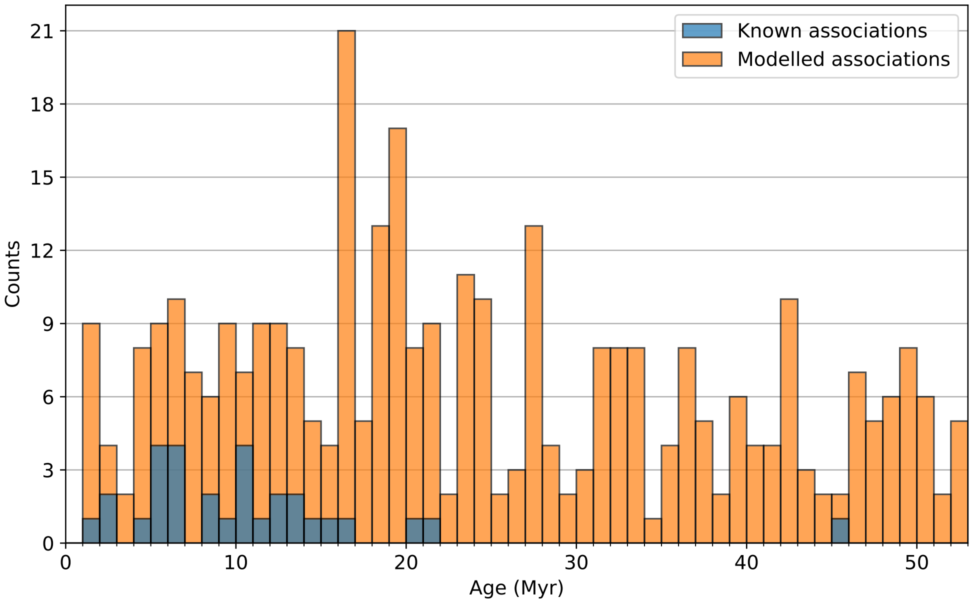

Figure 4.8: An example of the age distribution of known and modelled associations, as the exact distribution varies for each run. Only associations located within a distance of $r \leq 2.5$ kpc from the Sun are considered. Modelled associations are generated with five star forming episodes over 100 Myr.

Figure 4.9 shows the radial density distribution of modelled and known associations. The bin size is the same as the distance between the concentric circles in Figure 4.7, and extends out to 2.5 kpc as there are no known associations beyond this distance. This figure is generated by counting the number of associations in each bin and dividing the count by the corresponding concentric circle area. This highlights that beyond 0.5 kpc, our knowledge of associations is very fragmented, and from the model, one would expect many more associations are waiting to be discovered.

Finally, we investigate how well the model can predict the total association mass (excluding the contribution of stars with mass $< 8\,\mathrm{M}_\odot$). This is shown in Figure 4.10 with a bin width of $50\,\mathrm{M}_\odot$ with five episodes of star formation for the modelled associations. Again, the exact count in each bin varies for each run, but overall, the fit between the mass distribution for modelled and known associations is good. With fewer episodes of star formation, the mass distribution for the modelled associations got skewed towards the lower mass end, and thus, five episodes of star formation made the best fit.

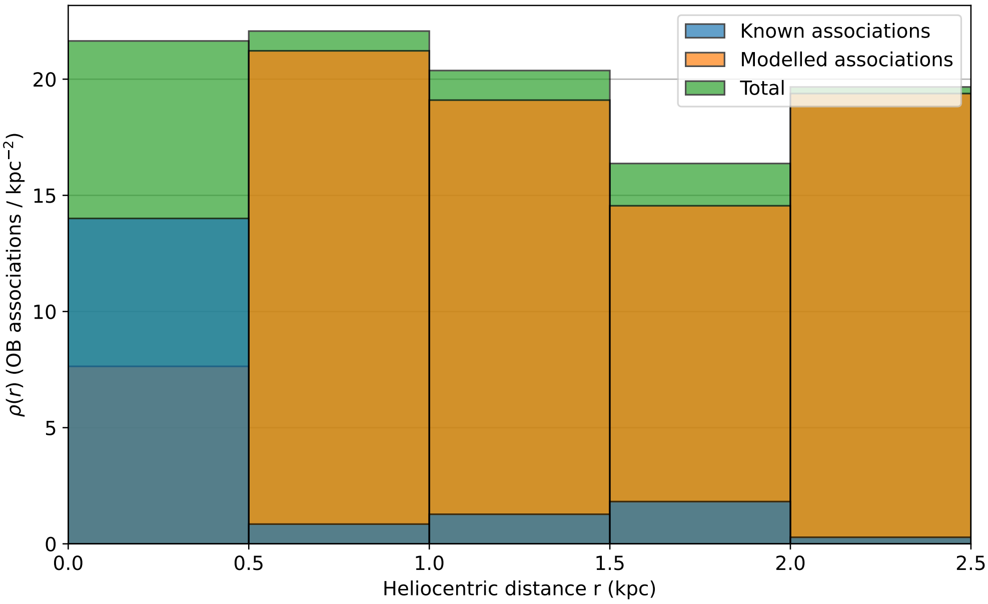

Figure 4.9: An example of the radial density distribution of modelled and known associations, as the exact distribution varies for each run. Only associations located within a distance of $r \leq 2.5\,\text{kpc}$ from the Sun are considered. Modelled associations are generated with five star forming episodes over 100 Myr.

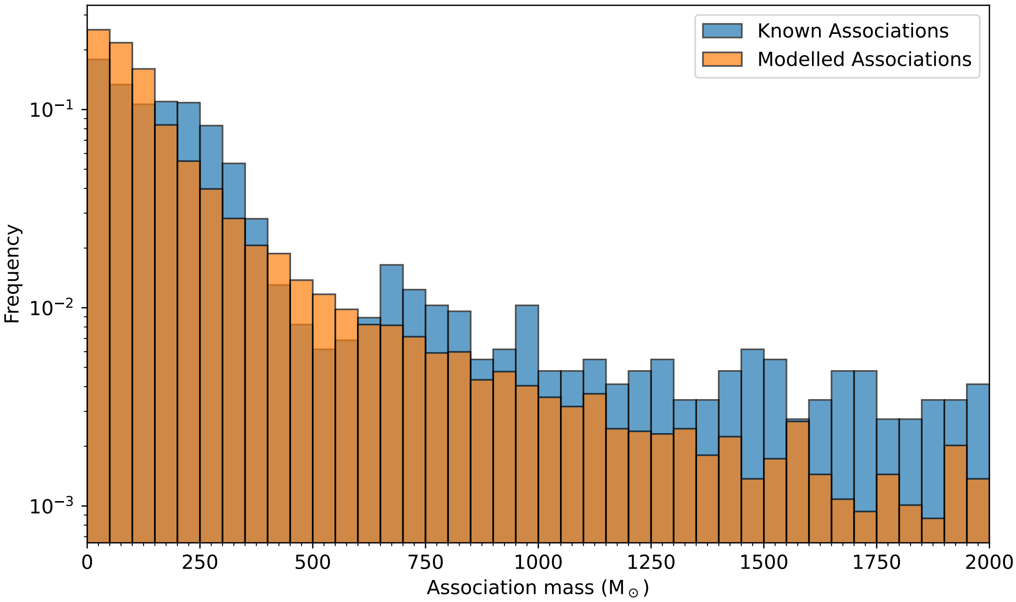

Figure 4.10: An example of the association density distribution for known and modelled associations, as the exact distribution varies for each run. Modelled associations are generated with five star forming episodes over 100 Myr

Chapter 5

Discussion and Conclusion

This thesis's primary aim was to refine our understanding of the spatial distribution of OB associations within the Galaxy so that we could simulate past supernova events. We reviewed the existing literature to compile an up-to-date catalogue of OB associations, including their positions, distances, ages, and stellar contents, as summarised in Table 2.1. This effort was primarily based on the comprehensive survey by Wright (2020) and supplemented by more recent studies released in the years since.

Following Higdon & Lingenfelter (2013), we explored two different models for the Galactic distribution of N II 205 µm line. The resulting longitudinal profile for the N II intensity for the axisymmetric and spiral arm model is found, respectively, in Figure 3.2 and Figure 3.12.

The resulting spiral arm model for the Galaxy, illustrated as a density map in Figure 4.1, was then used to simulate the spatial distribution of OB associations. Figure 4.3 shows one realisation of such a simulation. Finally, the observed OB associations were incorporated into the model, illustrated in Figure 4.7. This combined model gives a more comprehensive view of the distribution of OB associations in our Galaxy, filling in the observational gaps, and can be used to simulate past supernova events.

5.1 Discussion

Chapter 2 focused on investigating the literature for the known OB associations. For this data collection, the catalogues of OB associations by de Zeeuw et al. (1999), Humphreys (1978), Melnik & Dambis (2017, 2020) and Wright (2020) were used. We also supplemented with more recent studies on specific OB associations like, for instance, the work by Quintana & Wright (2021) on the Cygnus region. Wright (2020) is a recent and comprehensive census of our knowledge of OB associations and served as the primary reference for the data collection in this thesis. Specifically, Table 1 in Wright (2020), which lists all OB associations we know of, was heavily used. Due to time limitations, however, not all OB associations listed in this table were investigated for this thesis. We prioritised the OB associations that Wright classified as "well-studied" and "high-confidence", and from the latter category, we prioritised those that he reserved time to discuss in his article. The assumption was that the OB associations he discussed would be the most prominent and well-studied ones. Thus, these should be prioritised when not all OB associations could be investigated for the thesis.

It is important to note that this selection of OB associations from the literature introduces biases in this work that could be addressed in the future. These biases are significant when filling in modelled associations into the Galaxy, compensating for those we have not observed (see Figure 4.7), and for determining the value for the parameter α in Equation (4.2). We selected $\alpha = 0.8$, which is slightly lower than $\alpha = 1$ used by Higdon & Lingenfelter (2005) and McKee & Williams (1997), but still within the expected uncertainties. In Figure 4.7, we can observe some modelled associations that are located close to the Sun ($r \leq 0.5\,\mathrm{kpc}$) for our chosen value of α. A lower value for α, still within the uncertainties reported by McKee & Williams (1997), would have ensured that we would only have had known associations near the Sun. Still, we chose $\alpha = 0.8$ to somewhat compensate for the known associations not included in this thesis. With more time to collect data from the literature, more known associations would be present in Figure 4.7 and could slightly increase the alpha-parameter.

It is also worth discussing the observational difficulties of observing OB associations. As mentioned in the introduction, OB associations have a low density ($< 0.1\,\mathrm{M}_\odot\,\mathrm{pc}^{-3}$) and are gravitationally unbound. One implication is that the stars in these OB associations are spread out over a large area; thus, accurately determining the member stars of the OB associations is difficult. An example of this is the difficulty distinguishing OB field stars from the member stars of OB associations. In the years between each census on OB associations, the membership of each OB association has been refined with more accurate data. A concrete example of this is the census of Humphreys (1978) and de Zeeuw et al. (1999), where the latter could use data from the Hipparcos astrometry satellite to more accurately determine member-stars of OB associations. Moreover, the most recent studies used in Chapter 2 employed data from the Gaia mission, facilitating much more accurate kinematic studies and even helping determine the membership of young stellar objects in OB associations. A notable example is the study of Quintana & Wright (2021) on the Cygnus region, where the authors used Gaia data to suggest a different division than the classical associations in this region. As more data from the Gaia mission becomes available, it is expected that more thorough studies on the already known OB associations will be carried out and perhaps that even more associations will be found.

In Chapter 3, we focused on creating a model for the Galaxy which could recreate the measured values on the Galactic N II intensity. This effort closely followed the work of Higdon & Lingenfelter (2013), which served as an inspiration. For the axisymmetric and spiral arm models, the resulting N II luminosities in this thesis were slightly higher than that of Higdon & Lingenfelter (2013). We attribute these differences to the more up-to-date value for the distance between the Sun and the Galactic centre, R_S, the larger range in latitude used here of $|b| \leq 5°$, following the suggestion from Fixsen, and for the spiral arm model, the specific parameters for the spiral arm resulting from the χ^2 fitting procedure. The exact differences in the implementations of the models could also have contributed to the differences in the modelled N II luminosities.

Our value for the N II luminosity for the spiral arm model was $1.6 \times 10^{40}\,\mathrm{erg\,s^{-1}}$, in comparison to the value obtained by Higdon & Lingenfelter (2013) of $1.4 \times 10^{40}\,\mathrm{erg\,s^{-1}}$. How well does these numbers compare to the measured values? Higdon & Lingenfelter calculated that their model predicted a value for the N II luminosity within the solar circle ($\rho \leq R_{\mathrm{S}}$) to be $1.2 \times 10^{40}\,\mathrm{erg\,s^{-1}}$ for $R_{\mathrm{S}} = 7.6\,\mathrm{kpc}$. Bennett et al. (1994) used the FIRAS data to estimate the N II luminosity within the solar circle and reported this value to be $2.6 \times 10^{40}\,\mathrm{erg\,s^{-1}}$ with 50% uncertainty for $R_{\mathrm{S}} = 8.5\,\mathrm{kpc}$. Moreover, in a preliminary study on the FIRAS data by Wright, Cheng et al. (1991), they list in their Table 1 an estimate for the total Galactic N II luminosity as $\log(L_{\mathrm{N\,II}}) = 6.7 L_{\odot}$ for $R_{\mathrm{S}} = 8.5\,\mathrm{kpc}$. With $L_{\odot} = 3.828 \times 10^{33}\mathrm{erg\,s^{-1}}$ (Prša et al. 2016), this evaluates to $L_{\mathrm{N\,II}} = 1.92 \times 10^{40}\,\mathrm{erg\,s^{-1}}$. From their discussion, they estimate that the error could be as high as 30%. Certainly, the uncertainties are large in this work, too, but these numbers from the literature suggest our model is consistent with observations. Considering the estimates from Bennett et al. (1994) and Wright, Cheng et al. (1991) are larger than both our result and that of Higdon & Lingenfelter (2013), our larger value for the N II luminosity as compared to that of Higdon & Lingenfelter (2013) might suggest a greater accuracy from our model.

As discussed in Chapter 3, our model expanded upon the work of Higdon & Lingenfelter (2013) by also taking into account the Local Arm and the devoid region of the Sagittarius-Carina Arm. We saw that including these regions made a visual improvement on the fit, and also improved the reduced χ^2 value. However, as is evident from the line profile of Fixsen et al. (1999), the exact distribution of the N II intensities is quite complex, and there are still regions where our model does not capture all the details. For instance, towards the Galactic anticentre, the observed data shows a lot of fluctuations, whereas our model is smooth. As we did for the Sagittarius-Carina Arm, one could also incorporate more devoid regions into the model to improve the model even further. This has, for instance, been done by Cordes & Lazio (2002), where they modelled several regions with lower-than-ambient density to more accurately model the Galactic distribution of free electrons. They list these regions in their Table 8, which includes parts of the devoid region of Sagittarius-Carina modelled here. Some of the more prominent regions they list in this table are towards the Galactic centre at around $l = 5^{\circ}$ and the edge of the Gum Nebula at around $l = 280^{\circ}$, as the discrepancy between our model the observed data is quite large at these longitudes.

Cordes & Lazio (2002) also models the contribution of ”clumps”, which are regions of excess electron density compared to the ambient density. They write that these clumps most likely stem from individual H II regions, listed in Tables 5, 6 and 7 in their paper. Some of these overdensities coincide with the Cygnus region and the Gum Nebula, which we already considered in our model. Others, which were not modelled in this thesis, coincide with some peaks in the observed N II intensities towards the Galactic anticentre, and some match the peak towards the Galactic centre.

Other possible improvements to the spiral arm model could also be considered. For instance, we are assuming here that all arms start at the same distance ρ from the Galactic Centre, which might not be the case in reality. For instance, for the modelling of pulsars, Xie et al. (2024) used the spiral arm model by Hou & Han (2014) where all arms started at different values of ρ. Moreover, we are also assuming a single pitch angle for each arm, whereas other works such as Reid et al. (2019) allowed the spiral arms to have a "kink", a point along the arm where the pitch angles differ on either side. Another simplifying assumption made in this work was that the Galactic plane is entirely flat. It is known that this is not the case and that the Galaxy has much more structure in the z-direction, known as the Milky Way warp. Equation (1) of Skowron et al. (2019) describes this warp, and it would be interesting to see how an implementation of this more complex z-distribution would affect the intensity profile as compared to the simple 1° disk used here.

An important point with this discussion is that even though our model for the N II intensities is well able to recreate the measured values by Fixsen et al. (1999), and is an improvement upon the work of Higdon & Lingenfelter (2013), the model is still fairly simple. Only 40 parameters were needed to create the intensity plot in Figure 3.12, and many details of the Galaxy, some of which have been briefly discussed here, have been omitted. Future work could improve upon this, and more observations and accurate determinations of the nature of the Galactic arms could also help make the model more accurate.

In Chapter 4, the resulting model for the Galaxy is used to simulate the distribution of OB associations, with one realisation of this being shown in Figure 4.3. As discussed in this chapter, we only consider the temporal clustering of OB stars. Higdon & Lingenfelter (2005) showed that the resulting clustering of supernova progenitors more accurately resembles the expected number from observations by considering the spatial clustering. The incorporation of spatial clustering on top of temporal clustering could be done in the future to improve the model.

When simulating OB associations, we did not include the Galactic centre region, which is seen as a large "hole" in the centre of Figure 4.3. Clearly, the Galactic centre is not a devoid region, and other works, such as Xie et al. (2024), populated the centre region with pulsars, as seen in their Figure 7. However, as seen from, e.g., Figure 3.12, the modelled intensities generally follow the data from Fixsen et al. (1999), and the differences towards the centre region could be resolved by modelling devoid and enhanced regions, as already discussed. By modelling the centre region by, e.g., the Galactic bar, the differences between our modelled intensities and those measured would be exacerbated, and we thus decided not to include this in the model. It is also worth pointing out that observing the Galactic Centre from Earth is extremely difficult due to the high extinction level and Earth's location within the Galactic plane, so our knowledge of it from observation is still fairly limited.

An interesting application of this thesis could be the modelling of cosmic ray propagation through the Galaxy, which could be used to explore the emission of highly energetic photons in the peta-electronvolt (PeV) range. Generally, the cosmic ray energy spectrum follows a power-law $\mathrm{d}N/\mathrm{d}E \propto E^{-p}$ with energies in the range 10^{10} eV to 10^{20} eV (Hörandel 2003). Of special interest is the "knee", where the energy spectrum steepens at around 4 PeV (Amenomori, Bi et al. 2008). Cosmic rays are accelerated by powerful objects, such as supernova remnants, and up to the knee, cosmic rays are well confined within the Galaxy by the magnetic field (Berezhko & Ksenofontov

1999). The sources of the most energetic cosmic rays with energies in the PeV range are called "PeVatrons", and these sources are known to exist in our Galaxy. For instance, Amenomori, Bao et al. (2021) detected diffuse gamma rays with energies between 100 TeV and 1 PeV, and the recent result from the Lhaaso Collaboration (2024) suggests the presence of PeVatrons towards the Cygnus region.

The peta-electronvolt energy range is a fairly uncharted theory in astrophysics, and the accurate detection of PeVatrons could help our understanding of cosmic rays, their propagation through the Galaxy and their escape from their sources. However, detecting these PeVatrons is difficult, as fewer sources can accelerate cosmic rays to such high energies, and cosmic rays of higher energies diffuse more quickly. Giacinti et al. (2022) recently modelled how cosmic rays stemming from just a few sources, like supernova remnants, spread through the Galactic magnetic field could create large, diffuse sources of PeV photons through their interactions with the interstellar medium. They found, analytically and numerically, that the observed PeV photons by Amenomori, Bao et al. (2021) could be explained by just a few PeVatrons. Thus, the detection of gamma rays on large scales, $\gtrsim 10^\circ$, could provide a new way of detecting these sources of highly energetic photons.

The model for the Galaxy presented in this thesis could be used as a framework for simulating the propagating of the highly energetic cosmic rays as they did in Giacinti et al. (2022). Such simulations could give more insight into the nature of this new frontier in astrophysics and perhaps help to predict the locations of such PeVatrons. As such, we plan to publish the codebase later, and we hope others will find it useful.

5.2 Conclusion

OB associations are important to study to gain insight into star formation, the early evolution of stars and stellar systems, and their role as the spatial origins of cosmic rays and high-energy photons. In this thesis, we have improved the model from Higdon & Lingenfelter (2013) for the Galactic distribution of the N II 205 µm line by using more up-to-date parameters for the Galaxy and taking into account the contributions from the Local Arm and the devoid region of Sagittarius-Carina. From this modelled Galaxy and the data on the known OB associations, we were able to construct a model for the Galactic distribution of OB associations. This model can then be used to simulate past supernova events. This is very exciting, as the model could be developed further to simulate the diffusion of Cosmic Rays and, for instance, help search for the spatial origins of high-energy photons, known as PeVatrons.

References

Ambartsumian, V. A. (1947). *The evolution of stars and astrophysics.*

— (1949). 'Stellar Associations'. In: *Astronomicheskii Zhurnal* 26, p. 3.

Amenomori, M., Bao, Y. W. et al. (2021). 'First Detection of sub-PeV Diffuse Gamma Rays from the Galactic Disk: Evidence for Ubiquitous Galactic Cosmic Rays beyond PeV Energies'. In: *Physical Review Letters* 126.14, 141101, p. 141101. DOI: 10.1103/PhysRevLett.126.141101.

Amenomori, M., Bi, X. J. et al. (2008). 'The All-Particle Spectrum of Primary Cosmic Rays in the Wide Energy Range from 10^{14} to 10^{17} eV Observed with the Tibet-III Air-Shower Array'. In: *Astrophysical Journal* 678.2, pp. 1165–1179. DOI: 10.1086/529514.

Anantharamaiah, K. R. (1986). 'On the origin of the Galactic ridge recombination lines'. In: *Journal of Astrophysics and Astronomy* 7, pp. 131–139. DOI: 10.1007/BF02714206.

Armstrong, Joseph J., Wright, Nicholas J. & Jeffries, R. D. (2018). 'The low-mass population of the Vela OB2 association from Gaia'. In: *Monthly Notices of the Royal Astronomical Society* 480.1, pp. L121–L125. DOI: 10.1093/mnrasl/sly137.

Armstrong, Joseph J., Wright, Nicholas J., Jeffries, R. D. & Jackson, R. J. (2020). 'The dynamics of the γ Vel cluster and nearby Vela OB2 association'. In: *Monthly Notices of the Royal Astronomical Society* 494.4, pp. 4794–4801. DOI: 10.1093/mnras/staa939.

Armstrong, Joseph J., Wright, Nicholas J., Jeffries, R. D., Jackson, R. J. & Cantat-Gaudin, Tristan (2022). 'The structure and 3D kinematics of vela OB2'. In: *Monthly Notices of the Royal Astronomical Society* 517.4, pp. 5704–5720. DOI: 10.1093/mnras/stac3101.

Arnal, E. M. et al. (1987). 'ARA OB1 : a stellar association formed by the action of an energetic event ?' In: *Astronomy and Astrophysics* 174, pp. 78–84.

Axford, W. I. (1981). 'The acceleration of cosmic rays by shock waves'. In: *Annals of the New York Academy of Sciences* 375, pp. 297–313. DOI: 10.1111/j.1749-6632.1981.tb33702.x.

Azimlu, Mohaddesseh, Martínez-Galarza, Juan Rafael & Muench, August A. (2015). 'A WISE Census of Young Stellar Objects in the Perseus OB2 Association'. In: *The Astronomical Journal* 150.3, 95, p. 95. DOI: 10.1088/0004-6256/150/3/95.

Balega, Yu. Yu. et al. (2017). 'Multiplicity Survey of Bright Stars in the Nearby OB Associations'. In: *Stars: From Collapse to Collapse.* Ed. by Yu. Yu. Balega et al. Vol. 510. Astronomical Society of the Pacific Conference Series, p. 325.

Bally, J. et al. (2008). 'The Perseus Cloud'. In: *Handbook of Star Forming Regions, Volume I*. Ed. by B. Reipurth. Vol. 4, p. 308.

Benjamin, R. A. (2008). 'The Spiral Structure of the Galaxy: Something Old, Something New...' In: *Massive Star Formation: Observations Confront Theory*. Ed. by H. Beuther, H. Linz & Th. Henning. Vol. 387. Astronomical Society of the Pacific Conference Series, p. 375.

Benjamin, R. A. et al. (2005). 'First GLIMPSE Results on the Stellar Structure of the Galaxy'. In: *Astrophysical Journal, Letters* 630.2, pp. L149–L152. DOI: 10.1086/491785.

Bennett, C. L. et al. (1994). 'Morphology of the Interstellar Cooling Lines Detected by COBE'. In: *Astrophysical Journal* 434, p. 587. DOI: 10.1086/174761.

Berezhko, E. G. & Ksenofontov, L. T. (1999). 'Composition of cosmic rays accelerated in supernova remnants'. In: *Soviet Journal of Experimental and Theoretical Physics* 89.3, pp. 391–403. DOI: 10.1134/1.558996.

Berlanas, S. R. et al. (2023). 'Gaia-ESO survey: Massive stars in the Carina Nebula. I. A new census of OB stars'. In: *Astronomy and Astrophysics* 671, A20, A20. DOI: 10.1051/0004-6361/202245335.

Blaauw, A. (1944). 'A moving cluster of early-type stars in Perseus'. In: *Bulletin of the Astronomical Institutes of the Netherlands* 10, p. 29.

— (1958). 'The calibration of spectroscopic absolute magnitudes of early B-type stars.' In: *The Astronomical Journal* 63, p. 186.

Blaauw, Adriaan (1964). 'The O Associations in the Solar Neighborhood'. In: *Annual Review of Astronomy and Astrophysics* 2, p. 213. DOI: 10.1146/annurev.aa.02.090164.001241.

— (1991). 'OB Associations and the Fossil Record of Star Formation'. In: *The Physics of Star Formation and Early Stellar Evolution*. Ed. by Charles J. Lada & Nikolaos D. Kylafis. Vol. 342. NATO Advanced Study Institute (ASI) Series C, p. 125. DOI: 10.1007/978-94-011-3642-6_4.

Blaha, Cynthia & Humphreys, Roberta M. (1989). 'A Comparison of the Luminosity Functions in U, B, and V and Their Relationship to the Initial Mass Function for the Galaxy and the Magellanic Clouds'. In: *The Astronomical Journal* 98, p. 1598. DOI: 10.1086/115244.

Blandford, Roger & Eichler, David (1987). 'Particle acceleration at astrophysical shocks: A theory of cosmic ray origin'. In: *Physics Reports* 154.1, pp. 1–75. DOI: 10.1016/0370-1573(87)90134-7.

Bok, Bart J. (1934). 'The Stability of Moving Clusters.' In: *Harvard College Observatory Circular* 384, pp. 1–41.

Bonanno, A., Schlattl, H. & Paternò, L. (2002). 'The age of the Sun and the relativistic corrections in the EOS'. In: *Astronomy and Astrophysics* 390, pp. 1115–1118. DOI: 10.1051/0004-6361:20020749.

Bouy, H. & Alves, J. (2015). 'Cosmography of OB stars in the solar neighbourhood'. In: *Astronomy and Astrophysics* 584, A26, A26. DOI: 10.1051/0004-6361/201527058.

Briceno, C. (2008). 'The Dispersed Young Population in Orion'. In: *Handbook of Star Forming Regions, Volume I*. Ed. by B. Reipurth. Vol. 4, p. 838. DOI: `10.48550/arXiv.0810.2294`.

Briceño-Morales, Geovanny & Chanamé, Julio (2023). 'Substructure, supernovae, and a time-resolved star formation history for Upper Scorpius'. In: *Monthly Notices of the Royal Astronomical Society* 522.1, pp. 1288–1309. DOI: `10.1093/mnras/stad608`.

Brown, A. G. A., de Geus, E. J. & de Zeeuw, P. T. (1994). 'The Orion OB1 association. I. Stellar content.' In: *Astronomy and Astrophysics* 289, pp. 101–120. DOI: `10.48550/arXiv.astro-ph/9403051`.

Cantat-Gaudin, T. et al. (2019). 'Expanding associations in the Vela-Puppis region. 3D structure and kinematics of the young population'. In: *Astronomy and Astrophysics* 626, A17, A17. DOI: `10.1051/0004-6361/201834957`.

Chen, L., de Grijs, R. & Zhao, J. L. (2007). 'Mass Segregation in Very Young Open Clusters: A Case Study of NGC 2244 and NGC 6530'. In: *The Astronomical Journal* 134.4, pp. 1368–1379. DOI: `10.1086/521022`.

Chen, W. P. & Lee, H. T. (2008). 'The Lacerta OB1 Association'. In: *Handbook of Star Forming Regions, Volume I*. Ed. by B. Reipurth. Vol. 4, p. 124. DOI: `10.48550/arXiv.0811.0443`.

Claria, J. J. (1974). 'Investigation of a Milky Way region in Canis Majoris.' In: *The Astronomical Journal* 79, pp. 1022–1039. DOI: `10.1086/111648`.

Clariá, J. J. (1974). 'A study of the stellar association Canis Major OB 1.' In: *Astronomy and Astrophysics* 37, pp. 229–236.

Comerón, F. & Pasquali, A. (2012). 'New members of the massive stellar population in Cygnus'. In: *Astronomy and Astrophysics* 543, A101, A101. DOI: `10.1051/0004-6361/201219022`.

Comerón, F., Schneider, N. & Russeil, D. (2005). 'Star formation in RCW 108: Triggered or spontaneous?' In: *Astronomy and Astrophysics* 433.3, pp. 955–977. DOI: `10.1051/0004-6361:20041586`.

Cordes, J. M. & Lazio, T. J. W. (2002). 'NE2001.I. A New Model for the Galactic Distribution of Free Electrons and its Fluctuations'. In: *arXiv e-prints*, astro-ph/0207156, astro–ph/0207156. DOI: `10.48550/arXiv.astro-ph/0207156`.

Crampton, D. & Georgelin, Y. M. (1975). 'The distribution of optical H II regions in our Galaxy.' In: *Astronomy and Astrophysics* 40, pp. 317–321.

Daflon, Simone & Cunha, Katia (2004). 'Galactic Metallicity Gradients Derived from a Sample of OB Stars'. In: *Astrophysical Journal* 617.2, pp. 1115–1126. DOI: `10.1086/425607`.

Damiani, Francesco (2018). 'The low-mass pre-main sequence population of Scorpius OB1'. In: *Astronomy and Astrophysics* 615, A148, A148. DOI: `10.1051/0004-6361/201730960`.

de Geus, E. J. (1992). 'Interactions of stars and interstellar matter in Scorpio Centaurus.' In: *Astronomy and Astrophysics* 262, pp. 258–270.

de Zeeuw, P. T. et al. (1999). 'A HIPPARCOS Census of the Nearby OB Associations'. In: *The Astronomical Journal* 117.1, pp. 354–399. DOI: `10.1086/300682`.

DeGioia-Eastwood, K. et al. (2001). 'The Star Formation History of Trumpler 14 and Trumpler 16'. In: *Astrophysical Journal* 549.1, pp. 578–589. DOI: `10.1086/319047`.

Drimmel, Ronald & Spergel, David N. (2001). 'Three-dimensional Structure of the Milky Way Disk: The Distribution of Stars and Dust beyond 0.35 R_{solar}'. In: *Astrophysical Journal* 556.1, pp. 181–202. DOI: `10.1086/321556`.

Eddington, Arthur Stanley (1914). *Stellar movements and the structure of the universe.*

Elmegreen, B. G. & Lada, C. J. (1977). 'Sequential formation of subgroups in OB associations.' In: *Astrophysical Journal* 214, pp. 725–741. DOI: `10.1086/155302`.

Elmegreen, Bruce G. (2000). 'Star Formation in a Crossing Time'. In: *Astrophysical Journal* 530.1, pp. 277–281. DOI: `10.1086/308361`.

— (2002). 'Star Formation from Galaxies to Globules'. In: *Astrophysical Journal* 577.1, pp. 206–220. DOI: `10.1086/342177`.

Esteban, C. & García-Rojas, J. (2018). 'Revisiting the radial abundance gradients of nitrogen and oxygen of the Milky Way'. In: *Monthly Notices of the Royal Astronomical Society* 478.2, pp. 2315–2336. DOI: `10.1093/mnras/sty1168`.

Fernandes, B. et al. (2019). 'Runaways and shells around the CMa OB1 association'. In: *Astronomy and Astrophysics* 628, A44, A44. DOI: `10.1051/0004-6361/201935484`.

Ferriere, K. M. (1995). 'The Hot Gas Filling Factor in the Vicinity of the Sun'. In: *Astrophysical Journal* 441, p. 281. DOI: `10.1086/175355`.

Fesen, Robert A. et al. (2021). 'An updated distance to the Cygnus Loop based on Gaia Early DR3'. In: *Monthly Notices of the Royal Astronomical Society* 507.1, pp. 244–245. DOI: `10.1093/mnras/stab2066`.

Fischer, William J. et al. (2016). 'A WISE Census of Young Stellar Objects in Canis Major'. In: *Astrophysical Journal* 827.2, 96, p. 96. DOI: `10.3847/0004-637X/827/2/96`.

Fixsen, D. J., Bennett, C. L. & Mather, J. C. (1999). 'COBE Far Infrared Absolute Spectrophotometer Observations of Galactic Lines'. In: *Astrophysical Journal* 526.1, pp. 207–214. DOI: `10.1086/307962`.

Forbes, D. (1983). 'Optical spiral structure between L = 30 deg and 70 deg'. In: *Kinematics, Dynamics and Structure of the Milky Way*. Ed. by W. L. H. Shuter. Vol. 100. Astrophysics and Space Science Library, pp. 217–222. DOI: `10.1007/978-94-009-7060-1_32`.

— (1984). 'Optical spiral structure at L = 30 to 70. I. New observations of distant early-type stars.' In: *The Astronomical Journal* 89, pp. 475–479. DOI: `10.1086/113537`.

— (1985). 'Optical spiral structure at L = 30-70 deg. II - The distribution of interstellar extinction'. In: *The Astronomical Journal* 90, pp. 301–307. DOI: `10.1086/113730`.

Forbes, Douglas (2000). 'The Serpens OB2 Association and Its Thermal "Chimney"'. In: *The Astronomical Journal* 120.5, pp. 2594–2608. DOI: `10.1086/316822`.

Franco, Jose, Tenorio-Tagle, Guillermo & Bodenheimer, Peter (1990). 'On the Formation and Expansion of H II Regions'. In: *Astrophysical Journal* 349, p. 126. DOI: `10.1086/168300`.

Fuchs, B. et al. (2006). 'The search for the origin of the Local Bubble redivivus'. In: *Monthly Notices of the Royal Astronomical Society* 373.3, pp. 993–1003. DOI: `10.1111/j.1365-2966.2006.11044.x`.

Georgelin, Y. M. & Georgelin, Y. P. (1976). 'The spiral structure of our Galaxy determined from H II regions.' In: *Astronomy and Astrophysics* 49, pp. 57–79.

Giacinti, G. et al. (2022). 'Signatures of anisotropic diffusion around PeVatrons in 100 TeV gamma-ray data'. In: *Physical Review D* 106.12, 123029, p. 123029. DOI: `10.1103/PhysRevD.106.123029`.

Gimenez, A. & Clausen, J. V. (1994). 'AG Persei: absolute dimensions and membership of Perseus OB2.' In: *Astronomy and Astrophysics* 291, pp. 795–804.

Goldsmith, Paul F. et al. (2015). 'Herschel Galactic Plane Survey of [NII] Fine Structure Emission'. In: *Astrophysical Journal* 814.2, 133, p. 133. DOI: `10.1088/0004-637X/814/2/133`.

GRAVITY Collaboration et al. (2019). 'A geometric distance measurement to the Galactic center black hole with 0.3% uncertainty'. In: *Astronomy and Astrophysics* 625, L10, p. L10. DOI: `10.1051/0004-6361/201935656`.

Gregorio-Hetem, J. (2008). 'The Canis Major Star Forming Region'. In: *Handbook of Star Forming Regions, Volume II*. Ed. by B. Reipurth. Vol. 5, p. 1. DOI: `10.48550/arXiv.0808.3812`.

Gregorio-Hetem, J. et al. (2021). 'Searching for Active Low-mass Stars in the CMa Star-forming Region: Multi-band Photometry with T80S'. In: *The Astronomical Journal* 161.3, 133, p. 133. DOI: `10.3847/1538-3881/abd705`.

Gum, C. S. (1952). 'A large H II region at galactic longitude 226 deg.' In: *The Observatory* 72, pp. 151–154.

Gunderson, Sean J. et al. (2024). 'Observed epochal variations in X-ray lines from the O supergiant ζ Puppis do not require substantial changes in the wind mass flux'. In: *Monthly Notices of the Royal Astronomical Society* 529.4, pp. 3154–3170. DOI: `10.1093/mnras/stae547`.

Hanson, M. M. (2003). 'A Study of Cygnus OB2: Pointing the Way toward Finding Our Galaxy's Super-Star Clusters'. In: *Astrophysical Journal* 597.2, pp. 957–969. DOI: `10.1086/378508`.

Heiles, Carl (1990). 'Clustered Supernovae versus the Gaseous Disk and Halo'. In: *Astrophysical Journal* 354, p. 483. DOI: `10.1086/168709`.

Herbst, W. & Havlen, R. J. (1977). 'Ara OB1, NGC 6193 and Ara R1: an optical study of a very young southern complex.' In: *Astronomy and Astrophysics, Supplement* 30, pp. 279–295.

Hess, Victor (1912). 'Über Beobachtungen der durchdringenden Strahlung bei sieben Freiballonfahrten'. In: *Physik Zeitschrift* 13. Accessed: 2024-04-29, p. 1084.

— (2018). 'On the Observations of the Penetrating Radiation during Seven Balloon Flights'. In: *arXiv e-prints*, arXiv:1808.02927, arXiv:1808.02927. DOI: `10.48550/arXiv.1808.02927`.

Higdon, J. C. & Lingenfelter, R. E. (2005). 'OB Associations, Supernova-generated Superbubbles, and the Source of Cosmic Rays'. In: *Astrophysical Journal* 628.2, pp. 738–749. DOI: `10.1086/430814`.

Higdon, J. C. & Lingenfelter, R. E. (2013). 'The Galactic Spatial Distribution of OB Associations and their Surrounding Supernova-generated Superbubbles'. In: *Astrophysical Journal* 775.2, 110, p. 110. DOI: `10.1088/0004-637X/775/2/110`.

Hillebrandt, Wolfgang & Niemeyer, Jens C. (2000). 'Type IA Supernova Explosion Models'. In: *Annual Review of Astronomy and Astrophysics* 38, pp. 191–230. DOI: `10.1146/annurev.astro.38.1.191`.

Hillenbrand, Lynne A. (1997). 'On the Stellar Population and Star-Forming History of the Orion Nebula Cluster'. In: *The Astronomical Journal* 113, pp. 1733–1768. DOI: `10.1086/118389`.

Hillenbrand, Lynne A. et al. (1993). 'NGC 6611: A Cluster Caught in the Act'. In: *The Astronomical Journal* 106, p. 1906. DOI: `10.1086/116774`.

Hoogerwerf, R., de Bruijne, J. H. J. & de Zeeuw, P. T. (2001). 'On the origin of the O and B-type stars with high velocities. II. Runaway stars and pulsars ejected from the nearby young stellar groups'. In: *Astronomy and Astrophysics* 365, pp. 49–77. DOI: `10.1051/0004-6361:20000014`.

Hörandel, Jörg R. (2003). 'On the knee in the energy spectrum of cosmic rays'. In: *Astroparticle Physics* 19.2, pp. 193–220. DOI: `10.1016/S0927-6505(02)00198-6`.

Hou, L. G. & Han, J. L. (2014). 'The observed spiral structure of the Milky Way'. In: *Astronomy and Astrophysics* 569, A125, A125. DOI: `10.1051/0004-6361/201424039`.

— (2015). 'Offset between stellar spiral arms and gas arms of the Milky Way'. In: *Monthly Notices of the Royal Astronomical Society* 454.1, pp. 626–636. DOI: `10.1093/mnras/stv1904`.

Hou, L. G., Han, J. L. & Shi, W. B. (2009). 'The spiral structure of our Milky Way Galaxy'. In: *Astronomy and Astrophysics* 499.2, pp. 473–482. DOI: `10.1051/0004-6361/200809692`.

Howarth, Ian D. & van Leeuwen, Floor (2019). 'The distance, rotation, and physical parameters of ζ Pup'. In: *Monthly Notices of the Royal Astronomical Society* 484.4, pp. 5350–5361. DOI: `10.1093/mnras/stz291`.

Hubble, E. P. (1922a). 'A general study of diffuse galactic nebulae.' In: *Astrophysical Journal* 56, pp. 162–199. DOI: `10.1086/142698`.

— (1922b). 'The source of luminosity in galactic nebulae.' In: *Astrophysical Journal* 56, pp. 400–438. DOI: `10.1086/142713`.

Humphreys, R. M. (1978). 'Studies of luminous stars in nearby galaxies. I. Supergiants and O stars in the Milky Way.' In: *Astrophysical Journal, Supplement* 38, pp. 309–350. DOI: `10.1086/190559`.

Humphreys, R. M. & McElroy, D. B. (1984). 'The initial mass function for massive stars in the galaxy and the Magellanic clouds.' In: *Astrophysical Journal* 284, pp. 565–577. DOI: `10.1086/162439`.

Jeffries, R. D. et al. (2014). 'The Gaia-ESO Survey: Kinematic structure in the Gamma Velorum cluster'. In: *Astronomy and Astrophysics* 563, A94, A94. DOI: `10.1051/0004-6361/201323288`.

Johnson, H. L. & Morgan, W. W. (1953). 'Fundamental stellar photometry for standards of spectral type on the Revised System of the Yerkes Spectral Atlas.' In: *Astrophysical Journal* 117, p. 313. DOI: `10.1086/145697`.

Kapteyn, J. C. (1914). 'On the individual parallaxes of the brighter galactic helium stars in the southern hemisphere, together with considerations on the parallax of stars in general.' In: *Astrophysical Journal* 40, pp. 43–126. DOI: `10.1086/142098`.

Kennicutt Robert C., Jr., Edgar, B. Kevin & Hodge, Paul W. (1989). 'Properties of H II Region Populations in Galaxies. II. The H II Region Luminosity Function'. In: *Astrophysical Journal* 337, p. 761. DOI: `10.1086/167147`.

Knies, Jonathan R. et al. (2024). 'A new understanding of the Gemini-Monoceros X-ray enhancement from discoveries with eROSITA'. In: *arXiv e-prints*, arXiv:2401.17289, arXiv:2401.17289. DOI: `10.48550/arXiv.2401.17289`.

Kroupa, Pavel (2001). 'On the variation of the initial mass function'. In: *Monthly Notices of the Royal Astronomical Society* 322.2, pp. 231–246. DOI: `10.1046/j.1365-8711.2001.04022.x`.

— (2002). 'The Initial Mass Function of Stars: Evidence for Uniformity in Variable Systems'. In: *Science* 295.5552, pp. 82–91. DOI: `10.1126/science.1067524`.

Kuhn, Michael A. et al. (2014). 'The Spatial Structure of Young Stellar Clusters. I. Subclusters'. In: *Astrophysical Journal* 787.2, 107, p. 107. DOI: `10.1088/0004-637X/787/2/107`.

Leahy, D. A., Naranan, S. & Singh, K. P. (1986). 'An X-ray study of the Monoceros supernova remnant.' In: *Monthly Notices of the Royal Astronomical Society* 220, pp. 501–511. DOI: `10.1093/mnras/220.3.501`.

Lhaaso Collaboration (2024). 'An ultrahigh-energy γ -ray bubble powered by a super PeVatron'. In: *Science Bulletin* 69.4, pp. 449–457. DOI: `10.1016/j.scib.2023.12.040`.

Lim, Beomdu et al. (2022). 'A Gaia View on the Star Formation in the Monoceros OB1 and R1 Associations'. In: *The Astronomical Journal* 163.6, 266, p. 266. DOI: `10.3847/1538-3881/ac63b6`.

Mac Low, Mordecai-Mark & McCray, Richard (1988). 'Superbubbles in Disk Galaxies'. In: *Astrophysical Journal* 324, p. 776. DOI: `10.1086/165936`.

Mahy, L. et al. (2009). 'Early-type stars in the young open cluster NGC 2244 and in the Monoceros OB2 association. I. The multiplicity of O-type stars'. In: *Astronomy and Astrophysics* 502.3, pp. 937–950. DOI: `10.1051/0004-6361/200911662`.

Maíz-Apellániz, Jesús et al. (2004). 'A Galactic O Star Catalog'. In: *Astrophysical Journal, Supplement* 151.1, pp. 103–148. DOI: `10.1086/381380`.

Mamajek, Eric (2022). *A Modern Mean Dwarf Stellar Color and Effective Temperature Sequence*. `http://www.pas.rochester.edu/~emamajek/EEM_dwarf_UBVIJHK_colors_Teff.txt`. Version 2022.04.16, accessed on 2024-02-08.

Mamajek, Eric E., Meyer, Michael R. & Liebert, James (2002). 'Post-T Tauri Stars in the Nearest OB Association'. In: *The Astronomical Journal* 124.3, pp. 1670–1694. DOI: `10.1086/341952`.

Martins, F. et al. (2012). 'A quantitative study of O stars in NGC 2244 and the Monoceros OB2 association'. In: *Astronomy and Astrophysics* 538, A39, A39. DOI: 10.1051/0004-6361/201117458.

Maschberger, T. (2013). 'On the function describing the stellar initial mass function'. In: *Monthly Notices of the Royal Astronomical Society* 429.2, pp. 1725–1733. DOI: 10.1093/mnras/sts479.

McKee, C. F. & Ostriker, J. P. (1977). 'A theory of the interstellar medium: three components regulated by supernova explosions in an inhomogeneous substrate.' In: *Astrophysical Journal* 218, pp. 148–169. DOI: 10.1086/155667.

McKee, Christopher F. & Williams, Jonathan P. (1997). 'The Luminosity Function of OB Associations in the Galaxy'. In: *Astrophysical Journal* 476.1, pp. 144–165. DOI: 10.1086/303587.

Melnik, A. M. & Dambis, A. K. (2017). 'Kinematics of OB-associations in Gaia epoch'. In: *Monthly Notices of the Royal Astronomical Society* 472.4, pp. 3887–3904. DOI: 10.1093/mnras/stx2225.

— (2020). 'Internal motions in OB associations with Gaia DR2'. In: *Monthly Notices of the Royal Astronomical Society* 493.2, pp. 2339–2351. DOI: 10.1093/mnras/staa454.

Millour, F. et al. (2007). 'Direct constraint on the distance of γ^2 Velorum from AMBER/VLTI observations'. In: *Astronomy and Astrophysics* 464.1, pp. 107–118. DOI: 10.1051/0004-6361:20065408.

Morgan, W. W., Sharpless, S. & Osterbrock, D. (1952). 'Some features of galactic structure in the neighborhood of the Sun.' In: *The Astronomical Journal* 57, pp. 3–3. DOI: 10.1086/106673.

Morgan, William Wilson, Keenan, Philip Childs & Kellman, Edith (1943). *An atlas of stellar spectra, with an outline of spectral classification.*

Pecaut, Mark J. & Mamajek, Eric E. (2013). 'Intrinsic Colors, Temperatures, and Bolometric Corrections of Pre-main-sequence Stars'. In: *Astrophysical Journal, Supplement* 208.1, 9, p. 9. DOI: 10.1088/0067-0049/208/1/9.

— (2016). 'The star formation history and accretion-disc fraction among the K-type members of the Scorpius-Centaurus OB association'. In: *Monthly Notices of the Royal Astronomical Society* 461.1, pp. 794–815. DOI: 10.1093/mnras/stw1300.

Piddington, J. H. & Minnett, H. C. (1952). 'Radio-Frequency Radiation from the Constellation of Cygnus'. In: *Australian Journal of Scientific Research A Physical Sciences* 5, p. 17. DOI: 10.1071/CH9520017.

Preibisch, T. & Mamajek, E. (2008). 'The Nearest OB Association: Scorpius-Centaurus (Sco OB2)'. In: *Handbook of Star Forming Regions, Volume II*. Ed. by B. Reipurth. Vol. 5, p. 235. DOI: 10.48550/arXiv.0809.0407.

Prša, Andrej et al. (2016). 'Nominal Values for Selected Solar and Planetary Quantities: IAU 2015 Resolution B3'. In: *The Astronomical Journal* 152.2, 41, p. 41. DOI: 10.3847/0004-6256/152/2/41.

Quintana, Alexis L. & Wright, Nicholas J. (2021). 'Revisiting the Cygnus OB associations'. In: *Monthly Notices of the Royal Astronomical Society* 508.2, pp. 2370–2385. DOI: 10.1093/mnras/stab2663.

— (2022). ‘Large-scale expansion of OB stars in Cygnus’. In: *Monthly Notices of the Royal Astronomical Society* 515.1, pp. 687–692. DOI: `10.1093/mnras/stac1526`.

Quintana, Alexis L., Wright, Nicholas J. & Jeffries, Robin D. (2023). ‘Mapping the distribution of OB stars and associations in Auriga’. In: *Monthly Notices of the Royal Astronomical Society* 522.2, pp. 3124–3137. DOI: `10.1093/mnras/stad1160`.

Quireza, Cintia et al. (2006). ‘Radio Recombination Lines in Galactic H II Regions’. In: *Astrophysical Journal, Supplement* 165.1, pp. 338–359. DOI: `10.1086/503901`.

Reber, Grote (1944). ‘Cosmic Static.’ In: *Astrophysical Journal* 100, p. 279. DOI: `10.1086/144668`.

Reed, B. Cameron (2000). ‘New Estimates of the Scale Height and Surface Density of OB Stars in the Solar Neighborhood’. In: *The Astronomical Journal* 120.1, pp. 314–318. DOI: `10.1086/301421`.

Reichen, M. et al. (1990). ‘A detailed study of a 6° diameter field in Scutum’. In: *Astrophysics and Space Science* 163.2, pp. 275–332. DOI: `10.1007/BF00655749`.

Reid, M. J. et al. (2019). ‘Trigonometric Parallaxes of High-mass Star-forming Regions: Our View of the Milky Way’. In: *Astrophysical Journal* 885.2, 131, p. 131. DOI: `10.3847/1538-4357/ab4a11`.

Reipurth, B. (2008). ‘Young Stars in NGC 6231 and the Sco OB1 Association’. In: *Handbook of Star Forming Regions, Volume II*. Ed. by B. Reipurth. Vol. 5, p. 401.

Reipurth, B. & Schneider, N. (2008). ‘Star Formation and Young Clusters in Cygnus’. In: *Handbook of Star Forming Regions, Volume I*. Ed. by B. Reipurth. Vol. 4, p. 36.

Reynolds, R. J. (1976). ‘Observations of the Gum nebula with a Fabry-Perot spectrometer.’ In: *Astrophysical Journal* 203, pp. 151–153. DOI: `10.1086/154057`.

Rizzuto, A. C., Ireland, M. J. & Robertson, J. G. (2011). ‘Multidimensional Bayesian membership analysis of the Sco OB2 moving group’. In: *Monthly Notices of the Royal Astronomical Society* 416.4, pp. 3108–3117. DOI: `10.1111/j.1365-2966.2011.19256.x`.

Roberts William W., Jr. (1972). ‘Application of the Density-Wave Theory of Spiral Structure: Shock Formation Along the Perseus Arm’. In: *Astrophysical Journal* 173, p. 259. DOI: `10.1086/151418`.

Roshi, D. Anish & Anantharamaiah, K. R. (2001). ‘Hydrogen Recombination Lines near 327 MHz. III. Physical Properties and Origin of the Low-Density Ionized Gas in the Inner Galaxy’. In: *Astrophysical Journal* 557.1, pp. 226–239. DOI: `10.1086/321586`.

Ruprecht, J. (1966). In: *IAU Transactions* 12, p. 348.

Ruszkowski, Mateusz & Pfrommer, Christoph (2023). ‘Cosmic ray feedback in galaxies and galaxy clusters’. In: *Astronomy and Astrophysics Reviews* 31.1, 4, p. 4. DOI: `10.1007/s00159-023-00149-2`.

Rygl, K. L. J. et al. (2012). ‘Parallaxes and proper motions of interstellar masers toward the Cygnus X star-forming complex. I. Membership of the Cygnus X region’. In: *Astronomy and Astrophysics* 539, A79, A79. DOI: `10.1051/0004-6361/201118211`.

Sagar, R. et al. (1986). ‘Mass and age distributions of stars in young open clusters.’ In: *Monthly Notices of the Royal Astronomical Society* 220, pp. 383–403. DOI: `10.1093/mnras/220.2.383`.

Salpeter, Edwin E. (1955). 'The Luminosity Function and Stellar Evolution.' In: *Astrophysical Journal* 121, p. 161. DOI: 10.1086/145971.

Santos-Silva, T., Gregorio-Hetem, J. et al. (2018). 'Star formation history of Canis Major OB1. II. A bimodal X-ray population revealed by XMM-Newton'. In: *Astronomy and Astrophysics* 609, A127, A127. DOI: 10.1051/0004-6361/201730815.

Santos-Silva, T., Perottoni, H. D. et al. (2021). 'Canis Major OB1 stellar group contents revealed by Gaia'. In: *Monthly Notices of the Royal Astronomical Society* 508.1, pp. 1033–1055. DOI: 10.1093/mnras/stab2409.

Schaerer, D. & de Koter, A. (1997). 'Combined stellar structure and atmosphere models for massive stars. III. Spectral evolution and revised ionizing fluxes of O3-B0 stars.' In: *Astronomy and Astrophysics* 322, pp. 598–614. DOI: 10.48550/arXiv.astro-ph/9611068.

Schaller, G. et al. (1992). 'New Grids of Stellar Models from 0.8-SOLAR-MASS to 120-SOLAR-MASSES at Z=0.020 and Z=0.001'. In: *Astronomy and Astrophysics, Supplement* 96, p. 269.

Schilbach, E. & Röser, S. (2008). 'On the origin of field O-type stars'. In: *Astronomy and Astrophysics* 489.1, pp. 105–114. DOI: 10.1051/0004-6361:200809936.

Schild, H. & Maeder, A. (1985). 'The initial mass limit for neutron star and black hole formation.' In: *Astronomy and Astrophysics* 143, pp. L7–L10.

Shaver, P. A. et al. (1983). 'The galactic abundance gradient.' In: *Monthly Notices of the Royal Astronomical Society* 204, pp. 53–112. DOI: 10.1093/mnras/204.1.53.

Shevchenko, V. S. et al. (1999). 'The stellar composition of the star formation region CMa R1 - I. Results from new photometric and spectroscopic classifications'. In: *Monthly Notices of the Royal Astronomical Society* 310.1, pp. 210–222. DOI: 10.1046/j.1365-8711.1999.02937.x.

Shull, Michael, Darling, Jeremy & Danforth, Charles (2021). 'Gaia-EDR3 Parallax Distances to the Great Carina Nebula and its Star Clusters (Trumpler 14, 15, 16)'. In: *arXiv e-prints*, arXiv:2103.07922, arXiv:2103.07922. DOI: 10.48550/arXiv.2103.07922.

Skowron, D. M. et al. (2019). 'Mapping the Northern Galactic Disk Warp with Classical Cepheids'. In: *Acta Astronomica* 69.4, pp. 305–320. DOI: 10.32023/0001-5237/69.4.1.

Smartt, Stephen J. (2009). 'Progenitors of Core-Collapse Supernovae'. In: *Annual Review of Astronomy and Astrophysics* 47.1, pp. 63–106. DOI: 10.1146/annurev-astro-082708-101737.

Smith, L. F., Biermann, P. & Mezger, P. G. (1978). 'Star formation rates in the Galaxy.' In: *Astronomy and Astrophysics* 66, pp. 65–76.

Smith, Nathan (2006). 'The Structure of the Homunculus. I. Shape and Latitude Dependence from H_2 and [Fe II] Velocity Maps of η Carinae'. In: *Astrophysical Journal* 644.2, pp. 1151–1163. DOI: 10.1086/503766.

Stark, Antony A. & Lee, Youngung (2005). 'The Scale Height of Giant Molecular Clouds Is Less than That of Smaller Clouds'. In: *Astrophysical Journal, Letters* 619.2, pp. L159–L162. DOI: 10.1086/427936.

Steiman-Cameron, Thomas Y., Wolfire, Mark & Hollenbach, David (2010). 'COBE and the Galactic Interstellar Medium: Geometry of the Spiral Arms from FIR Cooling Lines'. In: *Astrophysical Journal* 722.2, pp. 1460–1473. DOI: `10.1088/0004-637X/722/2/1460`.

Stoop, M. et al. (2023). 'The early evolution of young massive clusters. The kinematic history of NGC 6611/M16'. In: *Astronomy and Astrophysics* 670, A108, A108. DOI: `10.1051/0004-6361/202244511`.

Sung, Hwankyung et al. (2008). 'The Initial Mass Function and Young Brown Dwarf Candidates in NGC 2264. III. Photometric Data'. In: *The Astronomical Journal* 135.2, pp. 441–466. DOI: `10.1088/0004-6256/135/2/441`.

Tammann, G. A., Loeffler, W. & Schroeder, A. (1994). 'The Galactic Supernova Rate'. In: *Astrophysical Journal, Supplement* 92, p. 487. DOI: `10.1086/192002`.

Taylor, J. H. & Cordes, J. M. (1993). 'Pulsar Distances and the Galactic Distribution of Free Electrons'. In: *Astrophysical Journal* 411, p. 674. DOI: `10.1086/172870`.

Tenorio-Tagle, Guillermo (1996). 'Interstellar Matter Hydrodynamics and the Dispersal and Mixing of Heavy Elements'. In: *The Astronomical Journal* 111, p. 1641. DOI: `10.1086/117903`.

Tenorio-Tagle, Guillermo & Bodenheimer, Peter (1988). 'Large-scale expanding superstructures in galaxies.' In: *Annual Review of Astronomy and Astrophysics* 26, pp. 145–197. DOI: `10.1146/annurev.aa.26.090188.001045`.

Tetzlaff, N. et al. (2010). 'Identifying birth places of young isolated neutron stars'. In: *Monthly Notices of the Royal Astronomical Society* 402.4, pp. 2369–2387. DOI: `10.1111/j.1365-2966.2009.16093.x`.

Tomisaka, Kohji (1992). 'The Evolution of a Magnetized Superbubble'. In: *Publications of the ASJ* 44, pp. 177–191.

Uyanıker, B. et al. (2001). 'The Cygnus superbubble revisited'. In: *Astronomy and Astrophysics* 371, pp. 675–697. DOI: `10.1051/0004-6361:20010387`.

Vallée, Jacques P. (2002). 'Metastudy of the Spiral Structure of Our Home Galaxy'. In: *Astrophysical Journal* 566.1, pp. 261–266. DOI: `10.1086/337988`.

— (2008). 'New Velocimetry and Revised Cartography of the Spiral Arms in the Milky Way—A Consistent Symbiosis'. In: *The Astronomical Journal* 135.4, pp. 1301–1310. DOI: `10.1088/0004-6256/135/4/1301`.

— (2013). 'A Synthesis of Fundamental Parameters of Spiral Arms, Based on Recent Observations in the Milky Way'. In: *International Journal of Astronomy and Astrophysics* 3.1, pp. 20–28. DOI: `10.4236/ijaa.2013.31003`.

van den Bergh, Sidney & McClure, Robert D. (1994). 'Rediscussion of Extragalactic Supernova Rates Derived from Evans's 1980–1988 Observations'. In: *Astrophysical Journal* 425, p. 205. DOI: `10.1086/173975`.

VERA Collaboration et al. (2020). 'The First VERA Astrometry Catalog'. In: *Publications of the ASJ* 72.4, 50, p. 50. DOI: `10.1093/pasj/psaa018`.

Whiteoak, J. B. (1963). 'An association of O and B stars in Ara'. In: *Monthly Notices of the Royal Astronomical Society* 125, p. 105. DOI: `10.1093/mnras/125.2.105`.

Wolk, Scott J., Rice, Thomas S. & Aspin, Colin (2013). 'Near-infrared Variability among Young Stellar Objects in the Star Formation Region Cygnus OB7'. In: *Astrophysical Journal* 773.2, 145, p. 145. DOI: 10.1088/0004-637X/773/2/145.

Woosley, S. E. & Weaver, Thomas A. (1995). 'The Evolution and Explosion of Massive Stars. II. Explosive Hydrodynamics and Nucleosynthesis'. In: *Astrophysical Journal, Supplement* 101, p. 181. DOI: 10.1086/192237.

Wright, E., Cheng, E. et al. (1991). 'Preliminary spectral observations of the galaxy with a 7° Beam by the Cosmic Background Explorer (COBE)'. In: *The Astrophysical Journal* 381, pp. 200–209. DOI: 10.1086/170641.

Wright, Nicholas J. (2020). 'OB Associations and their origins'. In: *New Astronomy Reviews* 90, 101549, p. 101549. DOI: 10.1016/j.newar.2020.101549.

Wright, Nicholas J., Drew, Janet E. & Mohr-Smith, Michael (2015). 'The massive star population of Cygnus OB2'. In: *Monthly Notices of the Royal Astronomical Society* 449.1, pp. 741–760. DOI: 10.1093/mnras/stv323.

Wright, Nicholas J., Goodwin, Simon et al. (2022). 'OB Associations'. In: *arXiv e-prints*, arXiv:2203.10007, arXiv:2203.10007. DOI: 10.48550/arXiv.2203.10007.

Wright, Nicholas J. & Mamajek, Eric E. (2018). 'The kinematics of the Scorpius-Centaurus OB association from Gaia DR1'. In: *Monthly Notices of the Royal Astronomical Society* 476.1, pp. 381–398. DOI: 10.1093/mnras/sty207.

Xie, J. T. et al. (2024). 'Modeling the Radial Distribution of Pulsars in the Galaxy'. In: *Astrophysical Journal, Letters* 963.2, L39, p. L39. DOI: 10.3847/2041-8213/ad2850.

Xu, Y. et al. (2013). 'On the Nature of the Local Spiral Arm of the Milky Way'. In: *Astrophysical Journal* 769.1, 15, p. 15. DOI: 10.1088/0004-637X/769/1/15.

Yalyalieva, L. et al. (2020). 'A new look at Sco OB1 association with Gaia DR2'. In: *Monthly Notices of the Royal Astronomical Society* 495.1, pp. 1349–1359. DOI: 10.1093/mnras/staa1205.

Zari, E. et al. (2018). '3D mapping of young stars in the solar neighbourhood with Gaia DR2'. In: *Astronomy and Astrophysics* 620, A172, A172. DOI: 10.1051/0004-6361/201834150.

Zhang, B. et al. (2012). 'The distance and size of the red hypergiant NML Cygni from VLBA and VLA astrometry'. In: *Astronomy and Astrophysics* 544, A42, A42. DOI: 10.1051/0004-6361/201219587.

Zucker, Catherine et al. (2019). 'A Large Catalog of Accurate Distances to Local Molecular Clouds: The Gaia DR2 Edition'. In: *Astrophysical Journal* 879.2, 125, p. 125. DOI: 10.3847/1538-4357/ab2388.

Zucker, Catherine et al. (2020). 'A compendium of distances to molecular clouds in the Star Formation Handbook'. In: *Astronomy and Astrophysics* 633, A51, A51. DOI: 10.1051/0004-6361/201936145.

Appendix A

Code

Here, we briefly overview the code, its structure, and how the user can change different input parameters. The code has been written in `Python`. We focus here on the essentials, and functions made for creating the figures presented in this thesis will not be discussed for the most part. The code is organised into five main folders: `galaxy_model`, `nii_intensities`, `tests`, `observational_data`, and `utilities`. Most of the figures in this thesis have been generated by the scripts in `tests`.

The code generating the Galaxy generates a vast amount of data, and as such, we write it to a file to save RAM and the time required to run the code once the data has been generated. The code automatically checks if the folders for storing data and figures exist and generates them if they are missing, for instance, when running the code for the first time. The code has been tested on both Linux and Windows.

A.1 `utilities`

Perhaps the most important folder is `utilities`, where the user will find the files `constants.py` and `settings.py`. All parameters for the models are stored within `constants.py`, and the user could easily change, for instance, the scalelengths `h_lyc`, `h_spiral_arm` and `h_axisymmetric`, and the distance between the Earth and Galactic Centre, `r_s`. Start angles, pitch angles, and maximum and minimum distance from the Galactic centre for the four major spiral arms, the Local Arm and the devoid region of the Sagittarius-Carina Arm, are also defined within this file. The parameters for the broken power-law for the IMF, and τ and α which enters Equation (4.8), are also found here, and the relative paths to where data and figures are stored are defined at the bottom of this file.

Within `settings.py`, four boolean values are defined: `num_grid_subdivisions`, `add_local_arm`, `add_devoid_region_sagittarius` and `add_gum_cygnus`. The three latter booleans determine whether or not if the Local Arm, the Sagittarius-Carina Arm's devoid region, and the Cygnus X and the Gum Nebula shall be added to the model. These three booleans are by default set to `True`. `add_gum_cygnus` only affects whether or not Cygnus X and Gum Nebula shall be included in the N II intensity plot for the spiral arm model, as these regions already are taken into account from the known data when modelling OB associations.

As for `num_grid_subdivisions`, this setting is to split up the interpolation procedure into smaller chunks, with `num_grid_subdivisions` being the number of chunks. The interpolation procedure is very memory intensive due to the large amount of data generated, so to conserve memory and allow the script to be run on pretty much any computer, the user can split this workload into several smaller parts. Note that the larger the value for `num_grid_subdivisions`, the more time is required for the interpolation to finish. From testing, we recommend using `num_grid_subdivisions = 1` for 32 GB RAM and `num_grid_subdivisions = 4` for 8 GB RAM.

`utilities.py` contains various miscellaneous functions used in the calculations. Equations (3.4) are implemented as `rho(r, l, b)`, `theta(r, l, b)` and `z(r, b)`, and converts the Earthcentric coordinates (r, l, b) to Galactocentric coordinates (ρ, θ, z). Function `xy_to_long(x, y)` takes as input x and y coordinates and calculates the corresponding longitude l. The function `axisymmetric_disk_population(rho, h)`, with `rho` being the usual distance from the Galactic Centre and `h` the scalelength of the Galactic disk, is the implementation of Equation (3.1). Equation (3.7) is implemented in the function `height_distribution(z, sigma)`, with `z` being the vertical height from the Galactic plane and `sigma` determining the falloff in density transverse the plane.

For averaging the N II intensities for the longitudinal profiles, we have defined in `utilities.py` the function `running_average(data, window_size)`. `data` are the intensities, and `window_size` determines the number of points to calculate the average from for each value of l. The IMF, as given by Equations (4.1), and the stellar lifetime as a function of initial mass, given by Equation (4.8), are also defined here.

A.2 observational_data

In this folder, we are focusing on the observational data. For instance, Figure 3.1 is generated in `rrl_hii.py` by accessing the VizieR database. The data entering Table 4.2 is calculated in `analysis_obs_data.py`, and in `firas_data.py` we are preparing the FIRAS data for plotting, which we downloaded from NASA's Goddard Space Flight Center, https://lambda.gsfc.nasa.gov/product/cobe/firas_prod_table.html.

A.3 nii_intensities

In this folder, we generate the axisymmetric and spiral arm models. They are located, respectively, in the files `axisymmetric_disk_model.py` and `spiral_arm_model.py`. Cygnus X and Gum Nebula are generated in `gum_cygnus.py`, and in `chi_squared.py`, we have the script optimising the parameters for the spiral arm model.

In `axisymmetric_disk_model.py`, we have two functions: `plot_axisymmetric()` and `calc_modelled_intensity(b_max = 5)`, where the former is responsible for loading the generated data and plotting it. The resulting figure is shown in Figure 3.2. For `calc_modelled_intensity(b_max = 5)` there is one input parameter, namely `b_max` whose default value is 5°. This is the maximum angle in latitude for which we integrate over such that $\Delta b = 2\,$`b_max`. This is useful for testing how different limits for the integration over latitude affect the resulting intensity plot. The other parameters entering the model, such as `rho_max_axisymmetric`, can be changed within `constants.py`. The resulting intensities for the axisymmetric model are saved to a `.npy` file.

In `spiral_arm_model.py`, `calc_modelled_intensity()` is the main function of interest, which is responsible for calculating the spiral arm intensities. The intensities for the four main spiral arms, as well as for the Local Arm, calculated here. This function has 11 input parameters which the user can change, but these have been given default values for ease of use. They will be next explained.

- `readfile_effective_area=True`: This boolean value controls whether or not the effective area per spiral arm shall be calculated. If it is set to `True` the values will be read from file, and if it is set to `False` the effective areas will be calculated and saved to file. It should be set to `False` when the code is run for the first time and whenever parameters for the spiral arms are changed, as this will affect the resulting effective areas.

- `interpolate_all_arms=True`: This boolean controls whether or not the densities for each arm shall be interpolated. If set to `True`, each spiral arm is interpolated over the entire Galactic plane, as described in the text, and then saved to file. The default value is set to `True`, as it is assumed the user will call the function `calc_modelled_intensity` only when spiral arm parameters are changed and thus need to recalculate the intensities. The reason for having this boolean in the first place is due to how the script for optimising the spiral arm parameters in `chi_squared.py` is designed. In short, we change the parameters for one arm at a time while keeping the others the same, and thus, we interpolate only one arm at a time. As such, we avoid interpolating the other arms multiple times for the same parameters, saving time. The intensities still need to be calculated, so we call `calc_modelled_intensity` with `interpolate_all_arms=False`. It should be set to `True` for all other uses.

- `calc_gum_cyg=False`: This boolean controls whether or not the modelled N II intensities from Cygnus X and Gum Nebula should be calculated. If set to `True`, the values will be calculated and saved to file by the script in `gum_cygnus.py`. It should be set to `True` the first time the script is run, and each time parameters for either Cygnus X or Gum Nebula are changed. Otherwise, it should be set to `False` to save time.

- `recalculate_coordinates=False`: The fourth and final boolean for this function controls whether or not the Galaxy coordinates should be recalculated. This process is time-consuming and should only be set to `True` the first time the script is run or if parameters for the Galaxy are changed, such as the maximum extent for the spiral arm `rho_max`, which is located in `constants.py`.

- `b_max=5` and `db_above_1_deg=0.2`: These parameters define the integrational range over latitude and the step-size above 1° latitude. As discussed in the text, the lines of sight are sampled non-uniformly for $|b| \leq 1°$ and with a fixed db for $|b| > 1°$ up to `b_max`.

- `fractional_contribution`, `h`, `sigma_arm`, `arm_angles` and `pitch_angles` are the final parameters for this function, and are the parameters for the arms themselves as well as the density scale length `h` which enters Equation (3.12). By default, these values are set to those stored in `constants.py`, but could be set to different values when calling the function. `sigma_arm` corresponds to σ_{A} which enters Equation (3.11). `fractional_contribution`, `arm_angles` and `pitch_angles` have to contain the same number of values and could either be a `Python list` or a `numpy array`.

As briefly mentioned, in `chi_squared.py`, we find the code which optimises the parameters entering the model. To run this script, one only has to call the function `run_tests(num_iterations=10)` and specify how many iterations you want the code to run. The default value is set to 10. For the first iteration, every parameter is varied around the value located in `constants.py`. The best parameters are kept and used as input in the next iteration. The best-fit parameters are printed to the terminal when the script is finished.

In `gum_cygnus.py`, we generate and save to file the intensities resulting from the modelled Cygnus X region and Gum Nebula. The calculations for both are done by calling the function `generate_gum_cygnus()`, which in turn calls the functions `gum()` and `cygnus()`. The latter functions calculate the Gum Nebula and the Cygnus X region, respectively, as described in the text. If the user wants to change the parameters for these regions, this can be done within `gum()` and `cygnus()`.

A.4 `galaxy_model`

In the final folder, we have the scripts which simulate the OB associations. Our first file, `galaxy_density_distr.py`, generates the coordinates for the Galaxy. The grid is generated in (x, y, z) coordinates with uniform spacing between each point. The generated coordinates and densities are saved to file and are generated by calling the function `generate_coords_densities()`. The parameters which enter this function are next described:

- `plane=1000`: This is the number of points along the x and y direction whose default value is 1000, such that the Galactic plane has a total of 1×10^6 number of points at which the OB associations can be placed.

- `transverse=20`: This is the number of points along the z direction whose default values is 20. As such, with the default value for `plane`, the number of grid points for which the OB associations could be placed is 20 million.

- `half_edge=40`: This is the distance in kpc from the Galactic Centre along the x and y axis for which the Galaxy is defined. The default value is set to 40 kpc, which is the distance from the Galactic Centre to the endpoint of the spiral arms (35 kpc) plus 5 kpc to take into account the falloff in density transverse the spiral arms.
- `readfile_effective_area=True`: This boolean parameter does the same job as in `calc_modelled_intensity`. Set this to `False` the first time the code is run and anytime parameters for the modelled Galaxy are changed. Otherwise, set it to `True` to save time running the code.
- `read_data_from_file=True`: This boolean parameter, which defaults to `True`, controls whether or not the coordinates and densities are read from file or calculated. Set this parameter to `False` the first time the code is run to calculate coordinates and densities and save them to file. When it is set to `True`, coordinates and densities are read from file.

The code uses an object-oriented approach for modelling OB associations. We have three main classes: one for the Galaxy, one for the Associations, and one for the OB stars. These are, respectively, located in the following files: `galaxy_class.py`, `association_class.py` and `supernovae_class.py`. How these classes work and are designed will now be explained.

The Galaxy class is mainly responsible for generating and storing the Galaxy's coordinates and densities, and drawing the positions of OB associations with a Monte Carlo simulation every Myr. When creating an instance of the Galaxy class, three parameters can be passed to it: `star_formation_episodes`, `sim_time_duration` and `read_data_from_file`. `sim_time_duration` is the number of Myr ago the simulation shall start. The Galaxy is generated in the past to produce supernovae which could have produced cosmic rays observable today. Every Myr, we draw the association's placement from the emissivity map generated by `generate_coords_densities()`. The parameter `read_data_from_file` is passed on to `generate_coords_densities()`, and as mentioned, controls whether or not the coordinates and densities for the Galaxy are calculated or read from file.

The final parameter for the Galaxy class is `star_formation_episodes`, which intuitively controls how many star forming episodes shall occur in each association. As described in the text, each episode is separated by 4 Myr and are equal in size. Finally, if the user wants to change the parameter α, which enters Equation (4.2), this can be done by changing the `alpha` argument of the function `_association_distribution` located within the Galaxy class.

The Galaxy Class generates associations for every Myr by creating instances of the association class, which in turn creates instances of the supernovae class to store information about each OB star. If the user wants to modify the calculated age or the IMF used, this is done in `utilities.py`.

NTNU

Norwegian University of
Science and Technology